Characterization and Nonlinear Cleanup of Noise in Optical Communication Systems

by

William S. Wong

Submitted to the Department of
Electrical Engineering and Computer Science
in partial fulfillment of the requirements for the degree of

Doctor of Philosophy
in Electrical Engineering and Computer Science

at the

MASSACHUSETTS INSTITUTE OF TECHNOLOGY

August 1999
[September 1999]

Author .....
Department of
Electrical Engineering and Computer Science
August 12, 1999

Certified by .....
Hermann A. Haus
Institute Professor
Thesis Supervisor

Certified by .....
Erich P. Ippen
Elihu Thomson Professor of Electrical Engineering
and Professor of Physics
Thesis Supervisor

Accepted by .....
Arthur C. Smith
Chairman, Department Committee on Graduate Students

Characterization and Nonlinear Cleanup of Noise in Optical Communication Systems

by

William S. Wong

Submitted to the Department of
Electrical Engineering and Computer Science
on August 12, 1999, in partial fulfillment of the
requirements for the degree of
Doctor of Philosophy
in Electrical Engineering and Computer Science

Abstract

In the first half of my thesis, I will present experimentally measured photon statistics of RZ/NRZ signals in an optically pre-amplified direct-detection receiver, and show that the results are in good agreement with quantum photodetection theory. Specifically, the ZEROs are described by a degenerate Bose-Einstein distribution, while the ONEs are described by a noncentral-negative-binomial distribution. We will compare the exact quantum mechanical approach with the semiclassical Gaussian approximation in terms of evaluating the bit-error rate and the optimal decision threshold.

I will then describe a nonlinear pulse filter that transmits incident pulses while rejecting cw background as well as ASE noise. The filter is realized by constructing a nonlinear optical Sagnac loop that is imbalanced by asymmetric dispersion. In the first demonstration at 30 Mb/s, a relative extinction of 22 dB (with respect to the pulse) is measured for the cw background. We also demonstrate cleanup of in-band ASE noise at 10 Gb/s. Other researchers have adopted my techniques and built similar pulse filters to clean up compressed pulses so as to build a pedestal-free, 5-ps 16-wavelength WDM source at 10 Gb/s and a 210-fs single-channel TDM source at 640 Gb/s.

Thesis Supervisor: Hermann A. Haus
Title: Institute Professor

Thesis Supervisor: Erich P. Ippen
Title: Elihu Thomson Professor of Electrical Engineering
and Professor of Physics

Acknowledgments

I thank my thesis supervisors Professors Hermann A. Haus and Erich P. Ippen for the opportunity to work in their research group. I am grateful to both of them for financial support through a research assistantship.

I thank Professor Haus for listening to my ideas patiently during the past four years. His unsurpassed creativity and productivity has been inspiring. Professor Ippen always guided me through research problems by offering his intuitive pictures. His insight, comments, as well as his penetrating questions are greatly appreciated.

I dedicate my Ph.D. thesis to my wonderful wife Nini. Words alone cannot express my love for her.

Contents

List of Figures

List of Tables

List of Acronyms

ASE	Amplified spontaneous emission (noise)
BE	Bose-Einstein distribution
BER	Bit error rate
cw	Continuous wave radiation
DCF	Dispersion-compensating fiber
DDF	Dispersion-decreasing fiber
DFB	Distributed feedback laser
DFF	Dispersion-flattened fiber
DI-NOLM	Dispersion-imbalanced nonlinear optical loop mirror; after [7]
DILM	Dispersion-imbalanced nonlinear optical loop mirror; after [9, 10]
DSF	Dispersion-shifted fiber
EDFA	Erbium-doped fiber amplifier
FFT	Fourier fast transform
FWHM	Full-width at half-maximum
GVD	Group velocity dispersion
NALM	Nonlinear amplifying loop mirror
NNB	Noncentral-negative-binomial distribution
NOLM	Nonlinear optical loop mirror
NRZ	Non-return to zero
NSE	Nonlinear Schrödinger equation
OOK	On-off keying

PC	polarization controller
PM	Polarization-maintaining
RMFL	Regeneratively mode-locked fiber laser
RZ	Return to zero
SNR	Signal-to-noise ratio
SPM	Self-phase modulation
TDM	Time-division multiplexing
WDM	Wavelength-division multiplexing

List of Symbols

A_{eff}	Effective modal area in a fiber
β_2	Second-order dispersion
β_3	Third-order dispersion
β_4	Fourth-order dispersion
χ	Spontaneous emission factor, also known as n_{sp}
G	Power gain of amplifier
$\Gamma(x)$	Gamma function
g	Degeneracy factor
$i = -j$	$= \sqrt{-1}$
$L_m^{g-1}(x)$	Generalized Laguerre polynomial
N	Soliton order
$\bar{n}$	Mean number of ASE photons per mode
$\bar{n}_s$	Mean number of (coherent) signal photons

Chapter 1

Introduction

With the explosive growth of the multimedia-driven World Wide Web, the demand for high bit-rate communications systems is rising exponentially. Following the rapid deployment of residential cable modems and DSL modems that work at the rate of 1.5 Mb/s, the aggregate bit rate in a small neighborhood quickly goes up to the multi-Gb/s range. To satisfy this insatiable demand for bandwidth, new optical networks are being developed and deployed, taking advantage of the low-loss, low-attenuation properties of the optical fiber, as well as the optical gain of the erbium-doped fiber amplifier (EDFA). Using an EDFA as an optical preamplifier in a receiver allows one to achieve unrivaled receiver sensitivities that are about only 3 dB away from the ultimate quantum limit (38 photons/bit), which is truly an amazing feat of engineering accomplishment.

Recently long-distance transmission experiments have demonstrated 64×10 Gb/s transmission where the entire gain bandwidth of EDFA's C-band is utilized. To further increase the total bit rate of a system, major efforts have been made to move from 10 Gb/s (OC-192) to 40 Gb/s (OC-768) in a single channel. As the bit period shrinks from 100 ps to 25 ps, there is clearly a need for a clean short-pulse source. Since most pulse compression schemes generate short pulses with undesirable pedestals that will lead to intersymbol interference, a pulse cleanup device has to be developed.

1.1 Thesis Overview

This thesis will address issues in noise characterization and nonlinear pulse processing in optical communication systems. Chapter 2 provides the necessary background information to understand optical fibers, which is the ideal medium for the transmission of information. Chapter 3 contains experimental results on the photon statistics of receivers that use EDFAs as the preamplifier. A better understanding of the noise processes inside an EDFA allows us to better design our transmission link. Chapter 4 describes a novel nonlinear pulse filter that can clean up pulses, which has found applications in terabit TDM networks as well as gigabit WDM networks. Chapter 5 extends the usage of the pulse filter to clean up ASE noise, whose presence degrades the signal-to-noise ratio and impairs the bit error rate of the system. Chapter 6 contains conclusions and future work. Normalization of the nonlinear Schrödinger equation is covered in Appendix A.

Chapter 2

Background

2.1 Wave Propagation in Optical Fibers

In this chapter, we present the theory of light propagation in an optical fiber. We will develop a mathematical model to describe the evolution of the envelope of a wavepacket in a dispersive medium where the refractive index depends on the field intensity.

We first begin with Maxwell's equations with no sources in an isotropic medium [11],

$$\nabla \cdot \mathbf{D}(\mathbf{r},t) = 0 \tag{2.1}$$

$$\nabla \cdot \mathbf{B}(\mathbf{r},t) = 0 \tag{2.2}$$

$$\nabla \times \mathbf{E}(\mathbf{r},t) = -\frac{\partial \mathbf{B}(\mathbf{r},t)}{\partial t} \tag{2.3}$$

$$\nabla \times \mathbf{H}(\mathbf{r},t) = \frac{\partial \mathbf{D}(\mathbf{r},t)}{\partial t} . \tag{2.4}$$

We can obtain a single partial differential equation for the propagation of the electric field by taking the curl of Eq. (2.3), and using Eqs. (2.1) and (2.4)

$$\nabla^2 \mathbf{E}(\mathbf{r},t) - \frac{1}{c^2}\frac{\partial^2 \mathbf{E}(\mathbf{r},t)}{\partial t^2} = \frac{1}{\epsilon_0 c^2}\frac{\partial^2 \mathbf{P}(\mathbf{r},t)}{\partial t^2} . \tag{2.5}$$

2.2 Linear Dispersion

Since the polarization field in an optical fiber does not respond instantaneously to incident light, that is,

$$\mathbf{P}(z,t) = \epsilon_0 \int_{-\infty}^{+\infty} \chi(t-\tau)\,\mathbf{E}(z,\tau)d\tau \;, \tag{2.6}$$

the susceptibility $\chi(\omega)$ is frequency-dependent. Because of causality, the real and imaginary parts of $\chi(\omega)$ are Hilbert transform pairs

$$\chi_1(\omega) = \frac{1}{\pi}\mathrm{P}\int_{-\infty}^{+\infty} \frac{\chi_2(\omega')\,d\omega'}{\omega'-\omega} \;, \tag{2.7}$$

$$\chi_2(\omega) = -\frac{1}{\pi}\mathrm{P}\int_{-\infty}^{+\infty} \frac{\chi_1(\omega')\,d\omega'}{\omega'-\omega} \;. \tag{2.8}$$

The real part $\chi_1(\omega)$ modifies the propagation speed, whereas the imaginary part $\chi_2(\omega)$ determines the absorption or amplification by the medium. Using the linear dispersion relation

$$\mathbf{D}(z,\omega) = \epsilon_0\mathbf{E}(z,\omega) + \mathbf{P}(z,\omega) = \epsilon_0(\omega)\left[1+\chi(\omega)\right]\mathbf{E}(z,\omega) \;, \tag{2.9}$$

we can rewrite the wave equation (2.5) in the Fourier domain for an axially uniform optical fiber as

$$\nabla^2\mathbf{E}(\mathbf{r},\omega) + \omega^2\mu\epsilon(\rho,\omega)\mathbf{E}(\mathbf{r},\omega) = 0 \;, \tag{2.10}$$

where $\mu\epsilon(\rho,\omega) = \left[1+\chi(\rho,\omega)\right]/c^2$ and $\rho = \sqrt{x^2+y^2}$.

If the electric field is y-polarized and it propagates along the z-direction, we can write

$$\mathbf{E}(\mathbf{r},t) = \hat{\mathbf{y}}\,a(x,y)\,e^{j(\omega t-\beta(\omega)z)} \;. \tag{2.11}$$

Substituting Eq. (2.11) into the wave equation (2.10), we obtain a differential equation that defines the transverse eigenmode $a(x,y)$ in the optical fiber with modal

propagation constant $\beta(\omega)$,

$$\nabla_{\mathrm{T}}^2 a(x,y) + \left[\omega^2 \mu\epsilon(\rho,\omega) - \beta^2(\omega)\right] a(x,y) = 0\,. \tag{2.12}$$

The evolution in z can be obtained by assuming

$$\mathbf{E}(\mathbf{r},\omega) = \hat{\mathbf{y}}\, E(z,\omega)\, a(x,y) \tag{2.13}$$

in Eq. (2.10), which yields a scalar partial differential equation,

$$\frac{\partial^2 E(z,\omega)}{\partial z^2} + \beta^2(\omega) E(z,\omega) = 0\,. \tag{2.14}$$

The modal propagation constant $\beta(\omega)$ depends on frequency in a complicated way, because apart from resonance contributions, waveguide dispersion also plays a significant role. To simplify calculations, we perform a Taylor series expansion of $\beta(\omega)$ around the optical carrier frequency ω_0 away from electronic resonances,

$$\beta(\omega) = \beta(\omega_0) + \beta'(\omega_0)\,(\omega - \omega_0) + \frac{1}{2}\beta''(\omega_0)\,(\omega - \omega_0)^2 + \cdots\,. \tag{2.15}$$

The envelope of the wavepacket moves at the group velocity $v_{\mathrm{group}} = 1/\beta'(\omega_0)$. The parameter $\beta''(\omega_0)$ describes pulse broadening due to dispersion. We can "factorize" and rewrite Eq. (2.14) in the time domain (dropping the term containing $\beta(\omega_0)$) as

$$\frac{\partial E(z,t)}{\partial z} + \frac{1}{v_{\mathrm{group}}}\frac{\partial E(z,t)}{\partial t} = \frac{j}{2}\beta''(\omega_0)\frac{\partial^2 E(z,t)}{\partial t^2}\,. \tag{2.16}$$

Instead of solving Eq. (2.5), a vector partial differential equation in $3+1$ dimensions, we have greatly simplified the problem such that we can now work with Eq. (2.16), a scalar partial differential equation in $1+1$ dimensions.

In Figure 2-1, the dispersion of a single-mode fiber is shown for different material composition and modefield diameter.

The measurement of chromatic dispersion is accomplished by analyzing the group delay through the fiber as a function of wavelength (Fig. 2-2(a)). A wavelength tun-

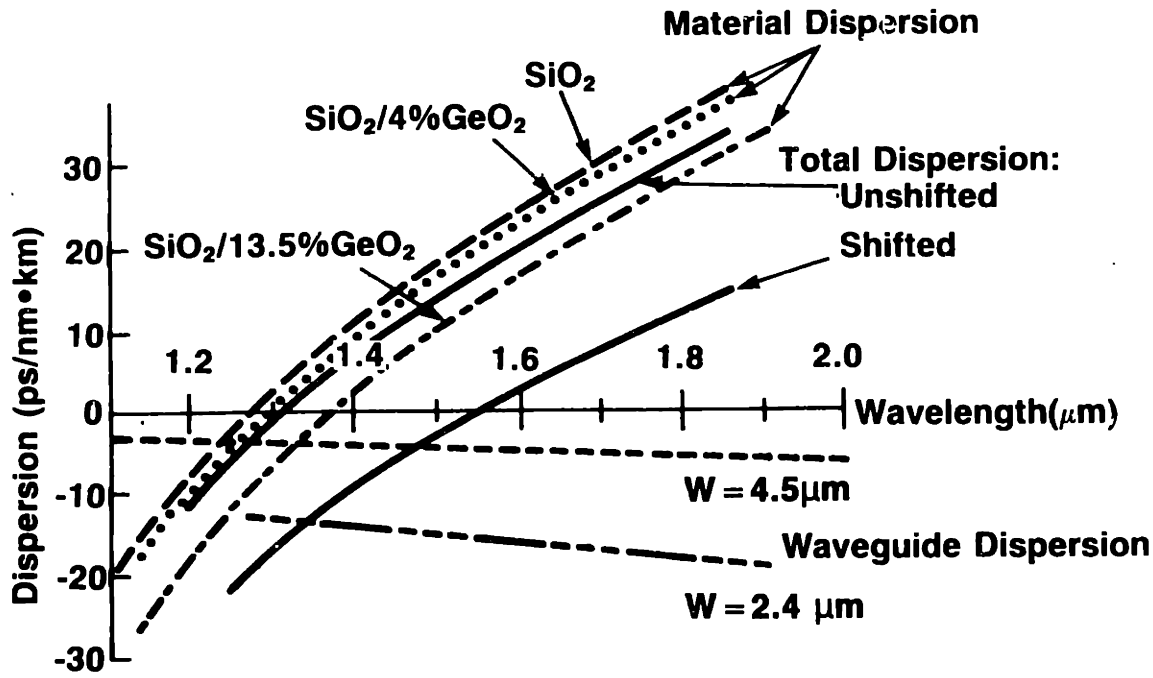

Figure 2-1: Dispersion of single-mode fiber vs. wavelength for different material composition and modefield diameter, after Ref. [1]. Note that the dispersion parameter is defined as $D = -\frac{2\pi c}{\lambda^2}\beta''(\omega_0)$.

able optical source is intensity modulated as the input stimulus for the fiber under test, while the phase of the detected modulation signal is then compared to that of the input electrical modulation. By measuring how this phase changes with wavelength, the group delay of the fiber is easily measured. Fig. 2-2(b) shows the relative group delay vs. wavelength for 1550 nm dispersion-shifted fiber (DSF). One can see clearly that above 1550 nm, the chromatic dispersion is anomalous, where the "blue component" is traveling faster than the "red component". Finally, the disperion parameter,

$$D = -\frac{2\pi c}{\lambda^2}\beta''(\omega_0) \ , \tag{2.17}$$

is evaluated from group delay data and plotted in Fig. 2-2(c).

2.3 Self-Phase Modulation

The response of an isotropic optical fiber to an external electric field becomes nonlinear when the field is intense (comparable to the internal atomic field). This nonlinear-

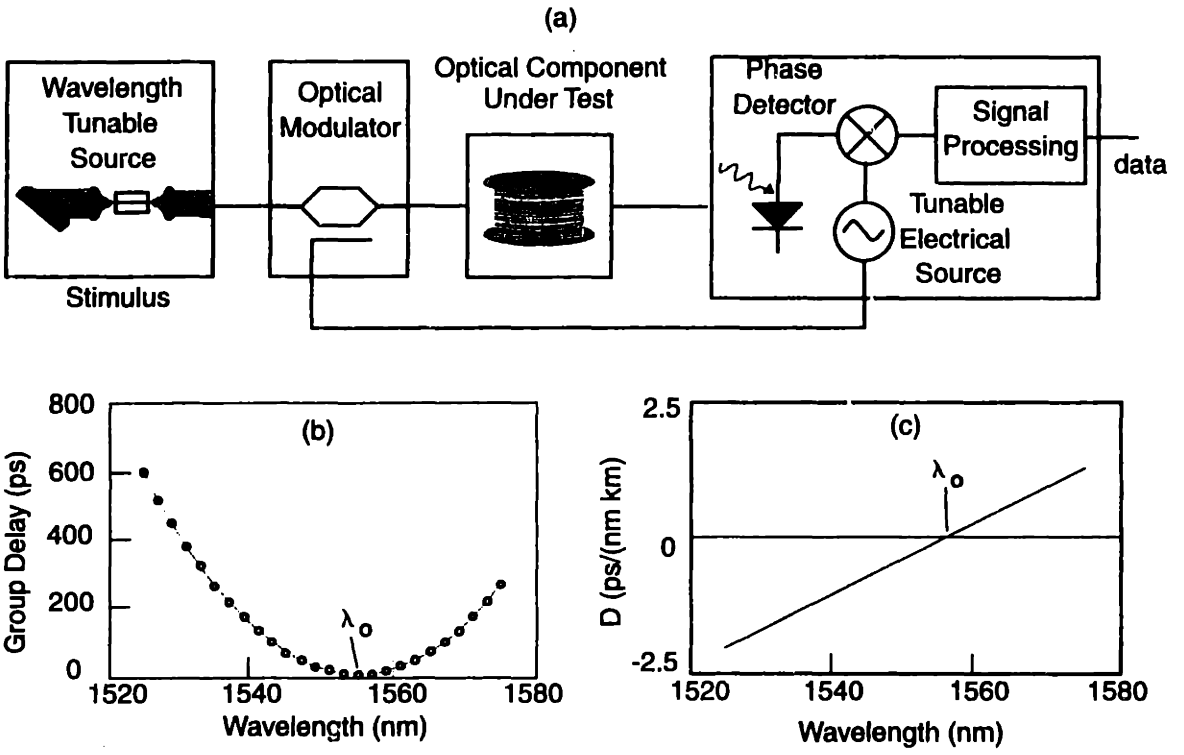

Figure 2-2: (a) Chromatic dispersion measurement of a 2-port optical device around 1.5 μm. (b) Relative group delay vs. wavelength. (c) Dispersion (in ps/nm/km) vs. wavelength. λ_0 is the zero-dispersion wavelength; after Ref [2].

ity originates from the anharmonic motion of bound electrons under the influence of an applied field. Self-phase modulation, one of the nonlinear effects, can be modeled as

$$\mathbf{P}^{\mathrm{NL}}(z,\omega) = \epsilon_0 \chi^{(3)} \left|\mathbf{E}(z,\omega)\right|^2 \mathbf{E}(z,\omega) \tag{2.18}$$

where $\chi^{(3)}$ is real and positive.

What happens physically is that the refractive index becomes dependent on the optical intensity. As a result, when an optical pulse propagates, its peak will acquire more phase shift than its wings will. Self-phase modulation plays an essential role in optical soliton formation. One can incorporate this nonlinearity into the wave equation by defining

$$\mathbf{D}(z,\omega) = \epsilon_0(\omega)\left[1+\chi^{(1)}(\omega)\right]\mathbf{E}(z,\omega) + \mathbf{P}^{\mathrm{NL}}(z,\omega)\ , \tag{2.19}$$

which yields the cubic nonlinear Schrödinger equation

$$\frac{\partial E(z,t)}{\partial z} + \frac{1}{v_{\mathrm{group}}}\frac{\partial E(z,t)}{\partial t} - \frac{j}{2}\beta''(\omega_0)\frac{\partial^2 E(z,t)}{\partial t^2} = -j\frac{\omega}{2nc}\chi^{(3)}\left|E(z,t)\right|^2 E(z,t)\ . \tag{2.20}$$

It is evident from the right hand side of Eq. (2.20) that the optical Kerr effect is a reactive process which produces an additional phase shift proportional to the optical intensity.

2.4 Optical Solitons

In a lossless medium with anomalous dispersion where $\beta''(\omega_0) < 0$, lower frequency components of an optical pulse trail higher frequency components. Thus, in a linear medium, the pulse will broaden indefinitely as it propagates. On the other hand, in a Kerr medium, self-phase modulation produces a positive chirp across the central portion of the pulse. It is possible to find a steady-state pulse shape where the amount of self-phase modulation balances the effect of dispersion exactly. The pulse then propagates undistorted in the form of an optical soliton.

To show that soliton solutions exist for Eq. (2.20), we first normalize the equation according to (see Appendix A for more details)

$$z_n = \frac{z - v_{\text{group}} t}{z_c} \tag{2.21}$$

$$t_n = \frac{t}{t_c} \tag{2.22}$$

$$u_n = \frac{E}{E_0} \tag{2.23}$$

and choose z_c, t_c, and E_0 such that both conditions

$$|\beta''(\omega_0)| \frac{z_c}{t_c^2} = 1 \tag{2.24}$$

and

$$\frac{\omega}{2nc} \chi^{(3)} E_0^2 z_c = 1 \tag{2.25}$$

are satisfied. The normalized nonlinear Schrödinger equation then takes a simple form

$$j \frac{\partial u_n}{\partial z_n} = \frac{1}{2} \frac{\partial^2 u_n}{\partial t_n^2} + |u_n|^2 u_n \ . \tag{2.26}$$

In 1972, Zakharov and Shabat [12] applied the technique of inverse scattering [13] to solve the above nonlinear partial differential equation. Their analytical solutions revealed that the amplitude and the velocity of interacting/colliding solitons did not change, whereas their phases contained discontinuities. The fundamental soliton is the simplest form of an extensive family of exact solutions of Eq. (2.26). It has an hyperbolic secant form

$$u(z_n, t_n) = \text{sech}(t_n)\, e^{-jz_n/2} \ . \tag{2.27}$$

Chapter 3

Photon Statistics in an Optically Pre-amplified Receiver

3.1 Motivation

The determination of receiver sensitivity and bit-error rate (BER) is important in the design of high bit rate optical digital communication systems. After the introduction of the erbium-doped fiber amplifier (EDFA), optical communication systems at the 1.5 μm wavelength is now widely based on intensity modulation and direction detection, instead of relying on coherent techniques [14]. By using an EDFA at the transmitter, signals can be boosted to high optical levels before transmission. As well, fiber attenuation can be compensated with EDFAs that are placed in the fiber span. Finally, by using an EDFA as a pre-amplifier at the receiver, excellent sensitivity as low as 76 photons/bit can be obtained experimentally [3]. Also, at wavelengths near 1.3 μm, an optically pre-amplified receiver using Raman gain is reported to have a sensitivity of 151 photons/bit [15]. As with other types of amplifiers, optical amplifiers introduce noise resulting from spontaneous emission in the amplifying region, which degrades the system's SNR and thus impairs BER.

In Fig. 3-1, the eye diagram of a typical 10 Gb/s NRZ transmission is shown. The horizontal axis is time (20 ps/div). Overlaid on the eye diagram is the histogram of "hits" sampled at the middle of the bit period in a predefined time window. From

the eye diagram, one can obtain the histogram and the probability distributions of the ZEROs and the ONEs, which will then enable one to deduce the bit error rate of the system.

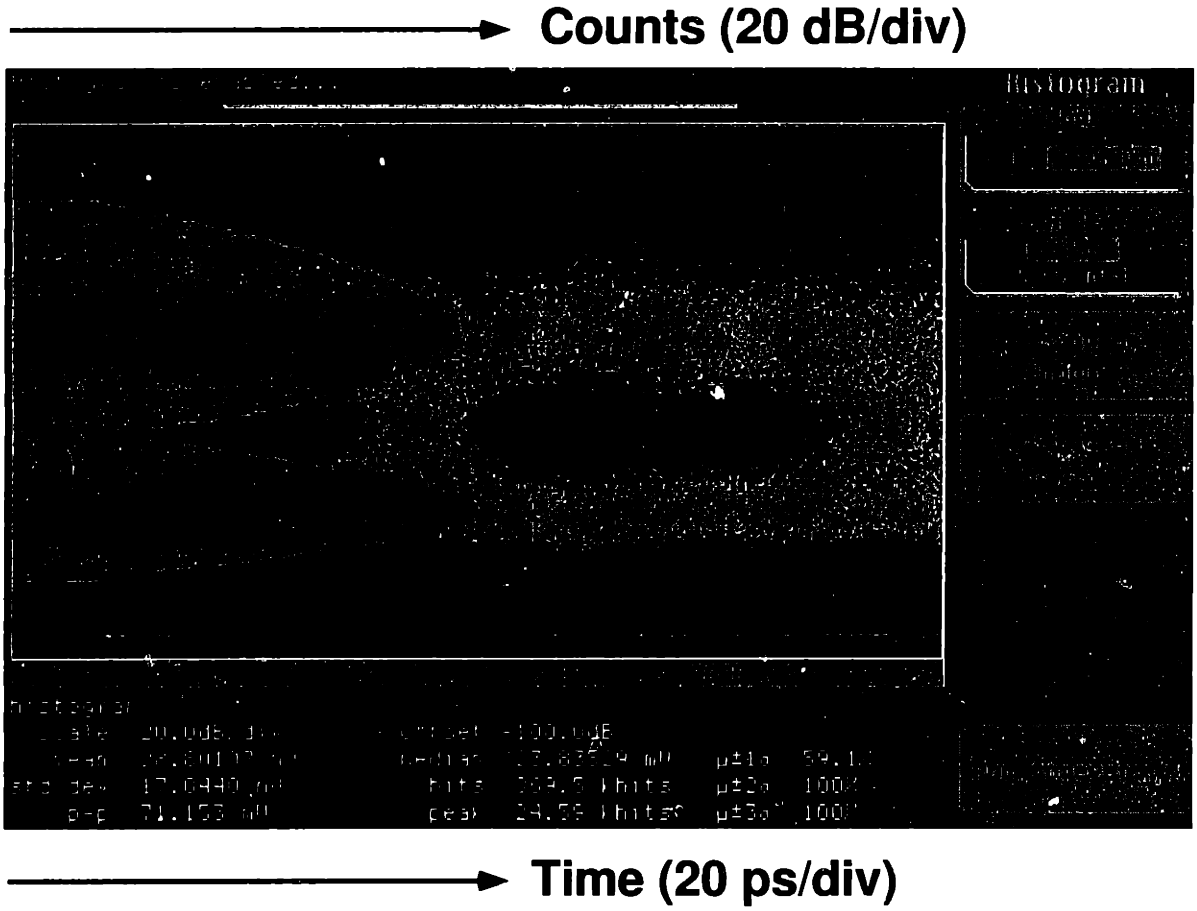

Figure 3-1: Eye diagram of a typical 10 Gb/s NRZ transmission. The horizontal axis is time (20 ps/div); the vertical axis is voltage (arb. units).

There exist two classes of models for modeling the probability distribution of received signals in a pre-amplified OOK (on-off keying) receiver. The first class uses the semiclassical square-law model for detection, resulting in a Gaussian distribution for the photocurrent [16–19]. The second class uses a quantum treatment of spontaneous and stimulated processes in the optical amplifier [20–22]. The advantages of the semiclassical models are simplicity and the fact that they yield approximate yet analytical expressions for the BER. The advantage of the quantum mechanical models is correctness and accuracy in describing the physical processes.

We will confirm experimentally the non-Gaussian nature of the ASE photon dis-

tribution by showing that it is degenerate Bose-Einstein, a quantum-mechanical prediction [23]. Later, we will further demonstrate experimentally that the photon distribution of the ONEs state in an OOK pre-amplified receiver is non-Gaussian, and can be described quantum mechanically by a noncentral-negative-binomial distribution. We would like to demonstrate the accuracy of the quantum mechanical receiver models describing both the ZEROs and ONEs.

The ASE noise of an optical amplifier is Bose-Einstein distributed [24]. In thermal equilibrium at temperature T, the probability $p_{BE}(m)$ that a harmonic oscillator is thermally excited to the m-th excited state is given by the Boltzmann factor

$$p_{BE}(m) = \frac{\exp(-E_m/k_BT)}{\sum_m \exp(-E_m/k_BT)} . \tag{2.1}$$

Using the expression for the mean photon number (collected in a time interval given by the inverse detector bandwidth)

$$\bar{n} = \frac{1}{\exp(\hbar\omega/k_BT) - 1} , \tag{3.2}$$

one can rewrite $p_{BE}(\bar{n}, m)$ as

$$p_{BE}(\bar{n}, m) = \frac{\bar{n}^m}{(1+\bar{n})^{1+m}} . \tag{3.3}$$

For polarized ASE light incident on a photodetector, if the optical filter bandwidth is g times wider than the inverse response time of the photodetector, the Bose-Einstein process becomes g-fold degenerate. The resulting photon probability distribution is then the convolution of the individual distributions over m, which can be stated in closed form as [20–22, 25]

$$p_{BE}(\bar{n}, g, m) = \frac{\Gamma(m+g)}{\Gamma(m+1)\Gamma(g)} \left(1 + \frac{1}{\bar{n}}\right)^{-m} (1+\bar{n})^{-g} \tag{3.4}$$

where $\Gamma(x)$ is the gamma function. The degenerate Bose-Einstein distribution in Eq. (3.4) is also known as the negative-binomial distribution [20, 22, 25]. The average

number of photons in all of the modes is $g\bar{n}$ (see Fig. 3-2), while the mean square fluctuations in photon number are

$$\left\langle \Delta m^2 \right\rangle = g\left(\bar{n} + \bar{n}^2\right) . \tag{3.5}$$

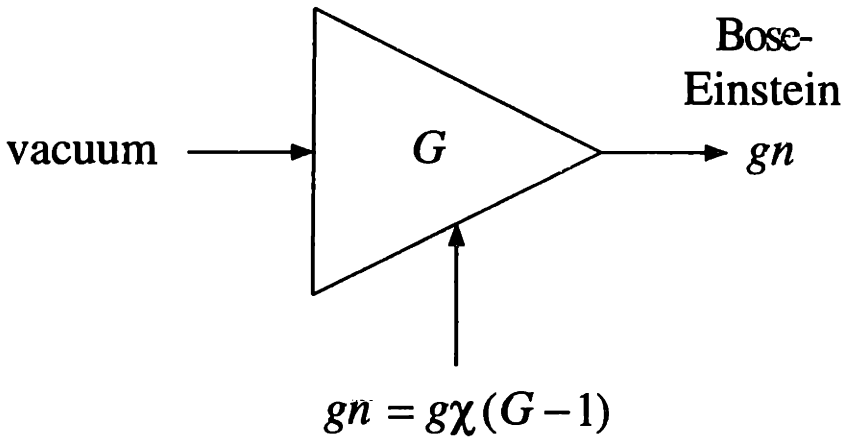

Figure 3-2: The amplified ZEROs are described by the Bose Einstein distribution. The Gaussian model tends to underestimate the upper tail of the probability distribution of the ZEROs.

For an optical amplifier with a power gain of G, the mean photon number in each mode is $\bar{n} = \chi(G-1)$, where χ is the noise enhancement factor for incomplete inversion of the gain medium. In the case of the erbium-doped fiber amplifier (EDFA) used in this experiment, χ is measured to be 1.4. For conventional lightwave receivers where the ASE noise is unpolarized, the degeneracy factor has to be doubled because of the additional degree of polarization.

On the other hand, optically amplified coherent light (ONEs) exhibits different statistics. When a ONE bit containing $\bar{n}_s$ photons is pre-amplified with a power gain of G in a receiver, its statistics are described by the noncentral-negative-binomial (NNB) distribution [20, 22, 25]:

$$p_{NNB}(\bar{n}, g, \bar{n}_s, m) = \frac{\bar{n}^m}{(1+\bar{n})^{m+g}} \exp\left(-\frac{G\bar{n}_s}{1+\bar{n}}\right) \cdot L_m^{(g-1)}\left[-\frac{G\bar{n}_s}{\bar{n}(1+\bar{n})}\right] \tag{3.6}$$

where

$$L_m^{(g-1)}(x) \equiv \sum_{k=0}^{m} (-x)^k (m+g-1)!/[(k+g-1)!(m-k)!k!] \tag{3.7}$$

is the generalized Laguerre polynomial. The average number of photons in the output is $G\bar{n}_s + g\bar{n}$(see Fig. 3-3), while the mean square fluctuations are

$$\left\langle \Delta m^2 \right\rangle = G\bar{n}_s + 2G\bar{n}_s\bar{n} + g\bar{n}\,(1+\bar{n}) \ . \tag{3.8}$$

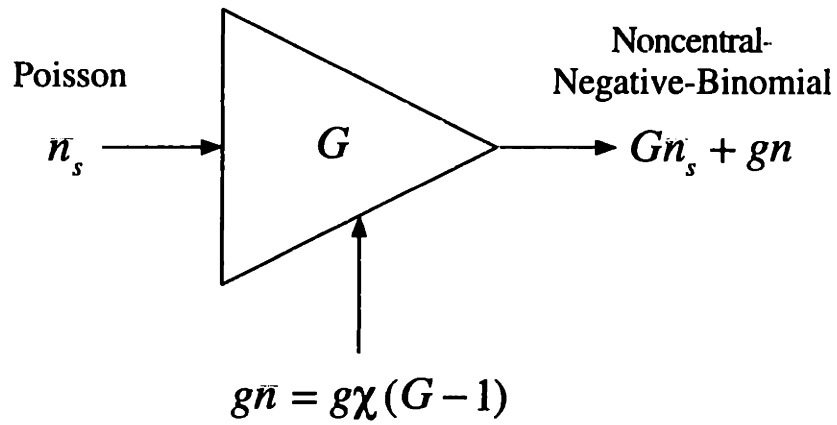

Figure 3-3: The amplified ONEs are described by the noncentral-negative-binomial distribution. The Gaussian model tends to overestimate the lower tail of the probability distribution of the ONEs.

The first term contributing to the fluctuations is identified as the shot noise of the amplified signal, while the second and the third terms are the signal-ASE beat term and the ASE-ASE beat term, respectively [14].

3.2 Steady-state/cw Measurement

The experimental setup is shown in Fig. 3-4. The receiver consists of an optical attenuator to adjust the received power, an EDFA pre-amplifier pumped at 980 nm, an optical bandpass filter with center wavelength 1550 nm and 3-dB bandwidth of 1.0 nm to provide rejection of out-of-band noise, a 30 GHz *pin* detector with a conversion gain of 24.83 V/W, and a 30 GHz dc-coupled digital sampling oscilloscope. A second optical attenuator is used to prevent the *pin* detector from saturating. For calibration, we measure the detection circuit's thermal circuit noise by blocking the detector input and obtaining the distribution of voltages on the oscilloscope. The voltage levels are then converted to a noise equivalent optical power, whose histogram is shown in Fig. 3-

5. The circuit noise distribution is found to be Gaussian with a standard deviation of 12.5 μW, or a noise equivalent power of 72 pW/$\sqrt{\text{Hz}}$, which is expected since thermal circuit noise is Gaussian [26]. Although the measured standard deviation of circuit noise at the receiver is within the manufacturer's specifications, it is about 4 times the standard deviation of the minimum theoretical thermal noise at room temperature, which is evaluated to be 0.13 mV. The fitting algorithm used throughout this chapter is the Levenberg-Marquardt method [27, 28]. The line search algorithm is a mixed quadratic and cubic polynomial interpolation and extrapolation method.

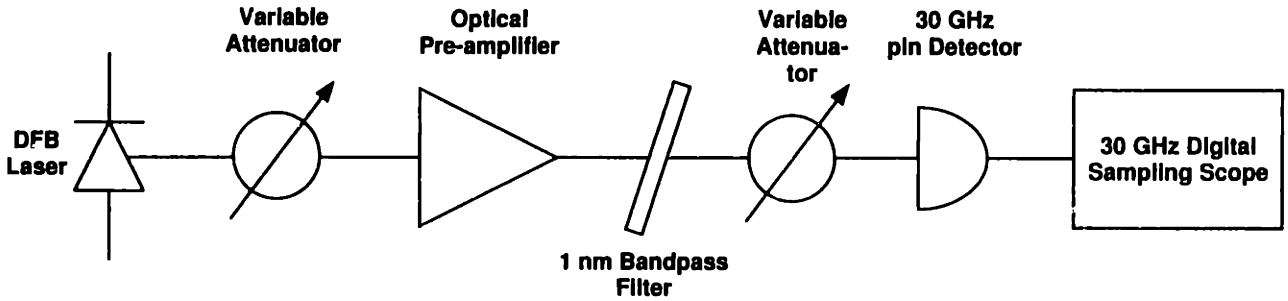

Figure 3-4: Experimental setup.

The photon distribution of ASE noise of the pre-amplifier on the oscilloscope is obtained by blocking the incident light at the pre-amplifier and unblocking the *pin* detector. Using the previously measured circuit noise distribution, the theoretical distribution of the ASE noise is computed by convolving the degenerate Bose-Einstein distribution in Eq. (3.4) with the Gaussian distribution obtained in Fig. 3-5. The ASE histogram data, collected with 10^7 hits, are then fitted with this composite distribution, shown in Fig. 3-6 in a logarithmic scale. The two degrees of freedom used in fitting are the mean photon number per mode $\bar{n}$ and the degeneracy factor g. The parameter $\bar{n}$ is found to be 2035, and g is 8.5, which is very close to the expected value of the optical bandwidth divided by the electrical bandwidth while accounting for the two degrees of polarization (125 GHz/30 GHz $\times 2 = 8.3$).

Next, the photon distribution of the amplified ONEs is obtained by injecting -36 dBm of coherent light ($\bar{n}_s = 63$) from a DFB laser at 1550 nm into the receiver. The histogram data are shown in Fig. 3-7, from which one can clearly see the non-Gaussian nature of the distribution. The NNB fit, agreeing very well with the experimental

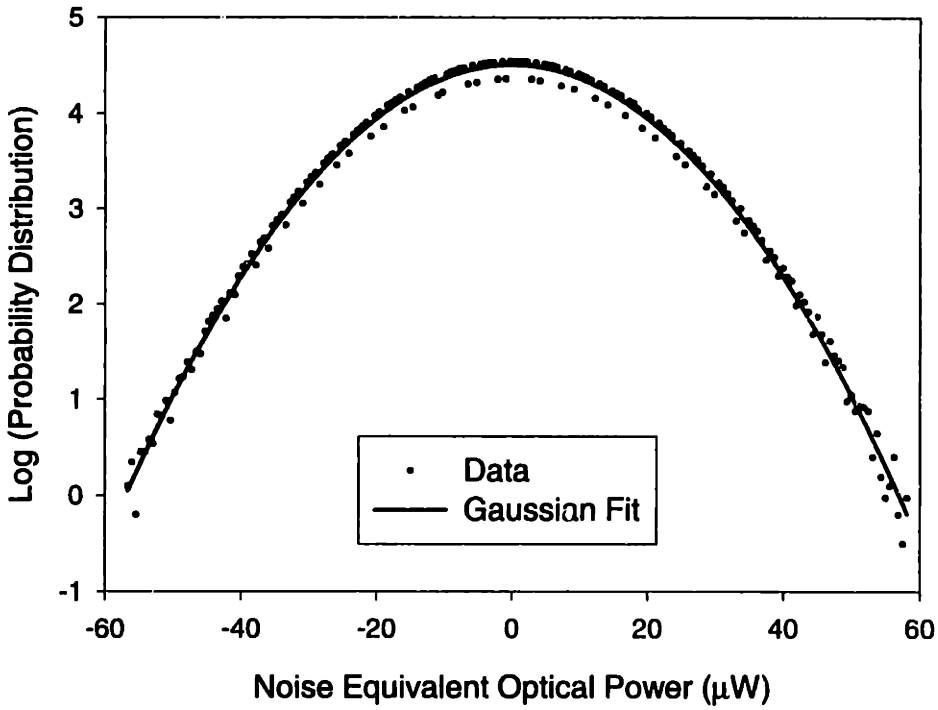

Figure 3-5: Probability distribution of the detector's thermal circuit noise (circles) and a Gaussian fit (solid line). Electrical bandwidth: from dc to 30 GHz. From curve fit, standard deviation is 12.5 μW.

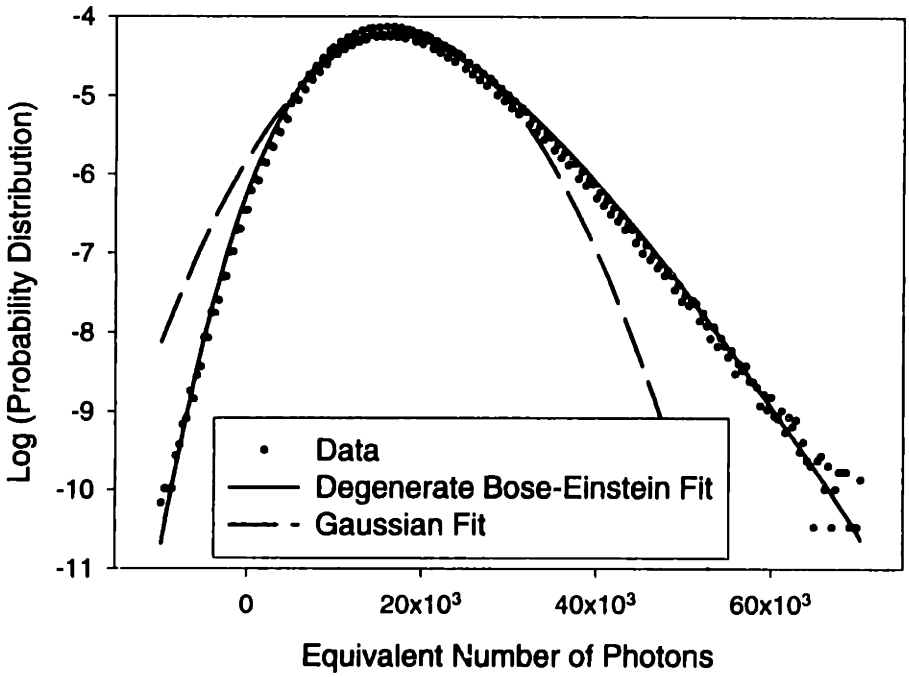

Figure 3-6: Probability distribution of the ASE/ZEROs (circles), a degenerate Bose-Einstein fit (solid line), and a Gaussian fit (dotted line) From curve fit, $\bar{n} = 2035$ and $g = 8.5$.

data over a dynamic range of 58 dB, yields $\bar{n} = 2110$, $g = 8.7$, and $\bar{n}_s = 60$. The extracted value of $g = 8.7$ in the ONEs is very close to the value of $g = 8.5$ that is obtained in the ZEROs. On the other hand, one can see that the Gaussian fit to the data is not satisfactory. As pointed out theoretically in Refs. [20–22], around the optimal decision threshold, the Gaussian model tends to underestimate the tails of the probability distributions of the ZEROs while overestimating those of the ONEs.

Next, a polarizer is inserted between the optical bandpass filter and the *pin* detector. It is oriented such that the amount of signal transmitted is maximized. Since ASE is unpolarized whereas the amplified signal is polarized, one would expect that half of the ASE noise is blocked by the polarizer. As shown in Figs. 3-8 and 3-9, this is indeed the case. The degeneracy factor g obtained from the curve fit is now 4.1, which is about half as much as before.

On the other hand, the use of a polarizer in a practical receiver proves to be not a good idea. First of all, it is not always possible to orient the polarizer to maximize

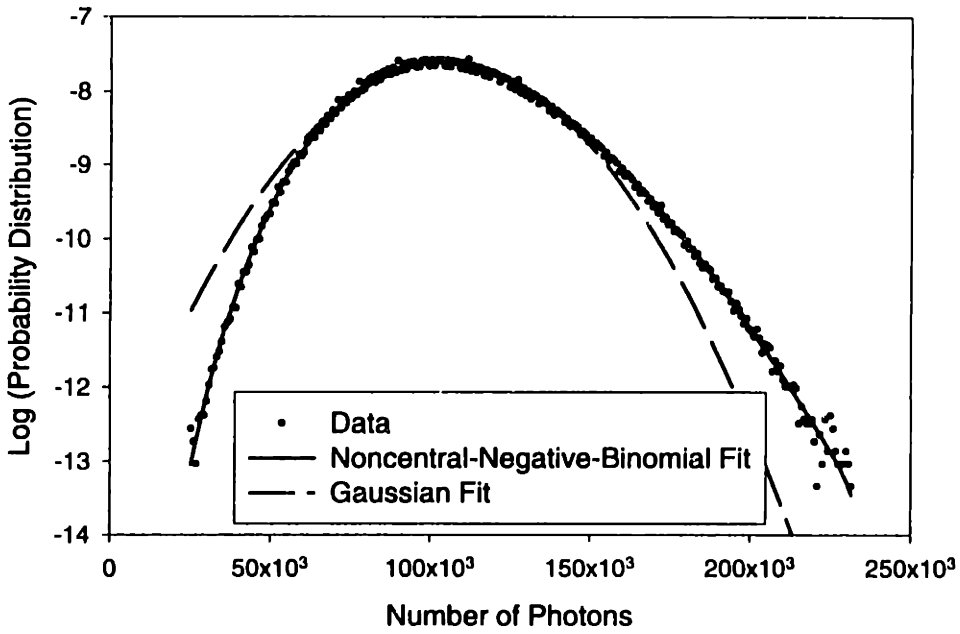

Figure 3-7: Probability distribution of the ONEs (circles), a noncentral-negative-binomial fit (solid line), and a Gaussian fit (dotted line). From curve fit, $\bar{n} = 2108$, $g = 8.7$, and $\bar{n}_s = 60$.

signal transmission as the signal may be coming from several sources, each having its own state of polarization. Second, the dominant noise term in a well-designed receiver is the signal-ASE beat term, which is independent of the degeneracy factor g. The physical understanding is that the signal does not beat with the part of the ASE noise that has the orthogonal polarization.

Since the Gaussian model tends to underestimate the tails of the probability distributions of the ZEROs while overestimating those of the ONEs, one expects that the optimal decision threshold predicted will be *lower* than that predicted by the quantum model. As shown in Fig. 3-10, the two predictions can differ by more than a factor of two at low degeneracies. On the other hand, due to a cancellation of errors in the Gaussian model the two models predict virtually the same number of photons/bit required to achieve a 10^{-9} BER.

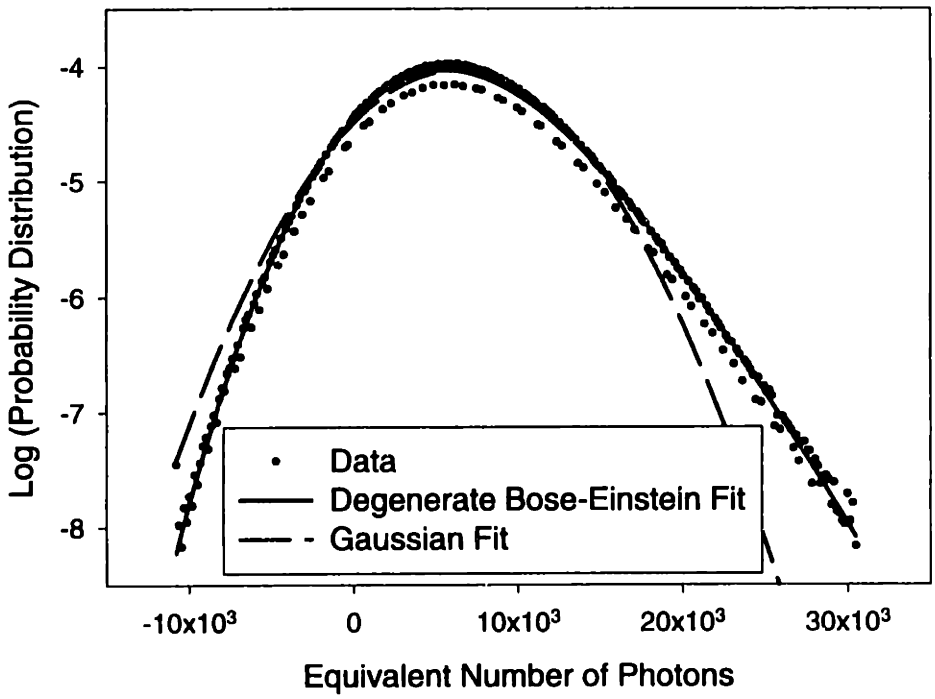

Figure 3-8: Probability distribution (obtained with a polarizer) of the ASE/ZEROs (circles), a degenerate Bose-Einstein fit (solid line), and a Gaussian fit (dotted line). From curve fit, $\bar{n} = 1510$ and $g = 4.1$.

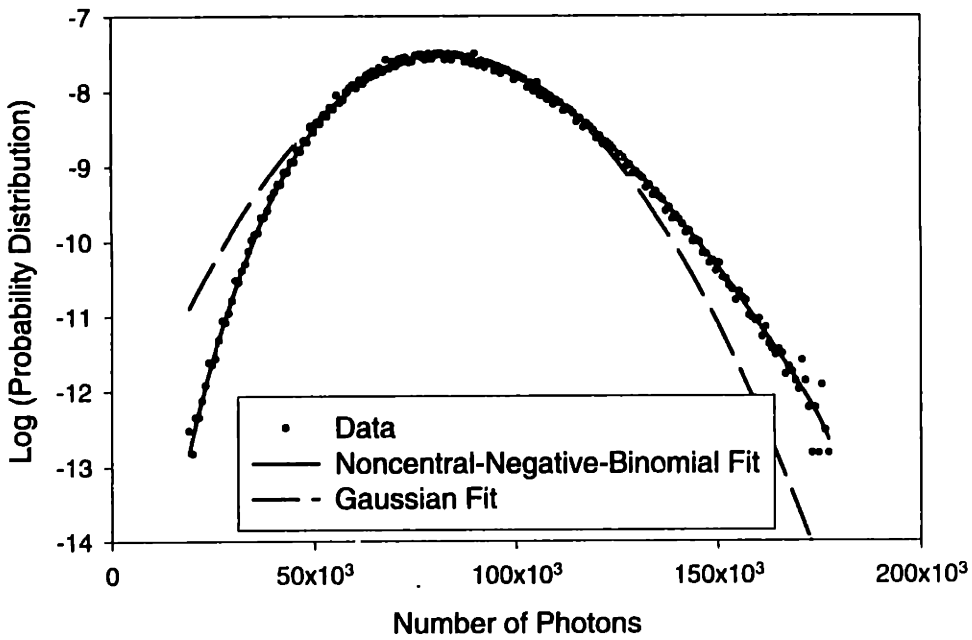

Figure 3-9: Probability distribution (obtained with a polarizer) of the ONEs (circles), a noncentral-negative-binomial fit (solid line), and a Gaussian fit (dotted line). From curve fit, $\bar{n} = 1610$, $g = 4.1$, and $\bar{n}_s = 69$.

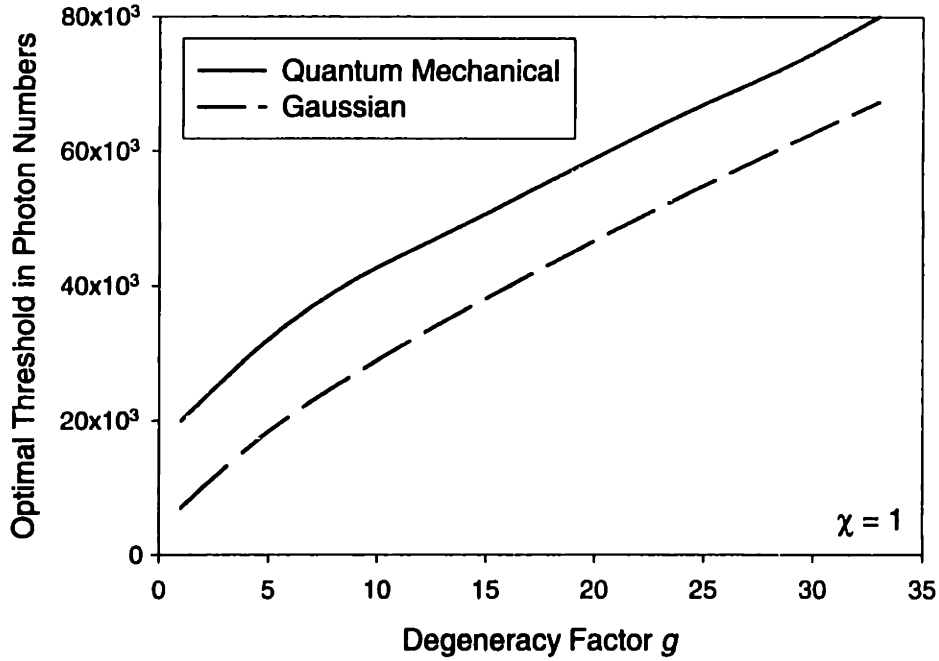

Figure 3-10: Optimal decision threshold calculations using the quantum mechanical model.

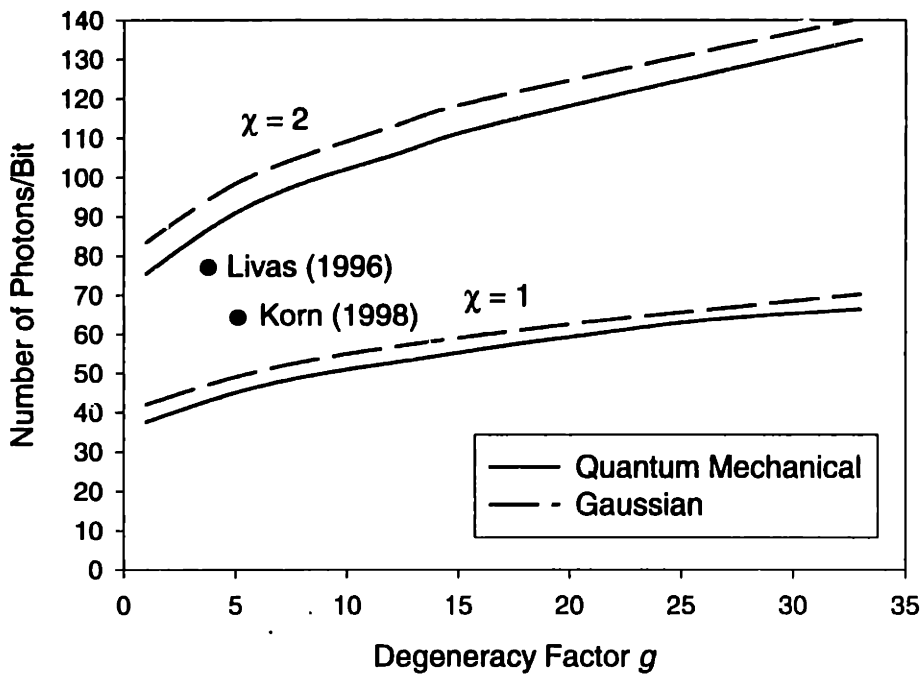

Figure 3-11: Predicted number of photons/bit required to achieve a 10^{-9} BER. J. Livas reported a sensitivity of 76 photons/bit [3]; more recently, J. Korn reported 67 photons/bit [4] using the RZ format.

3.3 Back-to-back NRZ and RZ Transmission Experiments

3.3.1 NRZ Transmission

After demonstrating good agreement between theory and experiment on steady-state probability distributions of ZEROs and ONEs, we now attempt to study the probability distributions when modulation is applied to the source. In our NRZ experiment, the DFB laser at 1550.9 nm is modulated at 10 Gb/s by a lithium niobate modulator with a $2^{31} - 1$ pseudorandom bit sequence. The optical pre-amplifier is made by OPREL, which has a 3.5 dB noise figure. A 1.0 nm optical bandpass filter is inserted after the pre-amplifier to filter out the out-of-band ASE noise. The detector is a Lasertron ac-coupled *pin*, and it is amplified by an Anritsu wideband rf amplifier (30 kHz – 10 GHz).

The BER curve for the NRZ case is shown in Fig. 3-12. The sensitivity at 10^{-9} BER is -38.7 dBm, or 105 photons/bit. The eye diagram as well as the histogram of ZEROs and ONEs are shown in Fig. 3-13(a). Since the optical power incident on the *pin* detector is as high as 3.0 dBm, the output voltage of the *pin* detector becomes saturated and clipping results. The probability distribution for the ONEs does not resemble the NNB distribution at all. After attenuating the optical power to -4.1 dBm with an optical attenuator, the detector is no longer saturated (Fig. 3-13(b)). However, the receiver sensitivity increases by 0.4 dBm, mostly due to the relative increase of thermal noise present in the detector's output.

3.3.2 RZ Transmission

We repeat the above experiment with the RZ data format as well. The RZ source is an external-cavity mode-locked semiconductor laser that produces 4 ps pulses at 10 GHz. We also switch to the dc-coupled HP Lightwave Converter as we think that it is better matched to RZ pulses than the Lasertron is. The sensitivity of RZ transmission is excellent (Fig. 3-12): sensitivity at 10^{-9} BER is 88 photons/bit (-40.0

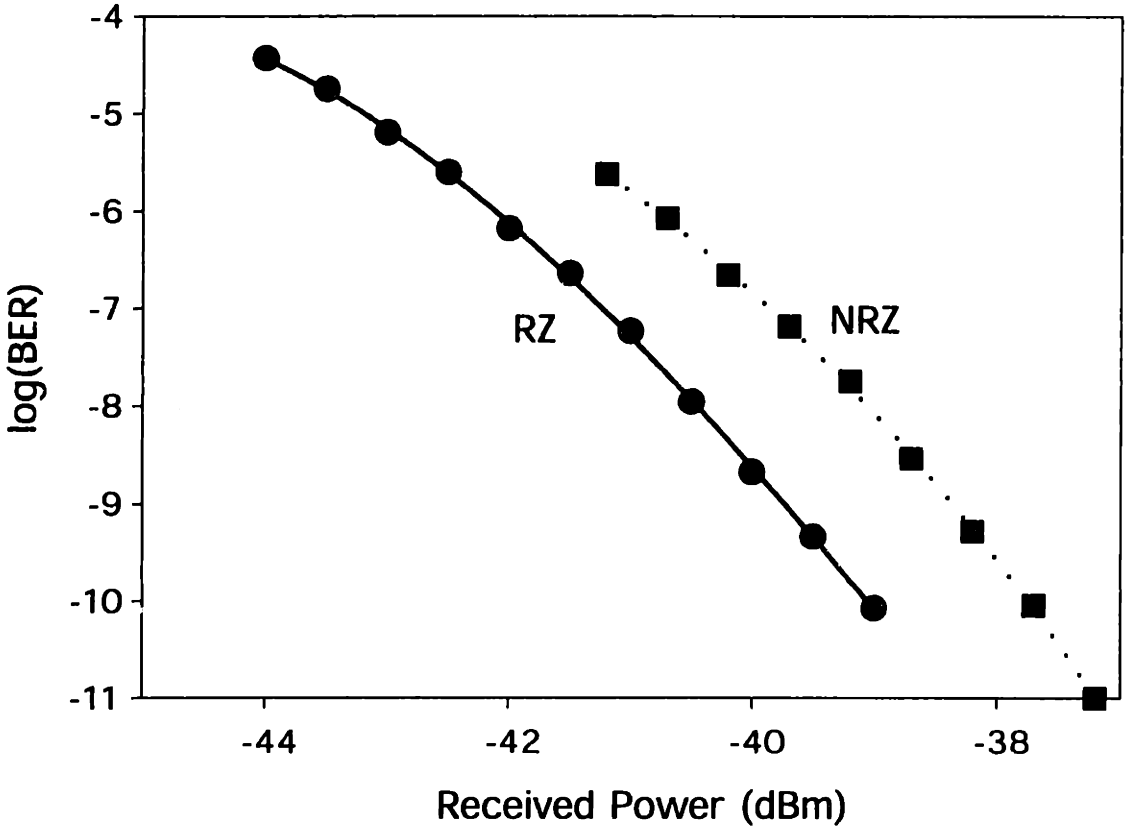

Figure 3-12: Back-to-back bit error rate curves for RZ and NRZ at 10 Gb/s. The receiver sensitivities at 10^{-9} BER are -38.7 dBm (105 photons/bit) for NRZ, and -40.0 dBm (88 photons/bit) for RZ.

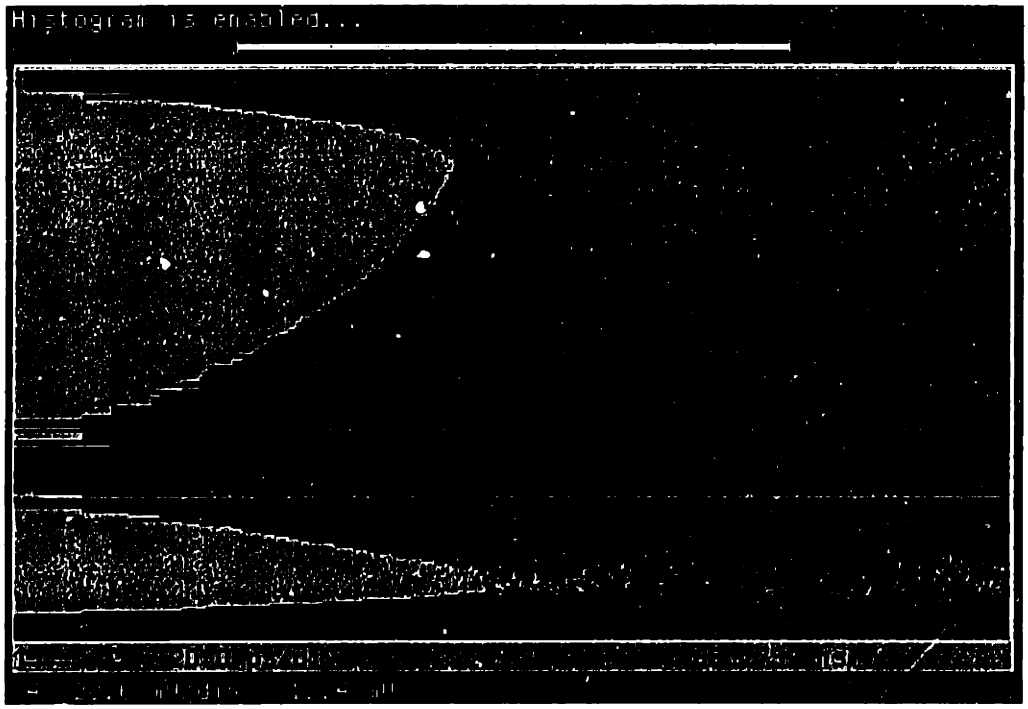

(a) Optical power at the *pin* detector = +3.0 dBm

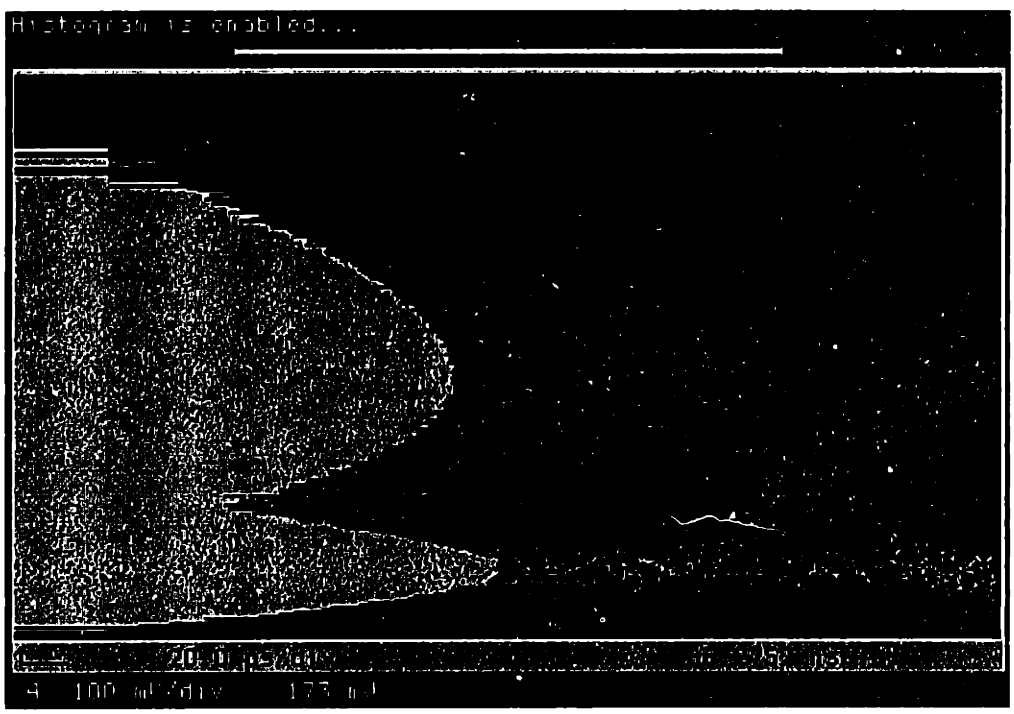

(b) Optical power at the *pin* detector = −4.1 dBm

Figure 3-13: Eye diagram of NRZ transmission at 10 Gb/s. The horizontal axis is time (20 ps/div); the vertical axis is voltage (arb. units).

dBm). The 1.3 dB difference in sensitivities between the RZ and the NRZ formats can be attributed to the fact that there is less intersymbol interference in the RZ case as the RZ pulses are much shorter than the 100 ps duration of the bit period at 10 Gb/s. L. Boivin [29] also observed similar gain in receiver sensitivity when switching from the NRZ to the RZ format.

At high input optical power (+3.0 dBm) to the detector, some saturation of the detector's output is observed (Fig. 3-14(a)). Lowering the optical power to -4 dBm produces the familiar asymmetric probability distribution of the ONEs (Fig. 3-14(b)). The probability distributions for the ONEs and ZEROs are re-plotted in Fig. 3-15, along with the theoretical estimates based on the physical parameters measured: $\bar{n} = 5 \times 10^3$, $g = 25$, $\bar{n}_s = 200$, and $\chi = 1.3$. From the two plots, one can see that the measured 88 photons/bit (-40.0 dBm) probability distributions have a larger variance. We think that it is due to i) pattern-dependent effects in the electronics, and ii) detector ringing (see Fig. 3-16). Naturally, the widened probability distributions contribute to a slightly higher BER than is predicted by theory.

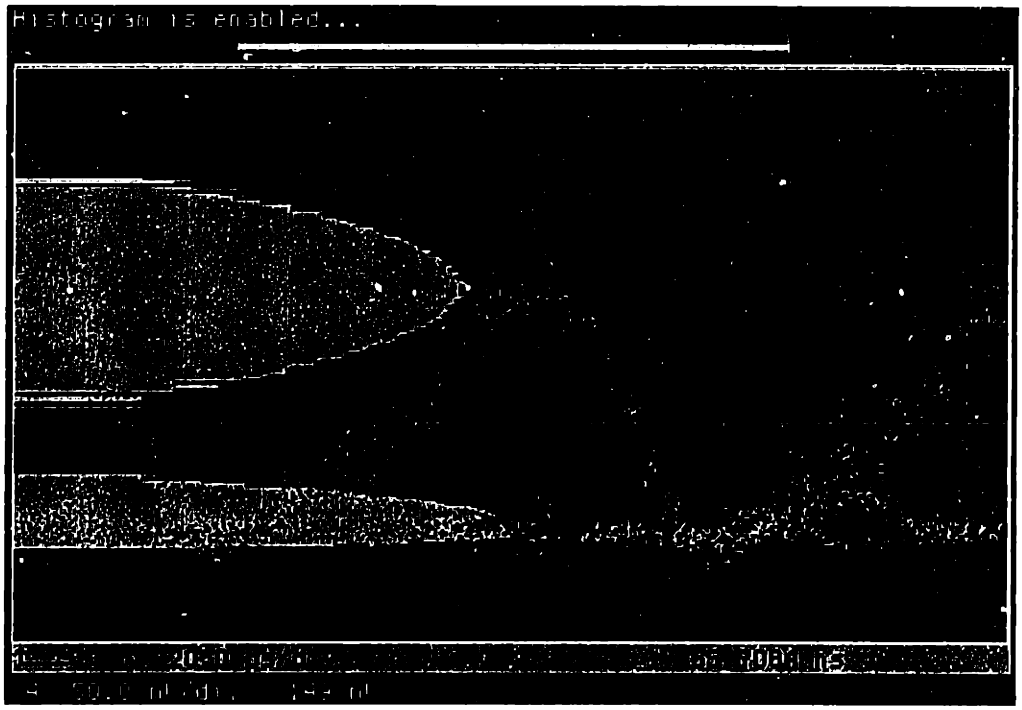

(a) Optical power at the *pin* detector = +3.0 dBm

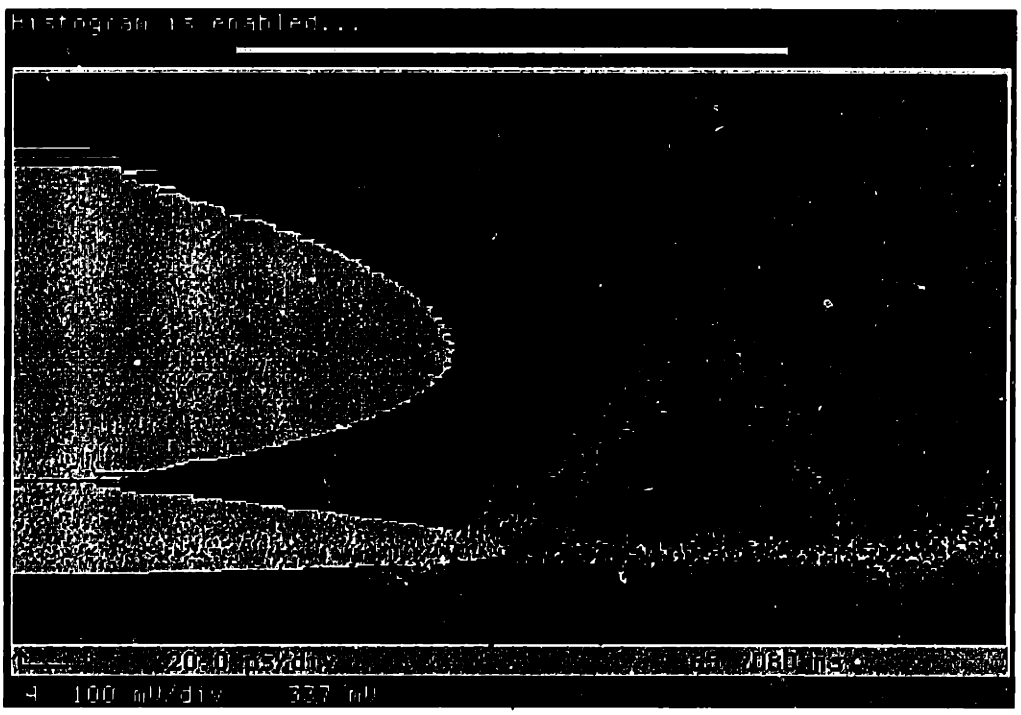

(b) Optical power at the *pin* detector = −4.0 dBm

Figure 3-14: Eye diagram of RZ transmission at 10 Gb/s. The horizontal axis is time (20 ps/div); the vertical axis is voltage (arb. units).

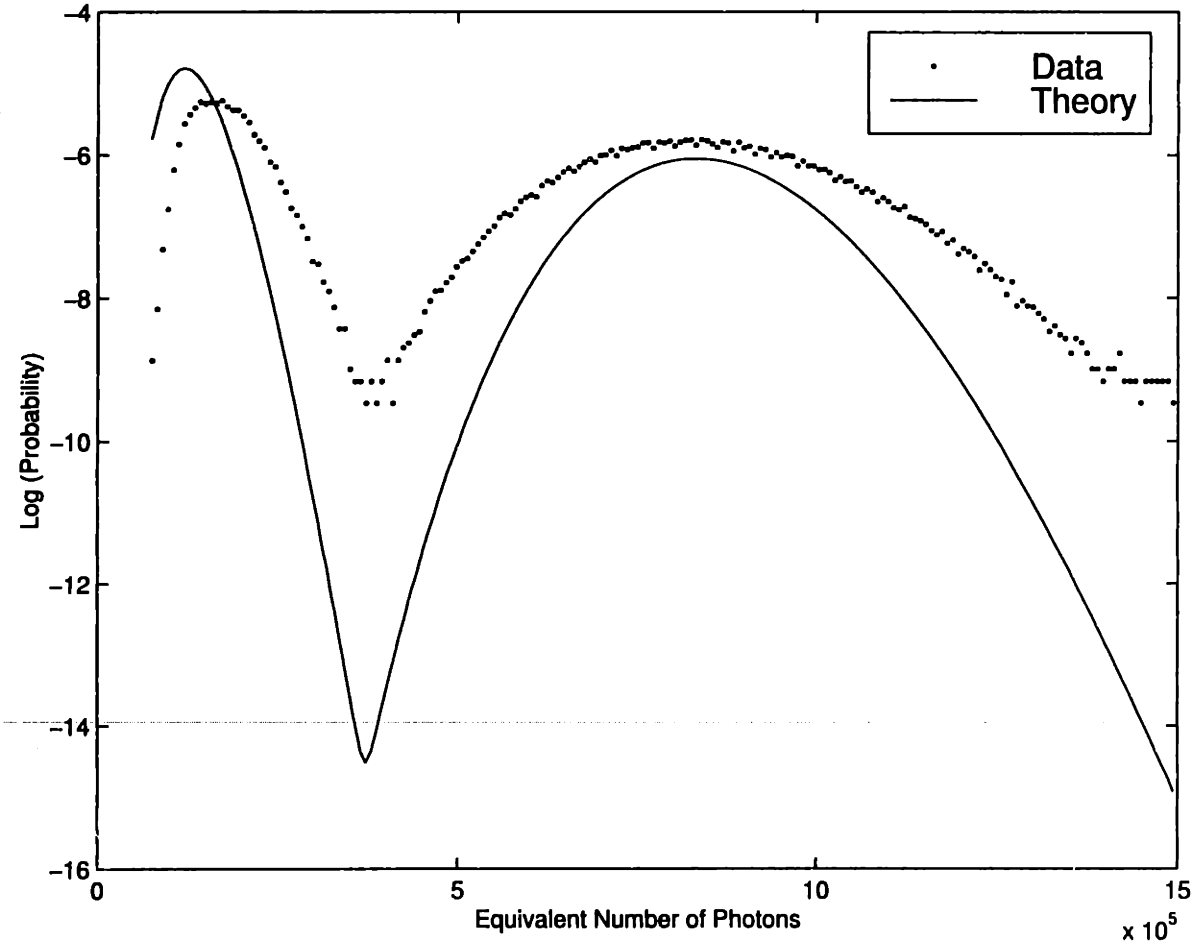

Figure 3-15: RZ eye diagrams: data vs. theoretical estimates. The estimates are $\bar{n} = 5 \times 10^3$, $g = 25$, $\bar{n}_s = 200$, and $\chi = 1.3$.

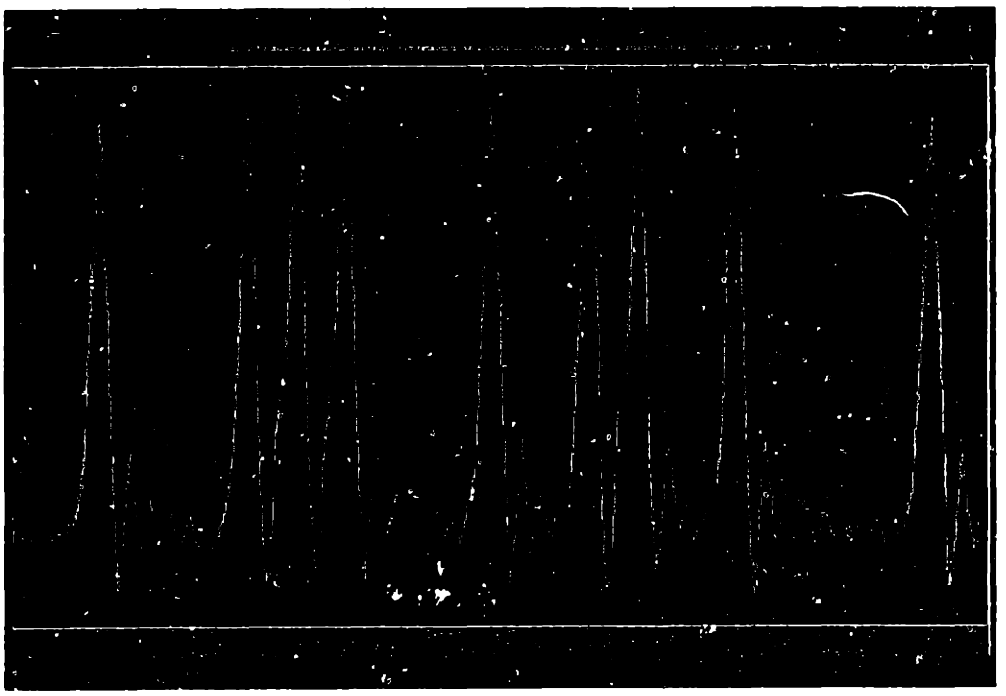

Figure 3-16: Portion of the $2^{31} - 1$ pseudorandom bit pattern as obtained on the digital sampling scope. Deleterious effects such as data pattern dependency as well as detector ringing are clearly evident.

Chapter 4

The Dispersion-Imbalanced Nonlinear Optical Mirror (DILM)

The nonlinear optical loop mirror (NOLM) was invented by Doran and Wood in 1988 [30]. It is a fiber loop constructed with an asymmetric coupler (Fig. 4-1), so that when light enters the NOLM, it is split into two pulses of unequal intensities, which will then acquire different nonlinear phase shifts as they propagate along the fiber. When these two pulses interfere at the coupler, the non-reciprocal phase difference alters the transmissivity of the NOLM in an intensity-dependent fashion. In 1990, Fermann *et al.* enhanced the design of nonlinear loop mirrors by placing an optical amplifier asymmetrically in the loop (Fig. 4-2), which was known as a nonlinear amplifying loop mirror (NALM) [31]. The presence of an active element in his design lowers the switching energy substantially. Subsequently, Richardson *et al.* [32] and Duling [33] used the NALM as an artificial saturable absorber to build short-pulse figure-of-eight fiber lasers. Others used the NOLM and the NALM to perform all-optical switching [34] and logic functions [35].

In this chapter, the concept of imbalancing loop mirrors with dispersion is first addressed, with emphasis on the how the self-switching behavior changes as a function of input pulse intensity, pulse width, and fiber length. The experimental results showing cw and ASE suppressions are then discussed, and compared with numerical results.

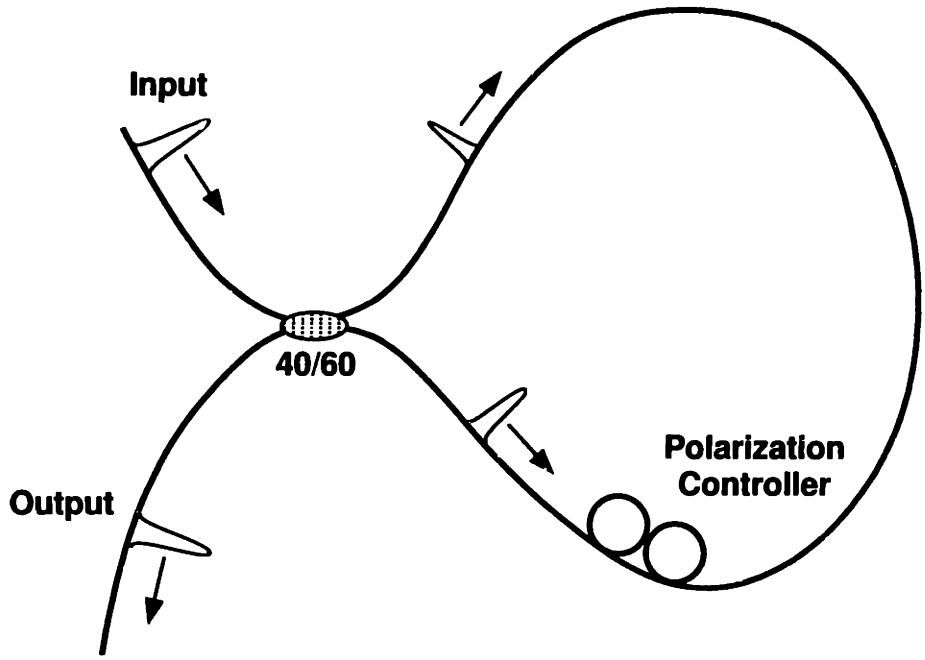

Figure 4-1: The nonlinear optical loop mirror.

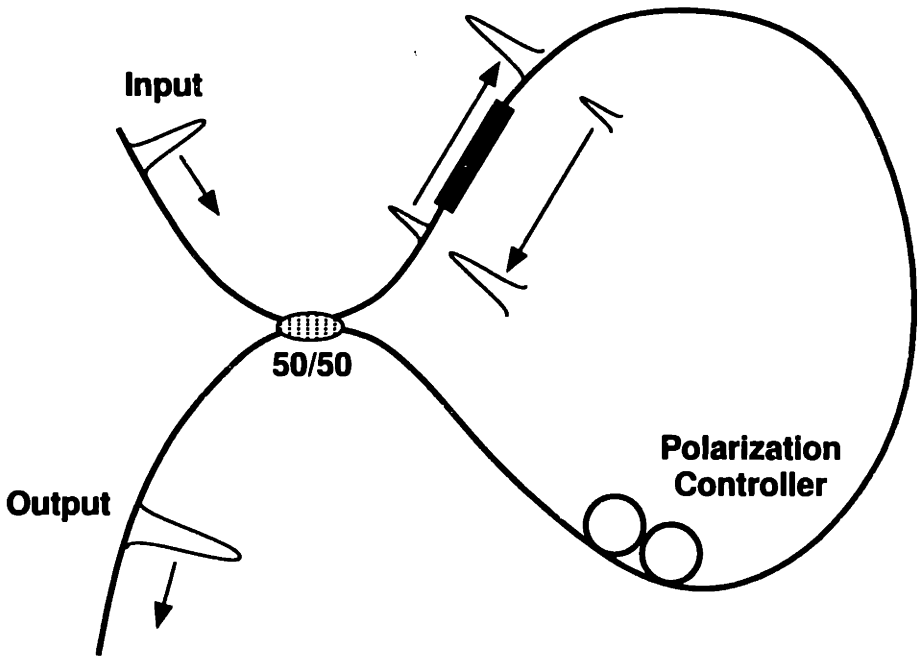

Figure 4-2: The nonlinear amplifying loop mirror.

4.1 Concept of a Dispersion-imbalanced Switch

Recently, the possibility of imbalancing a loop mirror with dispersion was demonstrated [9]. The dispersion-imbalanced loop was constructed with a 50/50 coupler, a segment of dispersive fiber, and a segment of dispersionless fiber (Fig. 4-3). When an $N < 1$ optical pulse enters the loop mirror, the clockwise-traveling pulse disperses quickly in the dispersive segment and then remains broad in the dispersionless segment; on the other hand, the counterclockwise-traveling pulse remains short and intense for the entire dispersionless first segment, where it acquires a large amount of nonlinear phase shift that is proportional to its peak intensity and to the fiber length L_2 (Fig. 4-4).

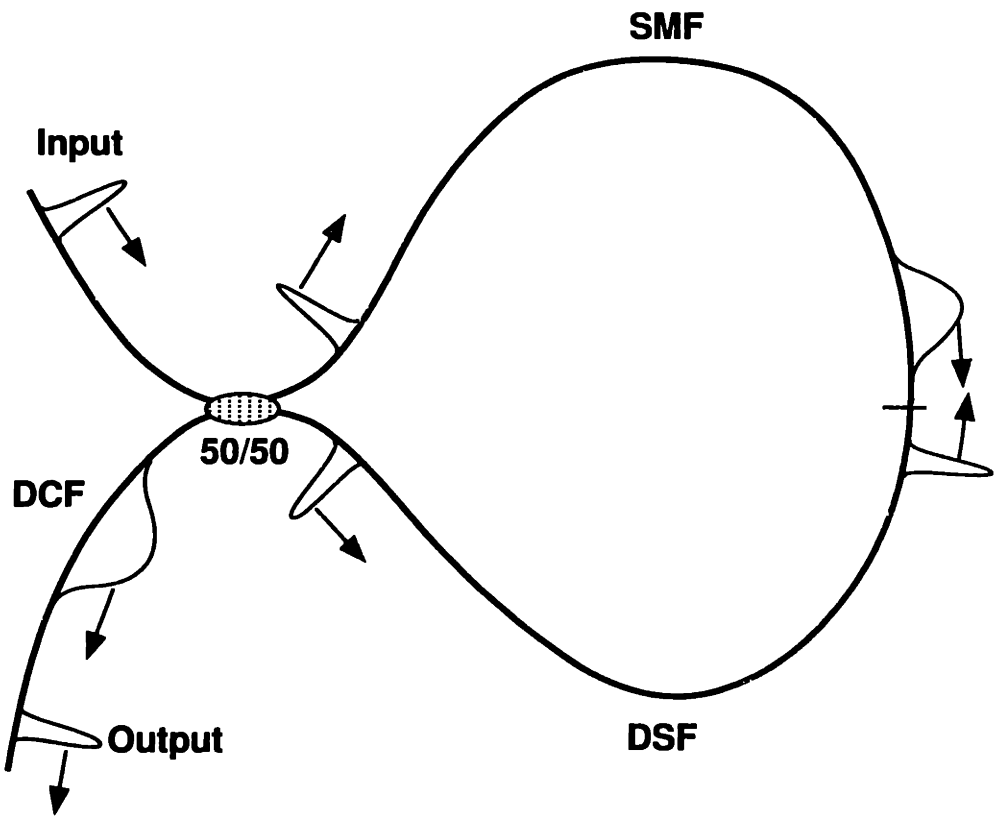

Figure 4-3: Conceptual operation of a dispersion-imbalanced loop mirror showing pulse stretching and compression: SMF, single-mode fiber; DCF, dispersion-compensating fiber; DSF, dispersion-shifted fiber.

Pulse propagation in an optical fiber can be modeled by the nonlinear Schrödinger

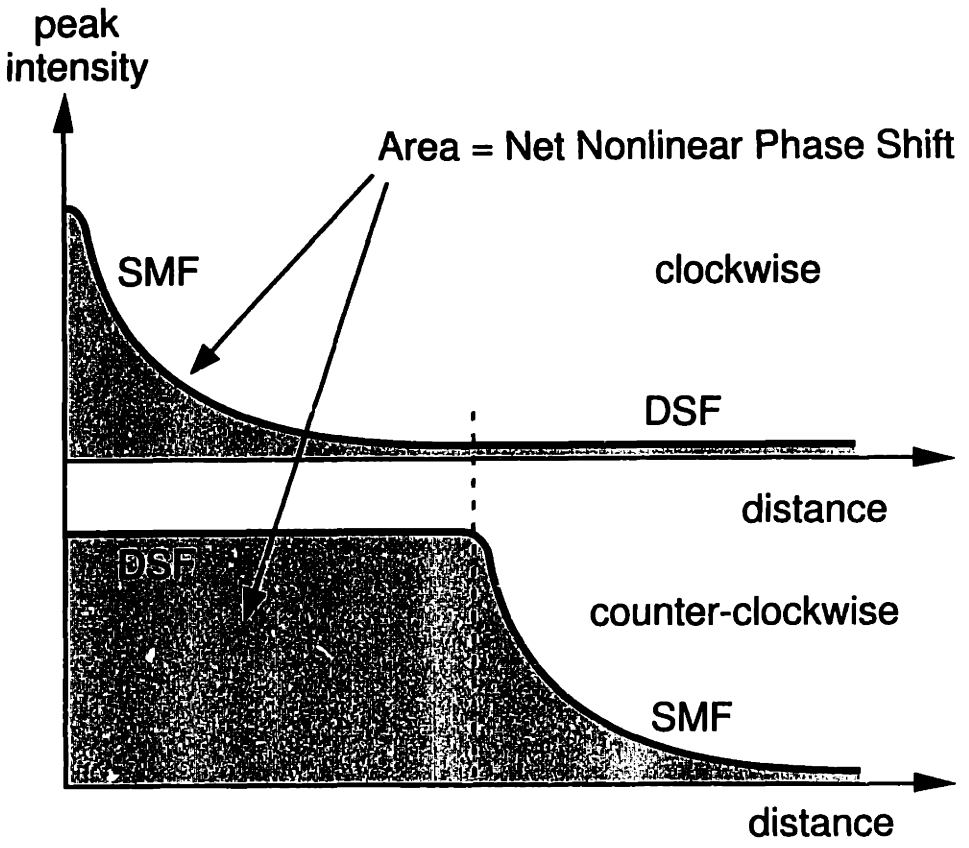

Figure 4-4: Plots of the peak pulse intensity as a function of distance along the two propagation directions: clockwise and counterclockwise.

equation, which in dimensionless form is

$$j\frac{\partial u}{\partial z} = \frac{1}{2}D_i\frac{\partial^2 u}{\partial t^2} + |u|^2 u. \tag{4.1}$$

The normalized distance z is in units of the dispersion length $z_c = \tau^2/|\beta_2|$, $\tau \approx 0.567\tau_{\mathrm{FWHM}}$, the normalized time t is measured in units of τ, the complex electric field envelop $u = u(z,t)$ is in units of $1/\sqrt{\delta z_c}$, where $\delta = 2\pi n_2/\lambda_0 A_{\mathrm{eff}}$, A_{eff} is the modal effective area in the fiber, $\beta_2 = \partial^2\beta/\partial\omega^2$, and n_2 is the nonlinear index $\approx 3.18\times10^{-20}$ m^2/W. Since dispersion varies along the loop, the normalization is done at the fiber segment with the largest amount of dispersion, i.e., $D_1 = 1$ and $|D_2| < |D_1|$. We assume that the input pulse has a hyperbolic secant shape $u(0,t) = N\mathrm{sech}(t)$ and the input fiber has a dispersion of $D_{\mathrm{input}} = D_1$. For example, an $N = 1$ soliton incident at the 50/50 coupler will split into an $N = 1/\sqrt{2}$ soliton propagating along L_1 in the clockwise direction, and an $N = 1/(D_2\sqrt{2})$ soliton propagating along L_2 in the counterclockwise direction.

The evolution of an $N = 0.85$ soliton input pulse as a function of distance is simulated numerically with a split-step Fourier algorithm with 1024 temporal gridpoints (Fig. 4-5). The loop parameters are $D_1 = 1.0$, $D_2 = 0.1$, and $L_1 = L_2 = 5.8z_0$, where $z_0 = z_c\pi/2$ is the soliton period. After the 50/50 coupler, the output pulse is compressed in the DCF to yield a near transform-limited pulse. The DCF parameters are $D_3 = D_{DCF} = -4.0$ and $L_3 = L_{DCF} = 1.45z_0$.

4.2 Switching Characteristics

Since fiber dispersion acts on pulses but not on cw light, a nonlinear loop mirror that is imbalanced by dispersion is not only able to select pulse amplitude as well as pulse width, but also to reject cw and ASE noise present in the input. Motivated by this observation, we investigate the switching characteristics of dispersion-imbalanced loop mirrors as a function of input pulse intensity, pulse width, and fiber length.

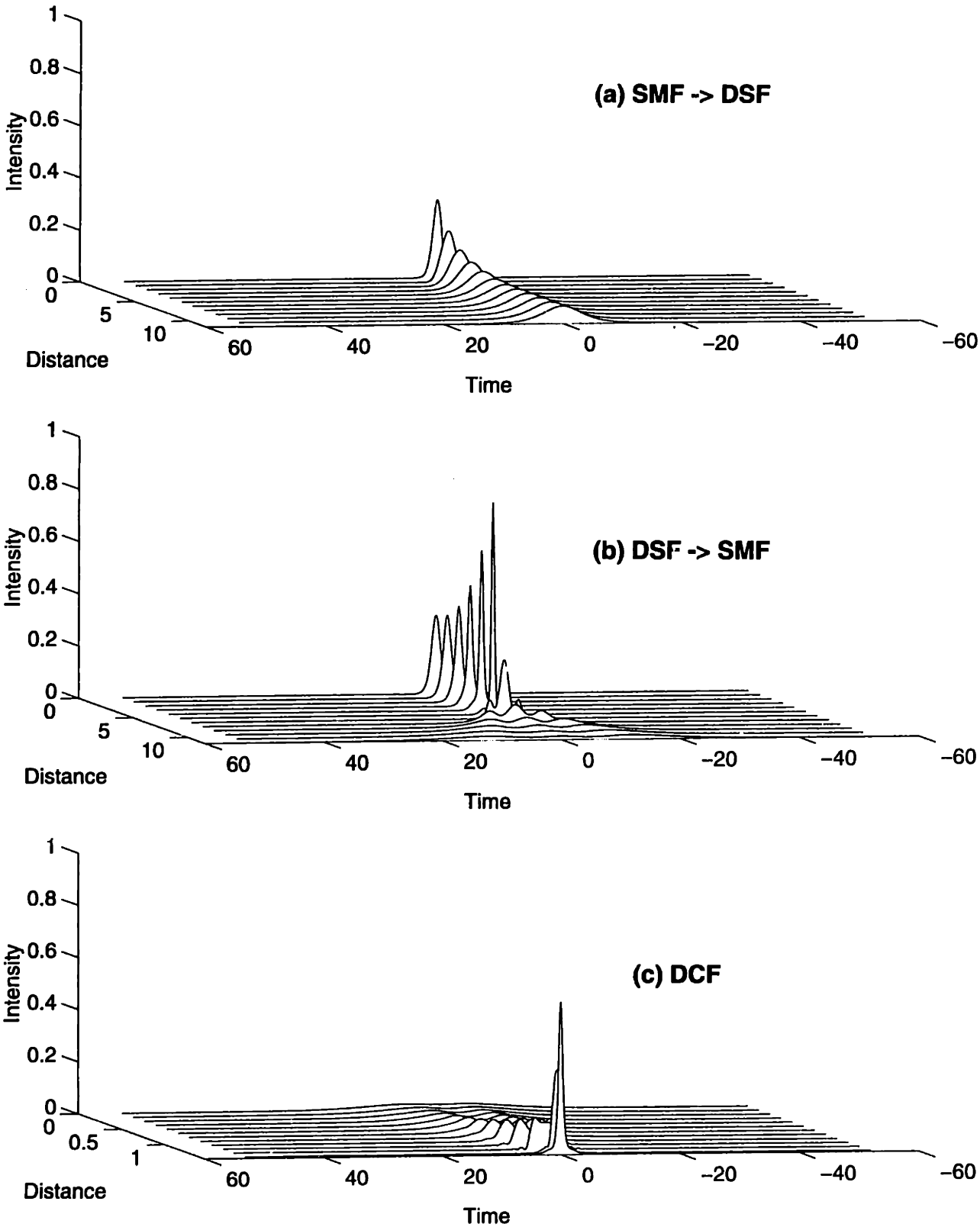

Figure 4-5: Intraloop pulse evolution: (a) clockwise along SMF and then DSF, (b) counterclockwise along DSF and then SMF, (c) along the output DCF.

4.2.1 Switching Characteristics as a Function of Input Intensity

Figure 4-6 shows the temporal output pulse intensities as the input pulse energy $2N^2$ is increased. The transmissivity first increases, peaks, and then drops to a minimum when the nonlinear phase shift is about 2π. Although this type of response is typical among conventional nonlinear loop mirrors, the response of the dispersion-imbalanced loop mirror is pulse-width sensitive as well, which will be shown in the next section.

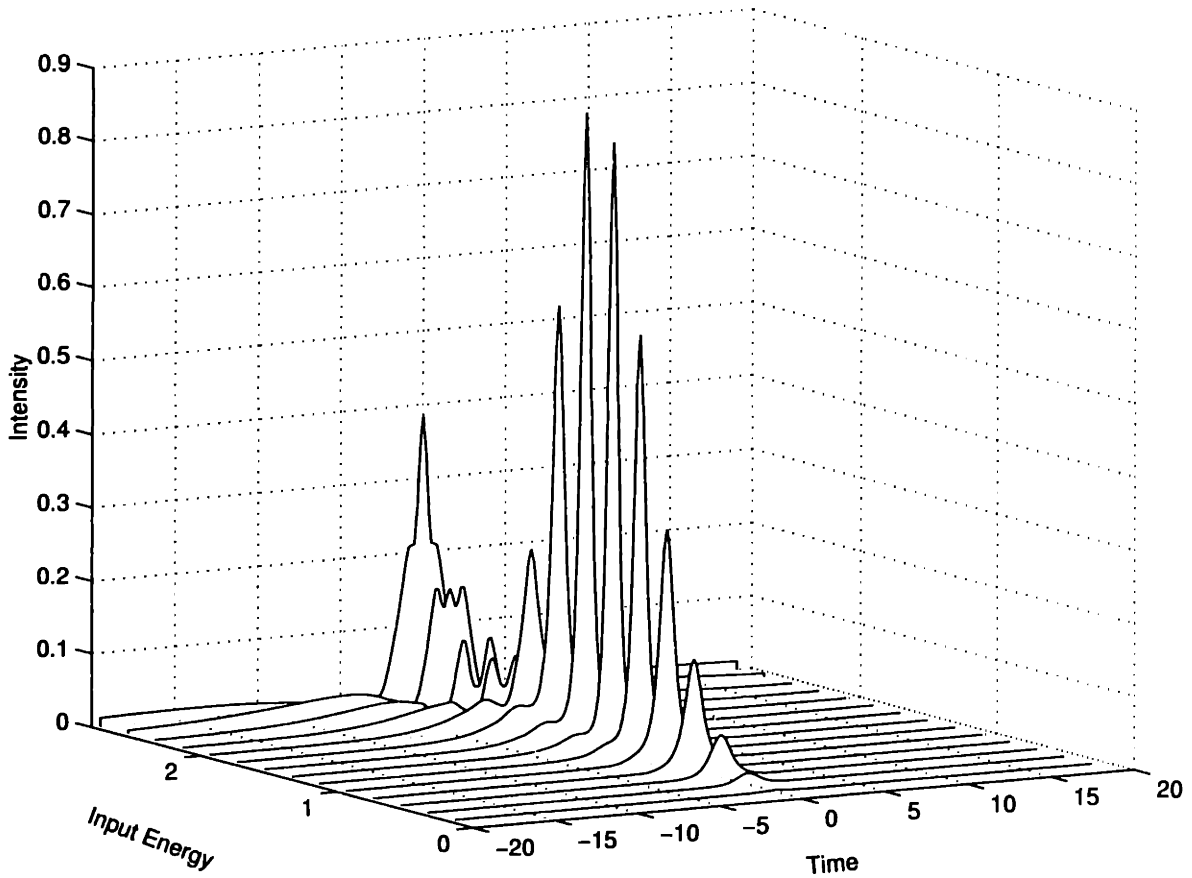

Figure 4-6: Temporal output pulse shapes as a function of input energy. The loop parameters are $D_1 = 1.0$, $D_2 = 0.1$, and $L_1 = L_2 = 5.8z_0$. The DCF parameters are $D_3 = D_{DCF} = -4.0$ and $L_3 = L_{DCF} = 1.45z_0$.

4.2.2 Switching Characteristics as a Function of Input Pulse Width

The dependence of switching as a function of pulse width is investigated by varying the normalized pulse width τ in the initial condition $u(0,t) = 0.85\text{sech}(t/\tau)$. The dependence of switching on pulse width is clearly seen in Fig. 4-7. For example, a factor of two change in pulse width from unity results in about a factor of two change in transmissivity.

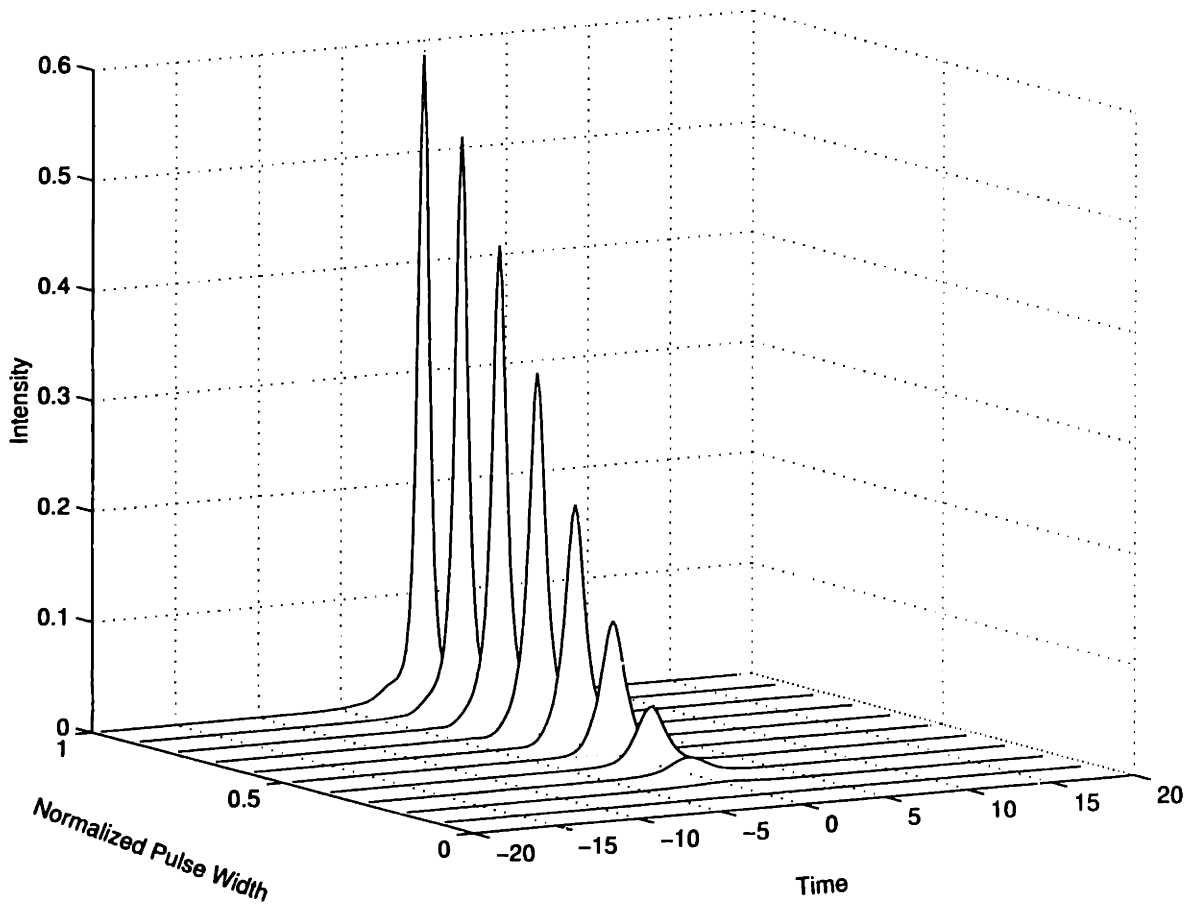

Figure 4-7: Temporal output pulse shapes as a function of normalized pulse width τ. The loop parameters are $D_1 = 1.0$, $D_2 = 0.1$, and $L_1 = L_2 = 5.8z_0$. The DCF parameters are $D_3 = D_{DCF} = -4.0$ and $L_3 = L_{DCF} = 1.45z_0$.

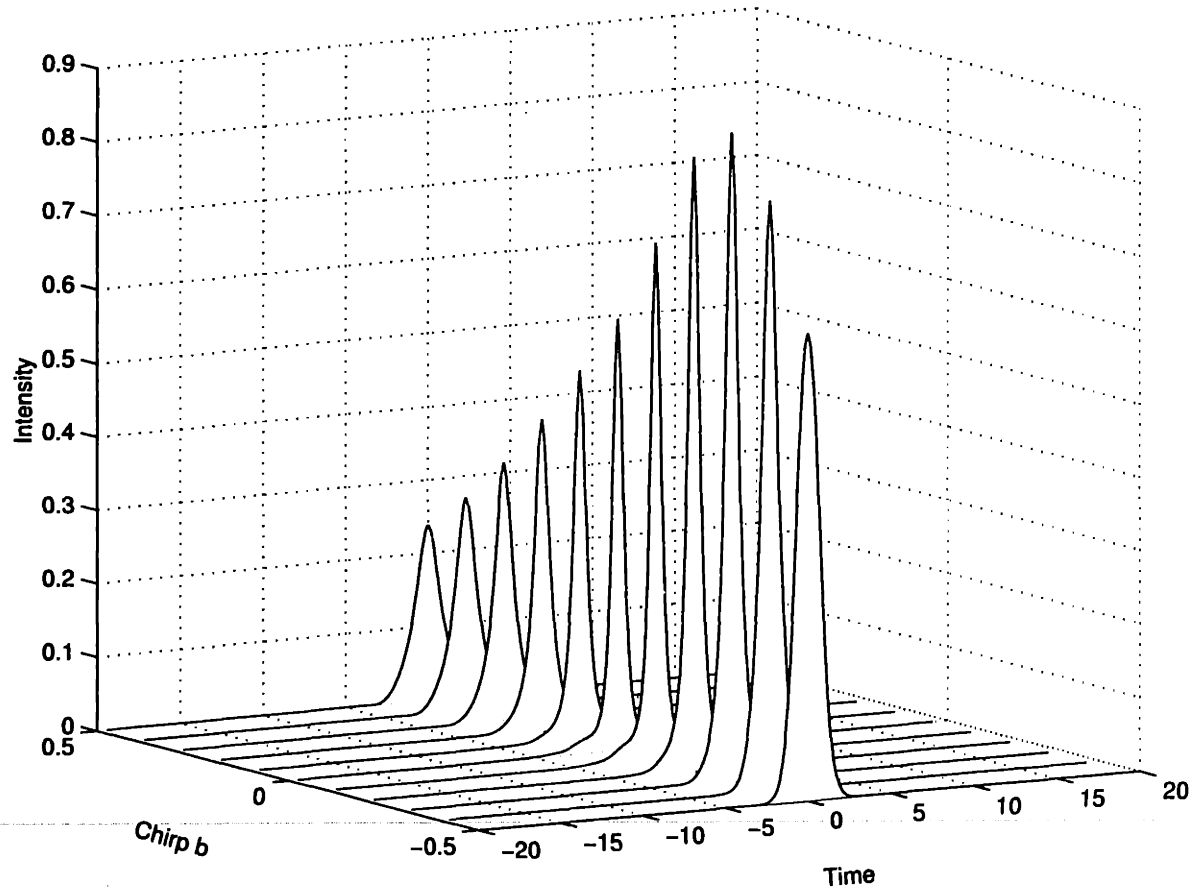

Figure 4-8: Temporal output pulse shapes as a function of linear chirp parameter b. The loop parameters are $D_1 = 1.0$, $D_2 = 0.1$, and $L_1 = L_2 = 5.8z_0$. The DCF parameters are $D_3 = D_{DCF} = -4.0$ and $L_3 = L_{DCF} = 1.45z_0$.

4.2.3 Switching Characteristics as a Function of Fiber Length

As the length of the DSF L_2 gets longer, the transmissivity peak shifts to lower energies, which can be explained by the fact that, to first order, the nonlinear phase shifts acquired by the two pulses are approximately:

$$\phi_{\text{NL, CW}} \approx 0 \tag{4.2}$$

$$\phi_{\text{NL, CCW}} \approx \frac{N^2}{2}\text{sech}^2(t)L_2 \, . \tag{4.3}$$

Since self-switching is an interferometric effect, one expects near-complete switching to occur when

$$\left|\phi_{\text{NL, CW}} - \phi_{\text{NL, CCW}}\right| \approx \pi \, . \tag{4.4}$$

In other words, the first peak in transmissivity occurs at

$$N^2 = \frac{2\pi}{L_2} \, . \tag{4.5}$$

If one expresses L_2 in units of the soliton period z_0, then Eq. (4.5) becomes

$$\text{Input pulse energy } 2N^2 = 8/L_2 \, . \tag{4.6}$$

Equation (4.4) is plotted as circles in Fig. 4-9 where L_2 is expressed in units of z_0. Good agreement is found between this back-of-the-envelope approximation and the full numerics. Its simplicity serves as a quick method to estimate the length of fiber needed for switching for a certain given input pulse. In contrast, running the full simulations to generate the curves for Fig. 4-9 can take many hours on a typical UNIX workstation.

4.3 Modeling via the Variational Approximation

The nonlinear Schrödinger (NLS) equation describes nonlinear pulse propagation in an optical fiber, where the effects of second-order group-velocity dispersion and the

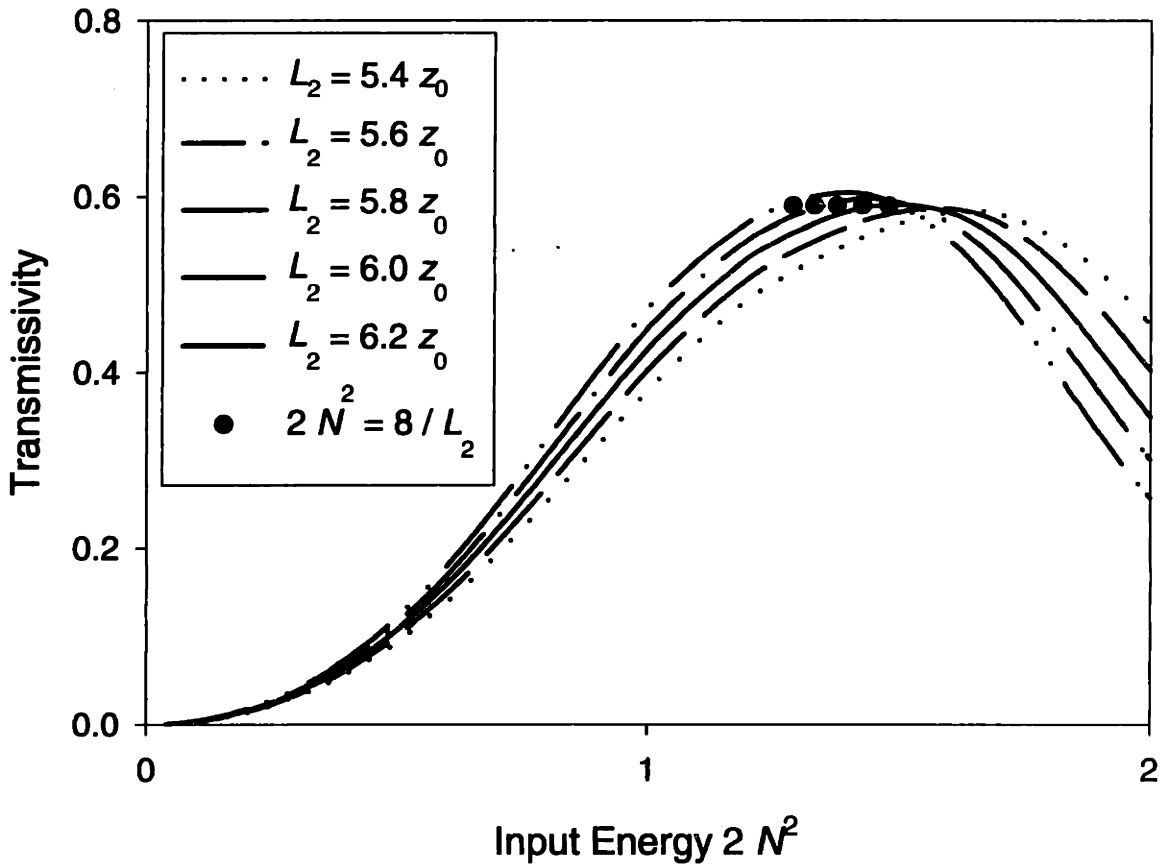

Figure 4-9: Transmissivity vs. input energy for different fiber lengths. Dotted, $L_2 = 5.4z_0$; short dash, $L_2 = 5.6z_0$; dash-dot, $L_2 = 5.8z_0$; dash-dot-dash, $L_2 = 6.0z_0$; solid, $L_2 = 6.2z_0$; circle, peak location as predicted by $2N^2 = 8/L_2$ in Eq. (4.6). The loop parameters are $D_1 = 1.0$, $D_2 = 0.1$, and $L_1 = 5.8z_0$. The DCF parameters are $D_3 = D_{DCF} = -4.0$ and $L_3 = L_{DCF} = 1.45z_0$.

Kerr nonlinearity are modeled. There exists a large body of theoretical and experimental work that was devoted to studying the properties of the NLS equation, along with its variants. Despite the fact that, in very few limited cases, exact results can be obtained using inverse scattering theory [12] to yield fundamental and higher order soliton solutions, approximate methods are needed to solve the remaining non-integrable problems. Anderson *et al.* first studied the variational formulation of the NLS equation by using linearly chirped Gaussians [36] and linearly chirped hyperbolic secants [37] as trial functions. Using the Ritz optimization procedure, the first variation of the variational functional is made to vanish to first order within a set of trial functions. Providing that good trial functions are used, the variational approach can capture the physics behind pulse propagation in an optical fiber. Subsequently, he and others applied the method successfully to study the effects of third-order dispersion [38], fourth-order dispersion [39], and linear birefringence [40], and phenomena such as soliton collisions [41] and dark solitons [42].

4.3.1 Variational Formulation of the Nonlinear Schrödinger Equation

The NLS equation can be written as

$$j\frac{\partial u}{\partial x} = D\frac{\partial^2 u}{\partial t^2} + \delta\left|u\right|^2 u, \tag{4.7}$$

where

$$D = -\frac{k''}{2} = -\frac{1}{2}\frac{\partial^2 k}{\partial \omega^2}, \tag{4.8}$$

$$\delta = \frac{2\pi n_2 \hbar \omega_0}{\lambda_0 A_{\text{eff}}}, \tag{4.9}$$

$u(x,t)$ is the complex slowly varying envelope of the optical field, A_{eff} is the modal effective area in the fiber, $\hbar (= 1.05 \times 10^{-34}$ J·s) is Planck's constant divided by 2π, ω_0 is the soliton initial carrier (mean) frequency (rad/s), and for silica the nonlinear index $n_2 \approx 3.2 \times 10^{-20}$ m^2/W.

It is straight forward to show that, if the Lagrangian is given by

$$L = \frac{j}{2}\left(u\frac{\partial u^*}{\partial x} - u^*\frac{\partial u}{\partial x}\right) - D\frac{\partial u}{\partial t}\frac{\partial u^*}{\partial t} + \frac{\delta}{2}|u|^4, \tag{4.10}$$

the variational formulation

$$\delta \int\int L\,dx\,dt = 0 \tag{4.11}$$

leads to the starting equation (4.7) via the Euler-Lagrange equation

$$\frac{\delta L}{\delta u^*} = \frac{d}{dt}\left(\frac{\partial L}{\partial u_t^*}\right) + \frac{d}{dx}\left(\frac{\partial L}{\partial u_x^*}\right) - \frac{\partial L}{\partial u^*} = 0. \tag{4.12}$$

4.3.2 Equations of Motion for the Pulse Parameters

In Ref. [36], Anderson used a linearly chirped Gaussian

$$u(x,t) = A(x)\exp\left[-\frac{t^2}{2a(x)^2} + jb(x)t^2 + j\phi(x)\right] \tag{4.13}$$

as the trial function, where $A(x)$ is the pulse amplitude, $a(x)$ is the pulse width, $b(x)$ is the linear chirp parameter, and $\phi(x)$ is the overall phase of the pulse. Substituting the trial function in Eq. (4.13) into the Lagrangian and integrating with respect to t, one obtains the averaged Lagrangian

$$\begin{aligned}\langle L\rangle &= \int_{-\infty}^{+\infty} L\,dt \\ &= \frac{2}{3}\delta a A^2 - \frac{2D}{3}\frac{A^2}{a}\left(1+\beta^2\right) + A^2\beta\frac{da}{dx} \\ &\quad + \left(2\ln 2 - 2\right)A^2 a\frac{d\beta}{dx} \\ &\quad + 2A^2 a\frac{d\phi}{dx}.\end{aligned} \tag{4.14}$$

The equations of motion for the pulse parameters are computed from the reduced Lagrangian as:

$$\frac{dA}{dx} = 2DAb \tag{4.15}$$

$$\frac{da}{dx} = -4Dab \tag{4.16}$$

$$\frac{db}{dx} = 4Db^2 - \frac{D}{a^4} + \frac{\delta}{2\sqrt{2}}\frac{A^2}{a^2} \tag{4.17}$$

$$\frac{d\phi}{dx} = \frac{D}{a^2} - \frac{5\sqrt{2}}{8}\delta A^2. \tag{4.18}$$

The equation of motion for the pulse width $a(x)$ has the following physical interpretation: the presence of linear chirp $b(x)$ can cause the pulse width to increase or decrease, depending on the sign of the dispersion (normal or anomalous) and the sign of the chirp. In addition, the rate of pulse broadening or shortening, $\frac{da}{dx}$, increases with inverse pulse width. The equation of motion of the chirp parameter $b(x)$ tells us that both nonlinearity (first term) and dispersion (second term) can cause a pulse to be chirped.

In Ref. [37], Anderson *et al.* also tried using a linearly chirped sech

$$u(x,t) = A(x)\text{sech}\left[\frac{t}{a(x)}\right]\exp\left[jb(x)t^2 + j\phi(x)\right] \tag{4.19}$$

as the trial function. Similarly, the equations of motion for the pulse parameters can be computed from the reduced Lagrangian as:

$$\frac{dA}{dx} = -\frac{A}{2a}\frac{da}{dx} \tag{4.20}$$

$$\frac{d^2a}{dx^2} = \frac{16D^2}{\pi^2 a^3} - \frac{8D}{\pi^2}\frac{\delta A^2}{a^2} \tag{4.21}$$

$$b = \frac{1}{4Da}\frac{da}{dx} \tag{4.22}$$

$$\frac{d\phi}{dx} = -\frac{2D}{3a^2} + \frac{5}{6}\delta A^2. \tag{4.23}$$

In the soliton regime where $D > 0$, we see that Eqs.(4.20)–(4.23) has the following steady-state solution:

$$A_{00} = \frac{1}{a_{00}}\sqrt{\frac{2D}{\delta}} \tag{4.24}$$

$$b_{00} = 0 \tag{4.25}$$

$$\frac{d\phi_{00}}{dx} = -\frac{D}{a_{00}^2} \tag{4.26}$$

or

$$u(x,t) = \frac{1}{a_{00}}\sqrt{\frac{2D}{\delta}}\text{sech}\left(\frac{t}{a_{00}}\right)e^{-j\frac{D}{2a_{00}^2}}, \tag{4.27}$$

which is exactly the $N = 1$ fundamental soliton solution [43]:

$$u(x,t) = \text{sech}(t)e^{-jx/2}, \tag{4.28}$$

if one uses the normalization $D = 1/2$, $\delta = 1$, and $a_{00} = 1$.

Using the variational method with the hyperbolic-secant trial function to approximate intra-loop pulse propagation, one obtains reasonable good agreement between this method and the full numerics (Figs. 4-10 and 4-11). As expected, the variational solution fails to describe the small pedestal in the output pulse, which accounts for 4% of the energy of the pulse. In other words, the pulse energy of the variational solution is 4% less than that of the full numerics. Please note that the overall system is still Hamiltonian — the *total energy* of the transmitted and the reflected pulses is conserved assuming that the fiber is lossless.

4.4 Experiment

The experimental setup is shown in Fig. 4-12. A 980 nm diode-pumped soliton laser and a DFB laser emitting 1.4 mW at 1550 nm are both amplified by a bi-directionally pumped erbium-doped fiber amplifier. The amplified light consists of 400 fs pulses (spectral width = 9 nm) with 0.16 nJ of pulse energy at 18 MHz and 8 mW of cw power at 1550 nm and 1554 nm. The 1554 nm peak is due to cw lasing in the soliton laser. The Sagnac loop is constructed with a 50/50 coupler with 50 cm of dispersion-shifted leads, 10.0 m of Corning SMF28 fiber with an anomalous dispersion of -23 ps^2/km, and 10.0 m of Corning DSF fiber with dispersion of -2.3 ps^2/km. Since N is less than unity after the pulse splits at the 50/50 coupler, we use 2.5 m of dispersion-compensating fiber (dispersion = +94.7 ps^2/km) to compress the 2.7

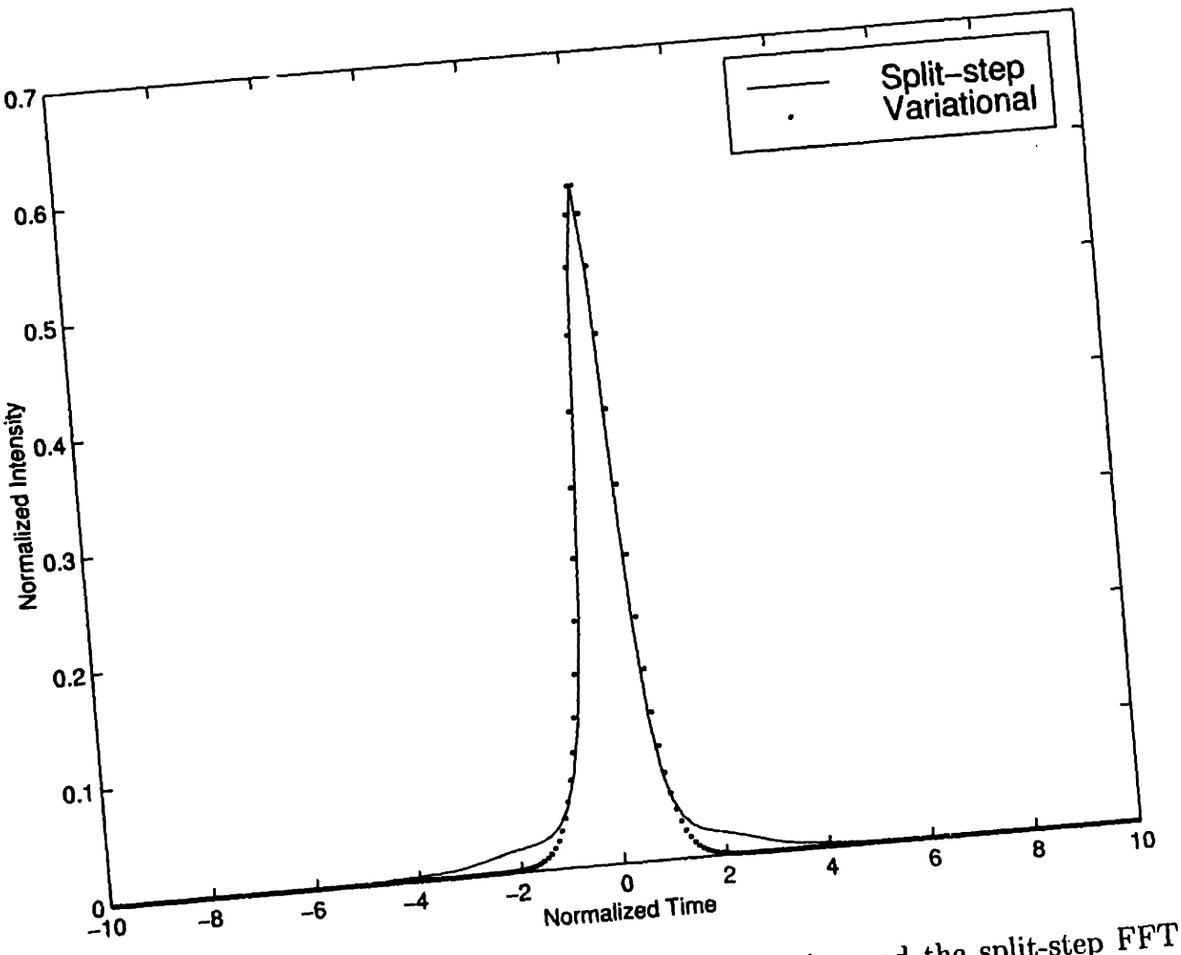

Figure 4-10: Comparison of the variational approximation and the split-step FFT scheme, linear scale. The loop parameters are $D_1 = 1.0$, $D_2 = 0.1$, and $L_1 = 5.8z_0$. The DCF parameters are $D_3 = D_{DCF} = -4.0$ and $L_3 = L_{DCF} = 1.45z_0$.

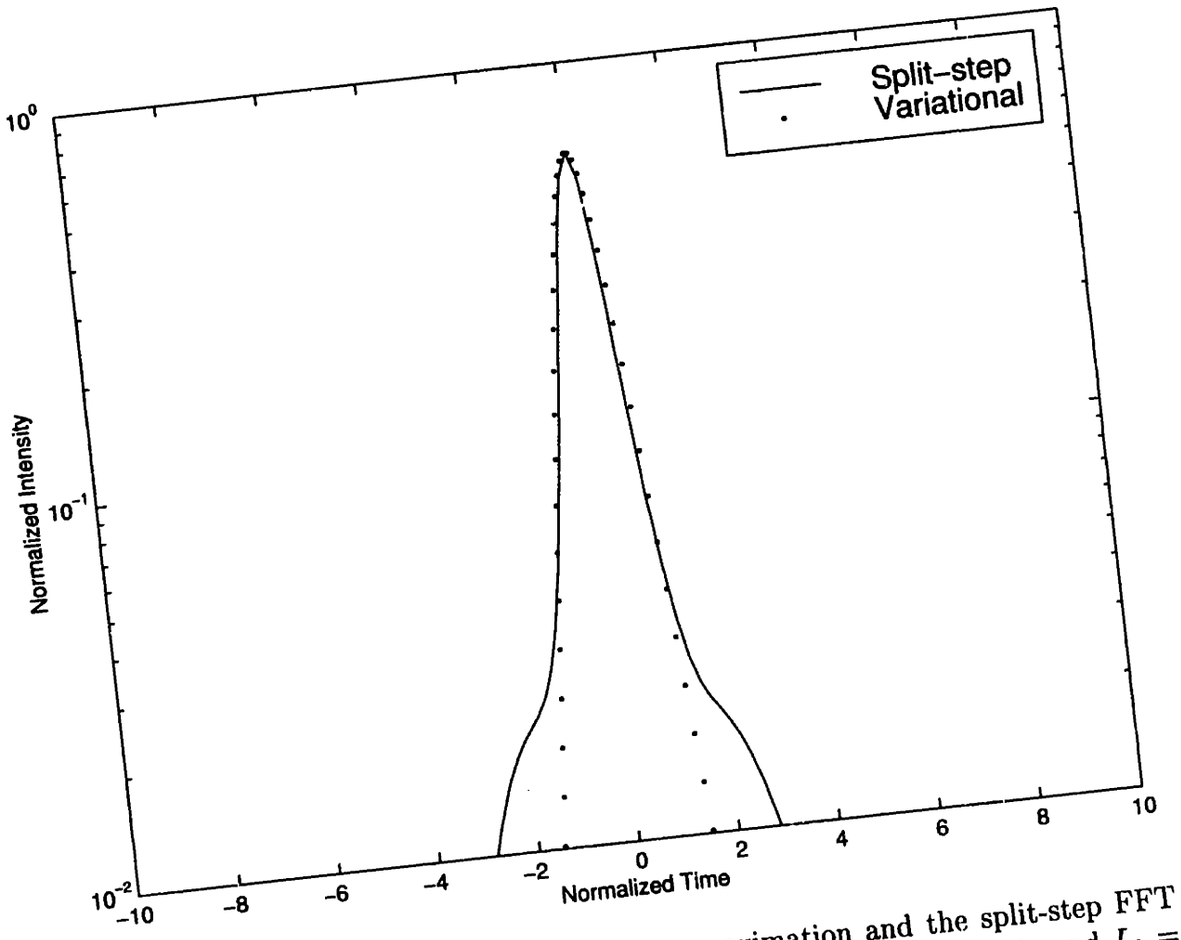

Figure 4-11: Comparison of the variational approximation and the split-step FFT scheme, logarithmic scale. The loop parameters are $D_1 = 1.0$, $D_2 = 0.1$, and $L_1 = 5.8z_0$. The DCF parameters are $D_3 = D_{DCF} = -4.0$ and $L_3 = L_{DCF} = 1.45z_0$.

ps chirped output pulse. The use of a three-port optical circulator makes simultaneous monitoring of transmitted and reflected light possible. To cancel the natural birefringence of the fibers, the transmissivity of the loop is nulled by adjusting the polarization controller for low-intensity cw input. The transmissivity characteristics are measured for both pulsed input and cw input (Fig. 4-13). The switching energy at the first peak is 93 pJ for 30% transmissivity for pulsed input. Since there is good agreement between the experimental data and simulations (when coupling and connector losses are accounted for), we expect the output pulse shape to be close to what is depicted in Fig. 4-6.

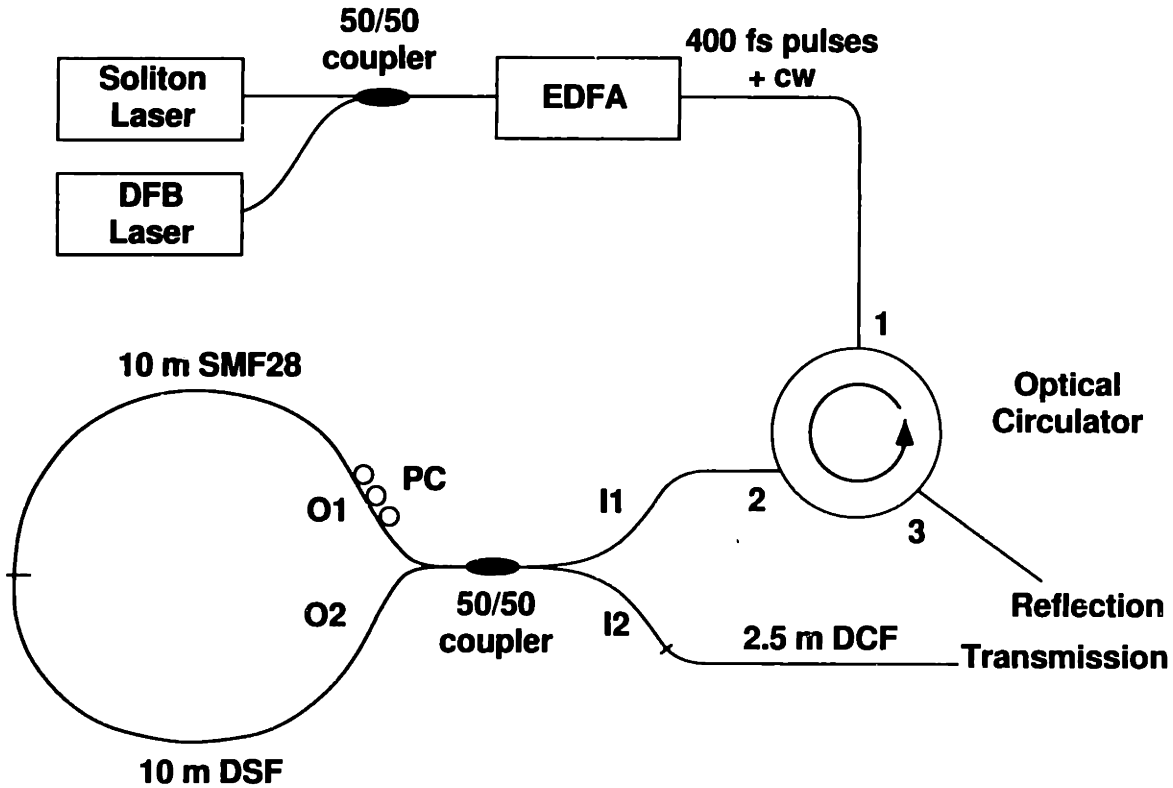

Figure 4-12: Experimental setup: PC, polarization controller; EDFA, erbium-doped fiber amplifier. The experimental parameters, stated in normalized units, are $D_1 = 1.0$, $D_2 = 0.1$, $D_3 = -4.0$, $L_1 = L_2 = 5.8z_0$, and $L_3 = 1.45z_0$.

The input and transmitted optical spectra are shown in Figs. 4-14 and 4-15 respectively. The extinction (loss) for cw in the output, relative to that of the pulse output, is 22 dB. Moreover, the pulse spectrum is modified in a favorable way — the spectral width broadens from 9 nm to 14 nm, while the resonant solitonic sidebands are re-

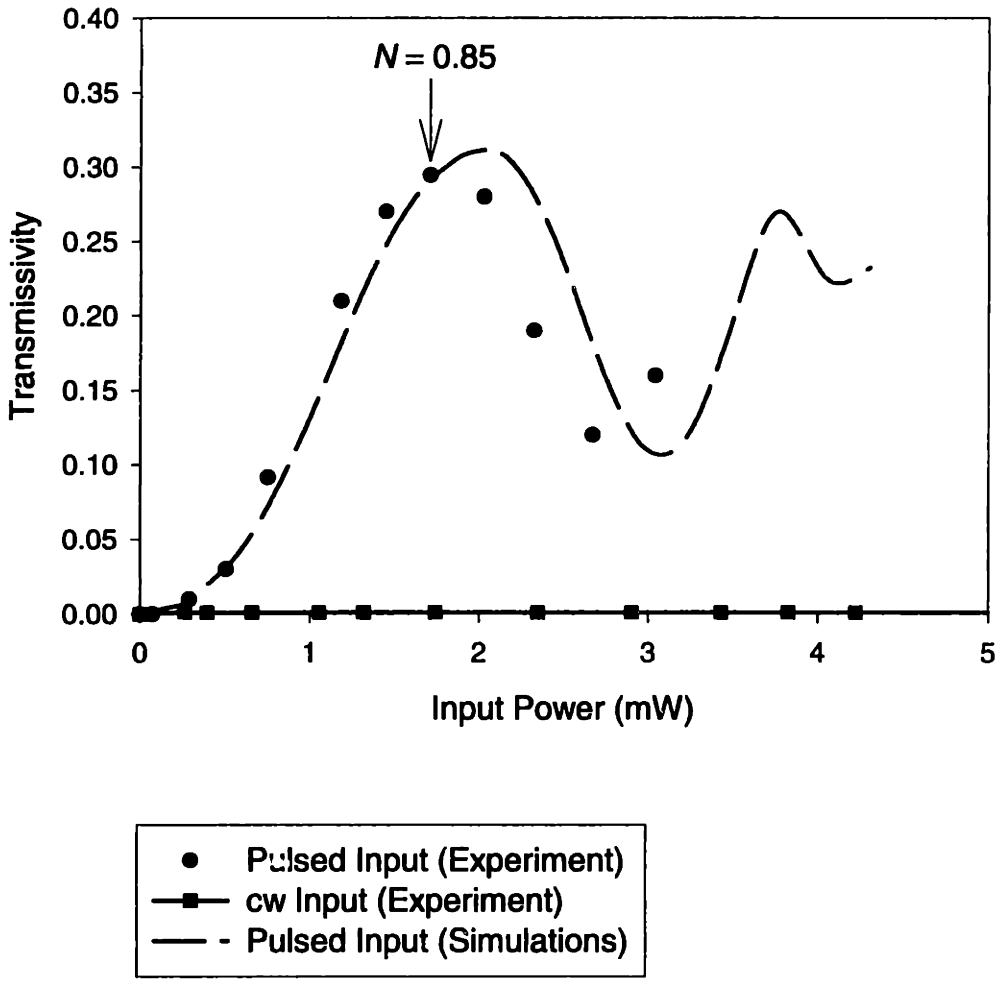

Figure 4-13: Nonlinear switching characteristics of the dispersion-imbalanced loop mirror.

jected by the loop, resulting in a shorter and cleaner pulse after propagation in a DCF fiber. The broadening in the output spectrum is predicted by simulations as well. As shown in Figs. 4-16 and 4-17, the output FWHM pulse width is compressed to 230 fs after 2.5 m of DCF, assuming a sech shape (time-bandwidth-product = 0.40). The suppression of the pedestal due to cw is evident in the log plot of the pulse autocorrelations before and after the loop. In the future, polarization-maintaining couplers and fibers can be used in constructing the Sagnac loop to improve the stability of its operation, while rendering the use of the polarization controller obsolete.

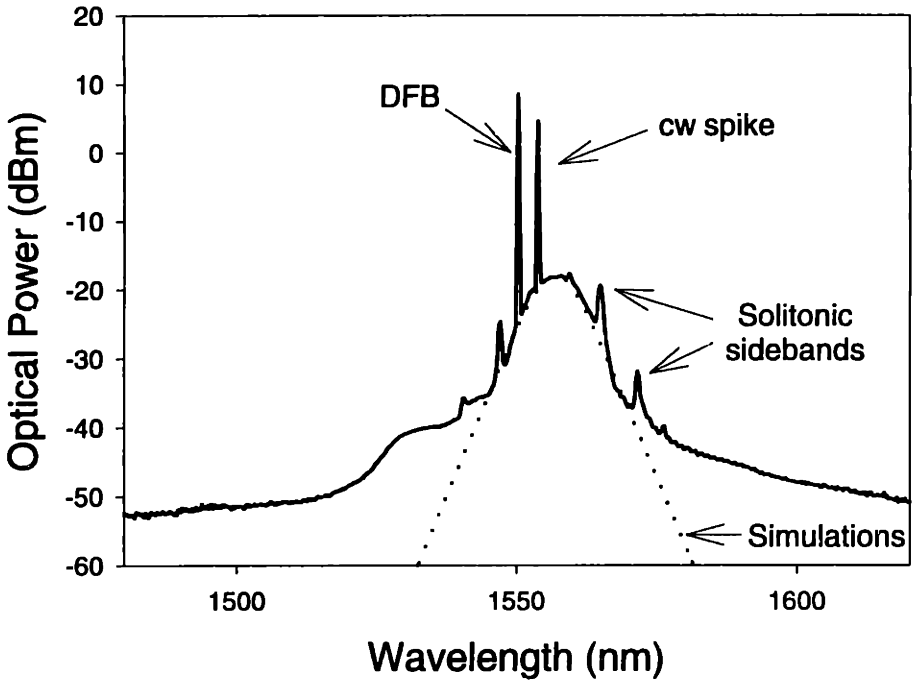

Figure 4-14: Input optical spectrum at port I1. Solid, experiment; dotted, simulations.

4.5 Further Work done by Other Research Groups

4.5.1 Applications in Laser Diode Pulse Compression

I. Y. Khrushchev and colleagues at the University of Bristol, United Kingdom [5], achieved high-quality femtosecond pulse generation from a directly-modulated laser

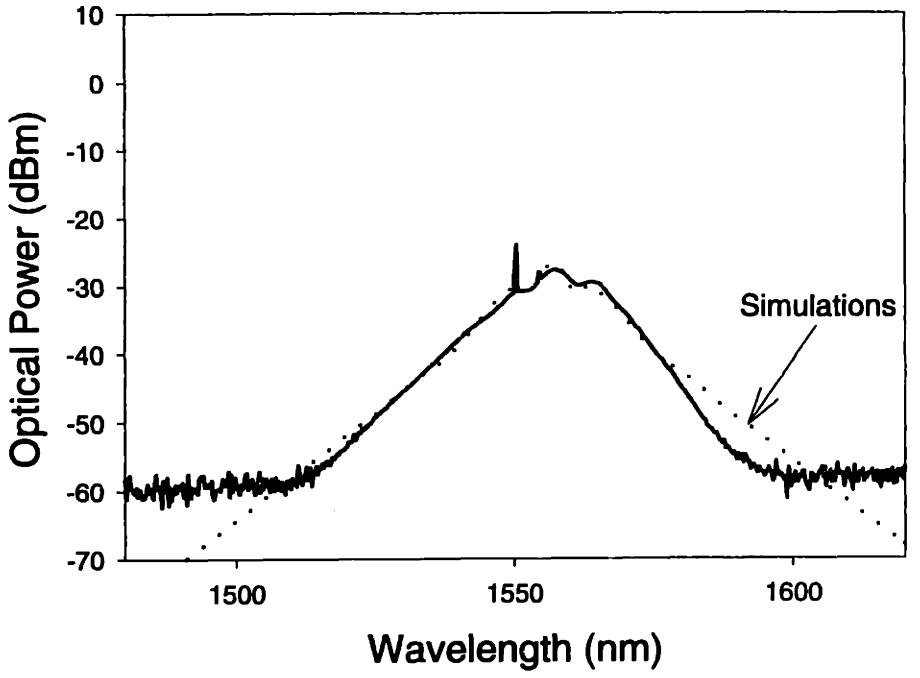

Figure 4-15: Output optical spectrum at port I2. Solid, experiment; dotted, simulations.

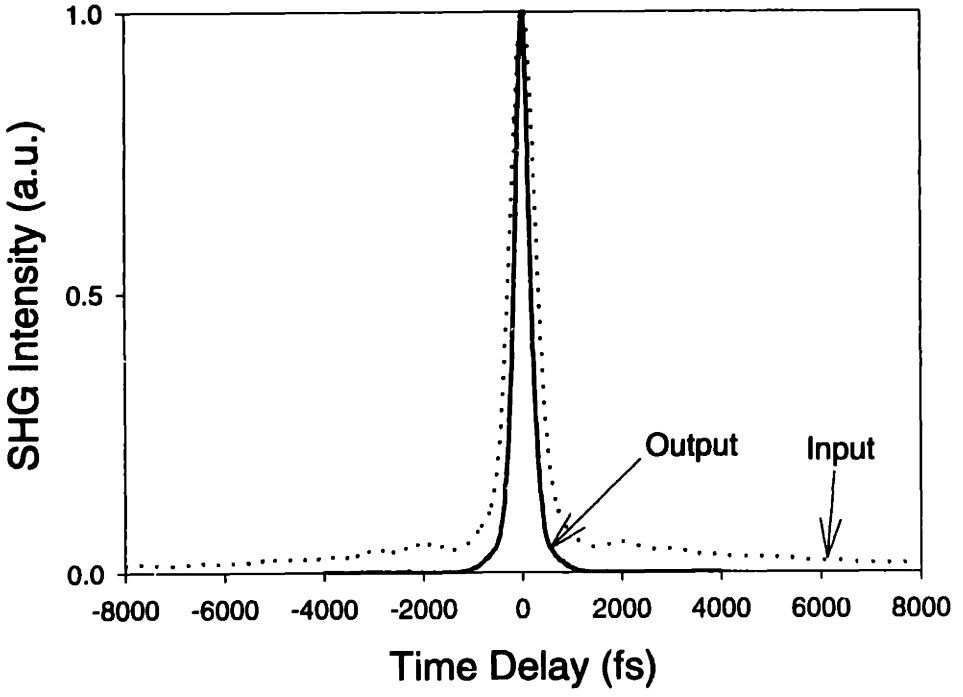

Figure 4-16: Autocorrelation traces of the input pulse (τ_{FWHM} = 400 fs, dotted line) and the transmitted pulse (τ_{FWHM} = 230 fs, solid line). Linear scale.

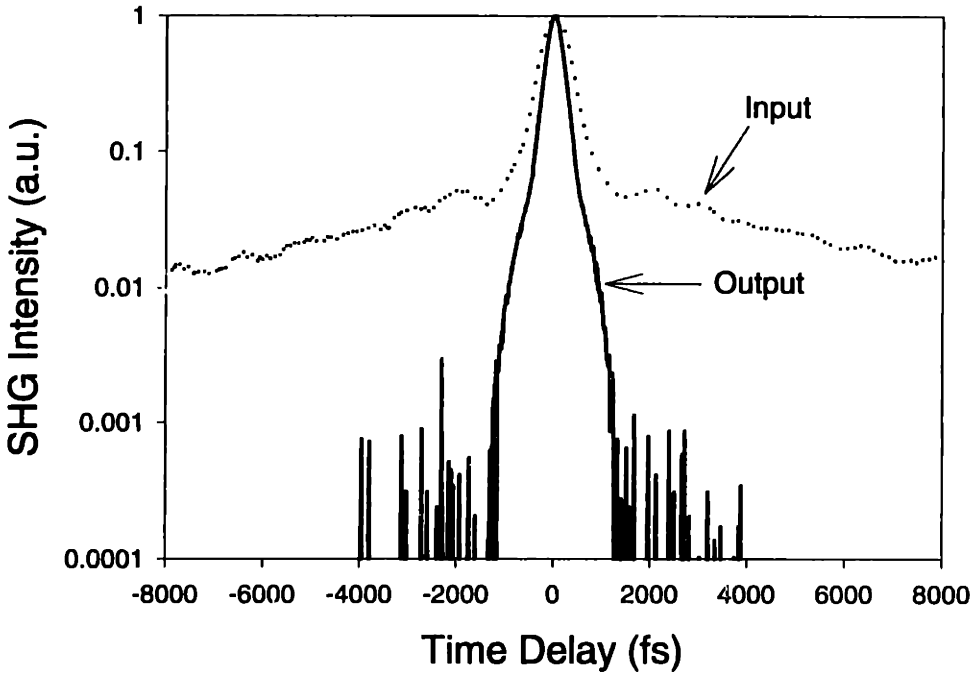

Figure 4-17: Autocorrelation traces of the input pulse (τ_{FWHM} = 400 fs, dotted line) and the transmitted pulse (τ_{FWHM} = 230 fs, solid line). Logarithmic scale.

diode by means of pulse compression in a nonlinear fiber, followed by nonlinear pulse cleanup in a DILM (Figs. 4-18 and 4-19). Starting with 22 ps pulses at a repetition rate of 250 MHz from a multiple quantum well InGaAsP/InP DFB laser diode, they obtained 270 fs compressed pulses with negligible pedestals at the output of the DILM. Their design is very similar to the MIT design. Instead of using two pieces of ten-meter fiber segments, they use 15 m fiber segments. Since we know that by lengthening the DSF segment, the peak of the switching curve will simply shift to lower input power/energies.

Recently, they repeated the above experiment at a much higher repetition rate of 10 GHz [6]. Moreover, they converted the resulting femtosecond pulse train into multiwavelength high-quality picosecond streams by means of spectral-slicing in an arrayed waveguide grating demultiplexer. The advantage of their method lies in the fact that actively mode-locked fiber lasers, an alternative short-pulse WDM source, are simply more complex, costly, yet are not as tunable in repetition rate. Their multiple quantum DFB laser is modulated at 10 GHz, producing linearly chirped 20

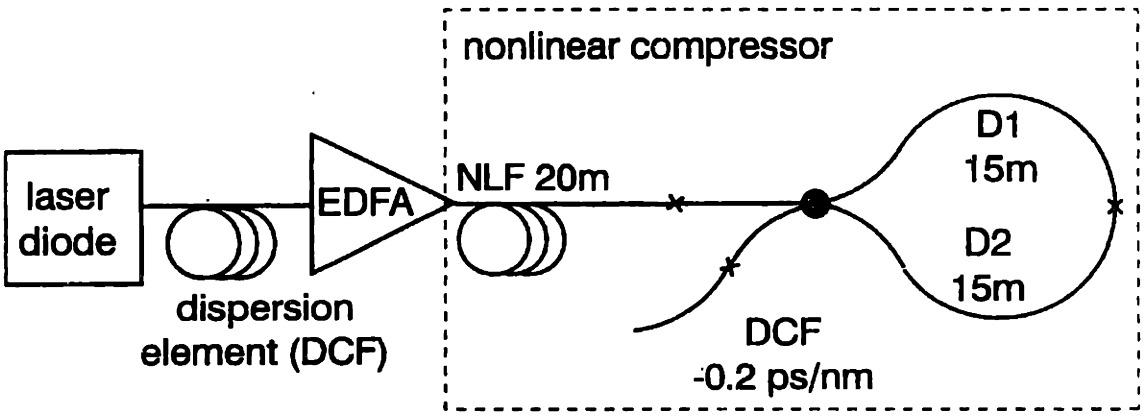

Figure 4-18: Experimental setup of the high-quality laser diode pulse compression scheme; after Ref. [5].

ps pulses. Following both linear and nonlinear compression, the compressed pulses are cleaned up in a DILM, yielding pedestal-free 300 fs pulses, which are then spectrally sliced using a 16 × 16 AWG with a channel spacing of 1.6 nm (200 GHz). As the final output, sixteen 10 Gb/s channels of clean 5-ps pulses are available on the ITU frequency grid (Fig. 4-21).

4.5.2 Applications in 640 Gb/s TDM Transmission

N. Nakazawa and K. Tamura at the NTT Optical Network Systems Laboratories in Kanagawa, Japan, recently demonstrated a 640 Gb/s TDM transmission over a distance of 60 km [7,8]. Data pulses at 10 Gb/s from a fiber laser are time-multiplexed by a factor of 64 to 640 Gb/s using a planar lightwave circuit. The reader should bear in mind that the bit period at 640 Gbit/s is only 1.6 ps, which is even shorter than the 3 ps pulses available from the original fiber laser. In order for this kind of time-multiplexing to be successful, a dispersion-imbalanced nonlinear optical loop mirror is used to clean up the pedestals of the compressed femtosecond pulse train. (Fig. 4-22).

The seed pulse source is a 10-GHz regeneratively mode-locked fiber laser (RMFL) emitting transform-limited 3.5 ps pulses with a tuning range of 32 nm. The pulses are amplified to an average power of 140 mW and then compressed adiabatically in a

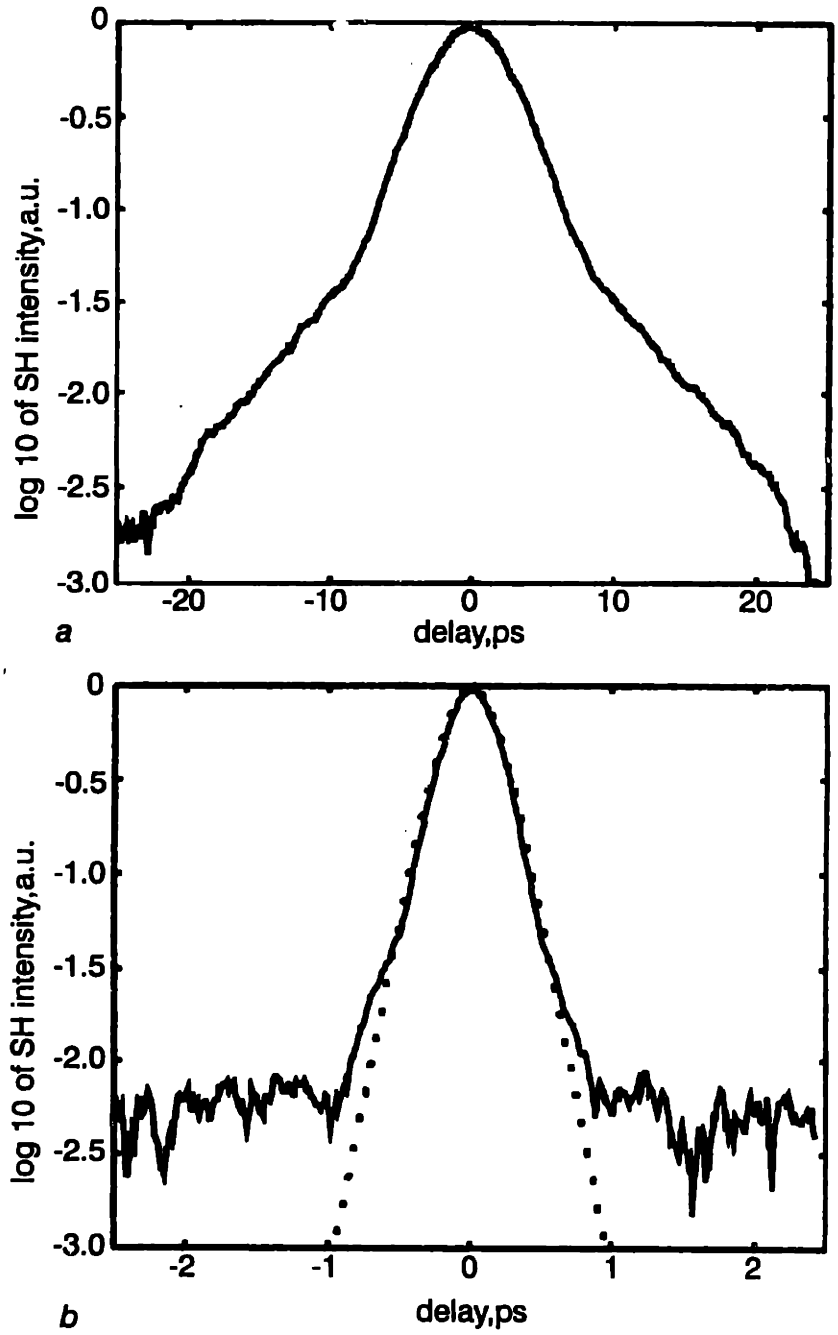

Figure 4-19: Autocorrelation traces of the signal at the input and output of the DILM. Input pulse width = 22 ps; compressed output pulse width = 270 fs; the dash line is the calculated autocorrelation trace of an ideal 270 fs hyperbolic-secant pulse; after Ref. [5].

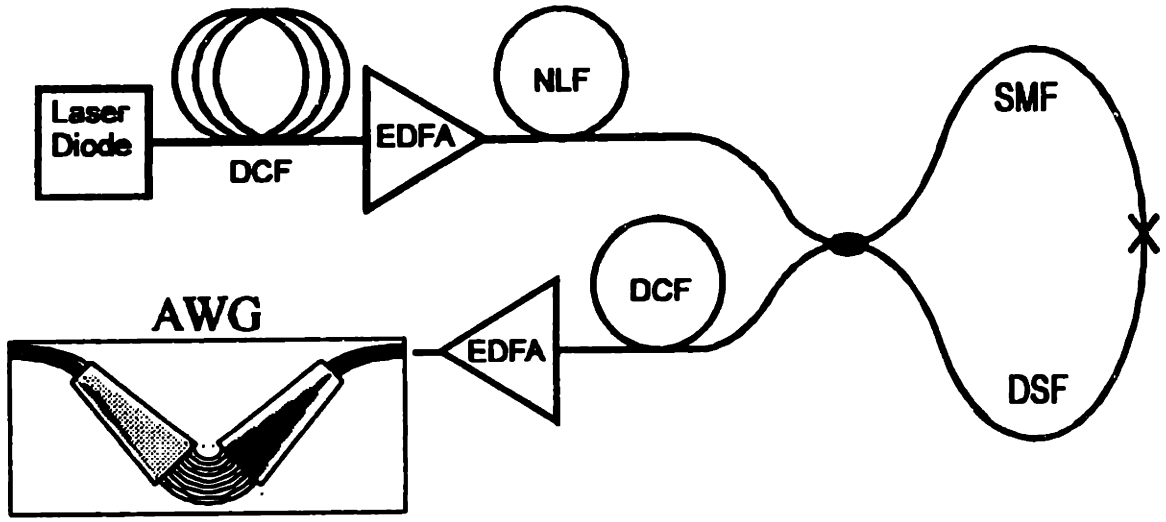

Figure 4-20: Experimental setup. DCF = dispersion compensating fiber; DSF = dispersion-shifted fiber; SMF = standard fiber; AWG = arrayed waveguide grating; after Ref. [6].

dispersion-flattened dispersion-decreasing fiber (DDF). The autocorrelation trace of the compressed pulses have a broad pedestal at −22 dB from the peak (Fig 4-23).

To reduce the pulse pedestals, the researchers use a dispersion-flattened and dispersion-flattened NOLM for pulse cleanup. Dispersion flattening is needed so as to maintain the broad 32 nm tuning range in the output. The optical spectra before and after the DILM are shown in Fig. 4-23. The spectral spikes in the input are almost completely extinguished. Likewise, the autocorrelation shows no sign of a pedestal down to approximately −40 dB below the pulse peak, which is the measurement limit of the autocorrelator. Furthermore, by operating the loop mirror at a regime where the transmissivity is a *decreasing* function of input power, a self-limiting effect is observed, which minimizes the intensity fluctuations in the pulse source. Previously, an intra-cavity self-limiting effect was studied by [44] and then demonstrated by [45].

Since a train of 210 fs transform-limited and pedestal-free pulses is now readily available for ultra high bit rate TDM experiments, Nakazawa *et al.* first modulate the pulses with a $2^{15} - 1$ PRBS, then time-multiplex the data up to 640 Gb/s, and finally launch the high bit rate stream into a 60 km dispersion- managed transmission line (Fig. 4-24). Using another NOLM to demultiplex the signal down to the original

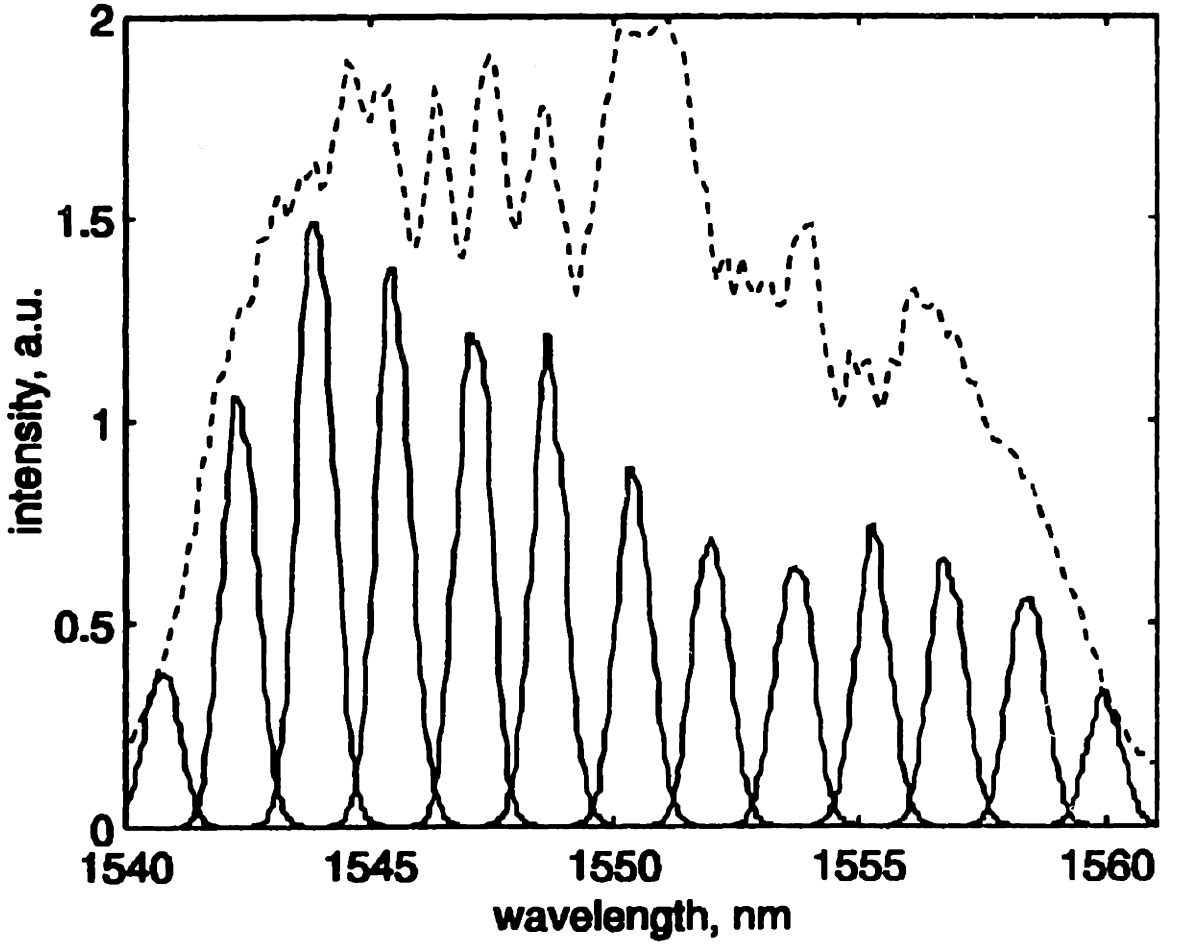

Figure 4-21: Optical spectra of the signal at the DILM output (dashed line) and at the AWG outputs (solid lines); after Ref. [6].

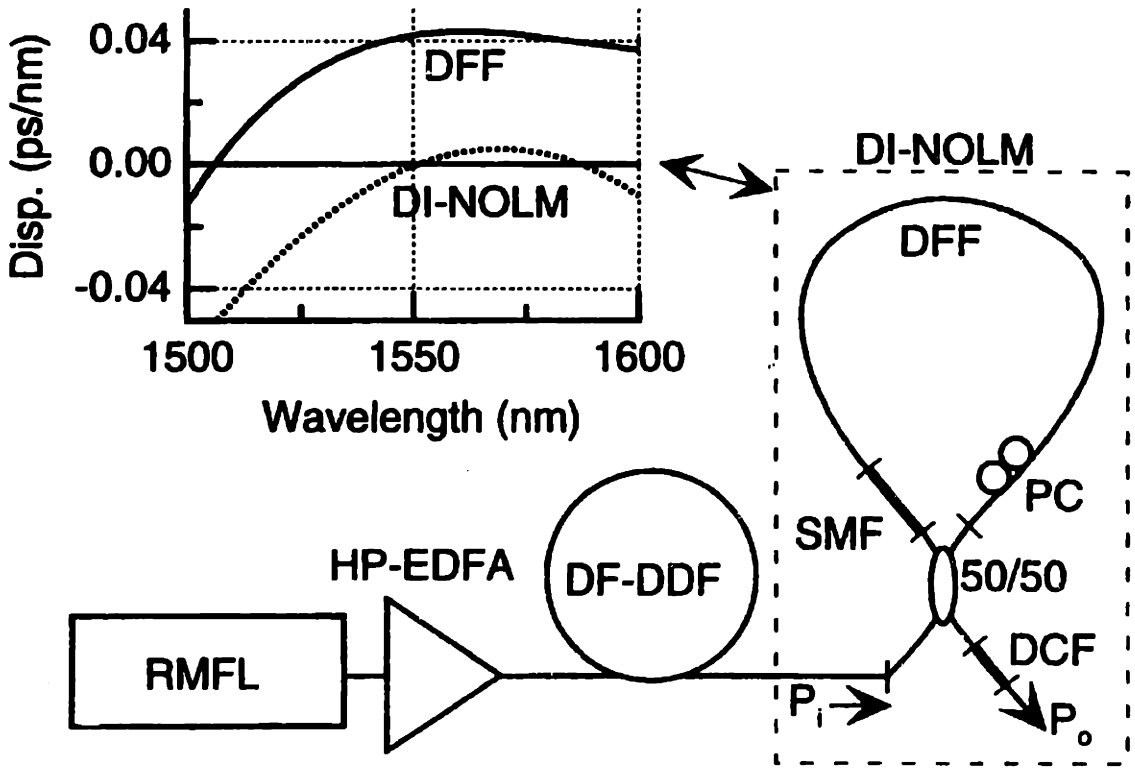

Figure 4-22: Experimental arrangement. Inset shows dispersion measurement of DFF (solid) and of dispersion-flattened DI-NOLM (dashed). $L_{DFF} = 100$ m, $L_{SMF} = 1$ m, and $L_{DCF} = 0.1$ m. DFF = dispersion-flattened fiber; PC = polarization controller; RMFL = regeneratively mode-locked fiber laser; HP-EDFA = high-power erbium-doped fiber amplifier; after Ref. [7].

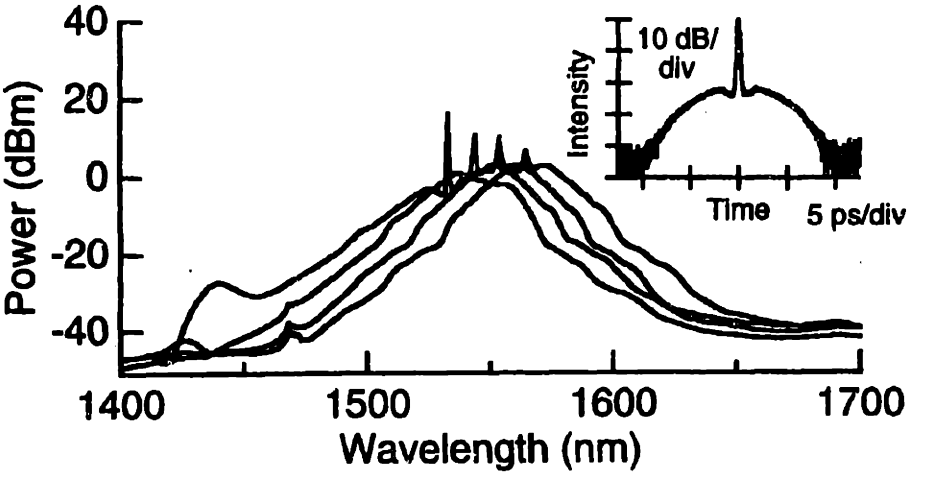

(a)

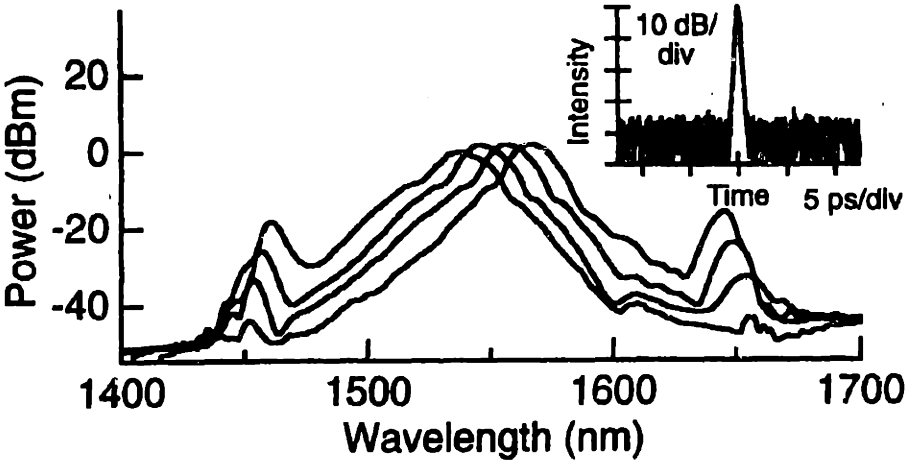

(b)

Figure 4-23: (a) Output spectra from dispersion-flattened DDF. Inset shows autocorrelation of pulse at 1554 nm. (b) Output spectra from dispersion-flattened DI-NOLM. Inset shows autocorrelation of pulse at 1554 nm; after Ref. [7].

10 Gb/s, they recorded a receiver sensitivity of -23 dBm at 10^{-10} BER.

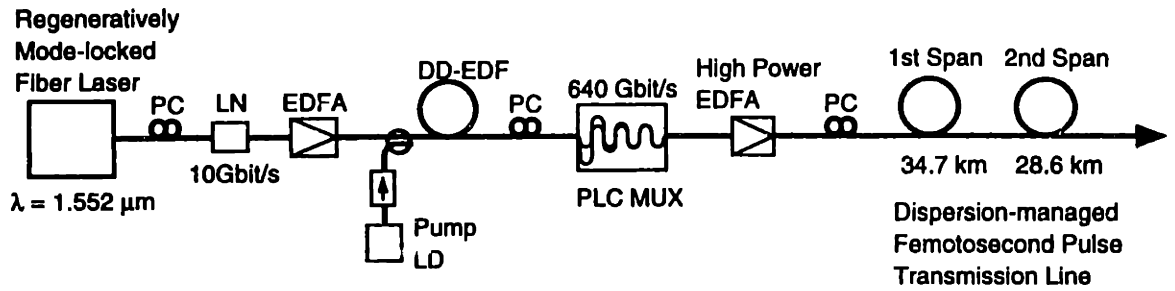

Figure 4-24: Generation and 64× multiplication of a femtosecond pulse train, and the transmission of a single TDM channel at 640 Gb/s over 60 km of a dispersion-managed fiber link; after Ref. [8].

Chapter 5

In-band Amplified Spontaneous Emission Noise Filtering with a DILM

In a communication system with in-line optical amplifiers, the presence of amplified spontaneous emission (ASE) noise in the signal stream lowers the signal-to-noise ratio (SNR) of the signal at the receiver, resulting in a higher bit error rate (BER) in transmission. We demonstrate here the possibility of using a dispersion-imbalanced loop mirror to perform nonlinear noise filtering on such a noise-loaded pulse stream. Previously, a dispersion-imbalanced Mach-Zehnder was proposed as a device for pulse processing [46]. As well, Olsson and Andrekson used a NOLM to filter mostly out-of-band noise, where the signal bandwidth to the noise bandwidth is 1:500 [47]. In this experiment, we will focus on the filtering of in-band noise, which an optical band-pass filter is incapable of rejecting.

As an overview, we compare the features and drawbacks of various types of nonlinear loop mirrors in Table 5.1. Regarding cw switching, for a narrow bandwidth signal, the effect of dispersion in the loop is negligible, hence the DILM remains non-transmitting for all intensities. This is the unique feature of the DILM that gives it a superior extinction ratio in comparison with other imbalancing schemes (gain, asymmetric coupler). Fig. 5-1 illustrates the theoretical transmissivity of a 42/58

Table 5.1: Comparison of various types of nonlinear optical loop mirrors.

Types of loop mirror	**Mechanism for imbalance**	**Drawbacks**
NOLM	asymmetric coupler	linear leakage, cw switching
NALM	asymmetric location of gain medium	EDFA adds ASE, cw switching
Loss-imbalanced loop mirror	asymmetric location of loss element	cw switching
Dispersion-imbalanced loop mirror	asymmetric dispersion map	??

NOLM for cw inputs.

5.1 Loop Design

We assume that the input pulse to the DILM has a hyperbolic secant shape $u(0,t) = N\text{sech}(t)$. Since dispersion varies along the loop, the normalization is done at the fiber segment with the largest amount of dispersion, i.e., $D_1 = 1$ and $|D_2| < |D_1|$. Since the nonlinear Schrödinger equation is self-similar: for $\lambda \neq 0$, $z \longrightarrow \lambda^2 z$, $t \longrightarrow \lambda t$, and $u \longrightarrow u/\lambda$, the dispersion-imbalanced loop mirror studied in a previous experiment with femtosecond pulses [9, 10] can be easily scaled so that it will now work with picosecond pulses, which are the natural bits for high bit-rate soliton transmission experiments [48, 49]. In other words,

$$z_0 = \frac{\pi}{2} z_c \propto \frac{\tau^2}{|D|}\,, \tag{5.1}$$

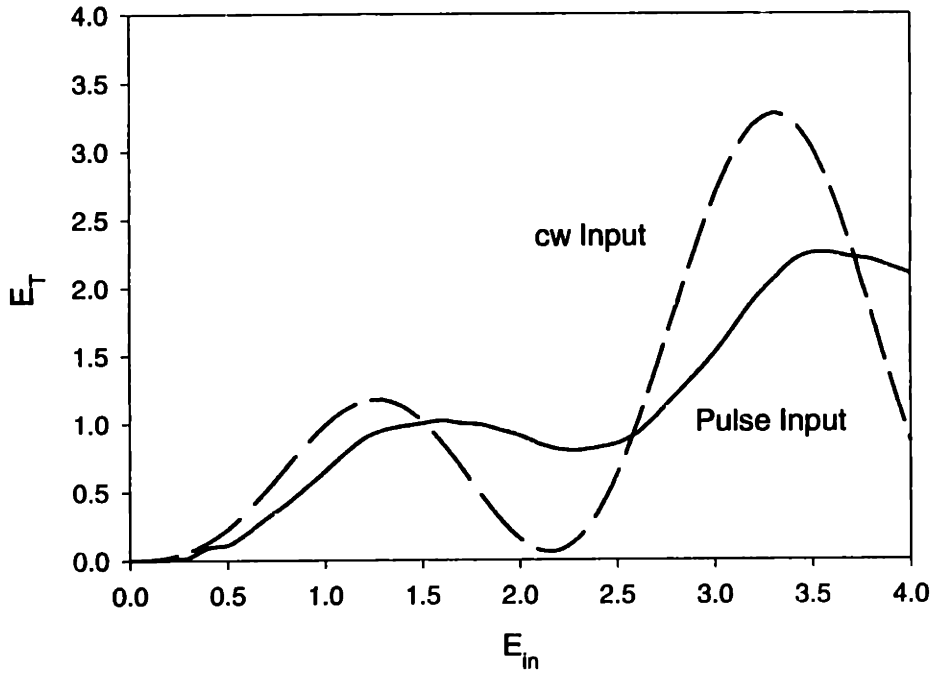

Figure 5-1: Theoretical transmissivity of a NOLM, built with a 42/58 coupler, for pulses and cw input; $E_{in} = N^2$ and $E_T = TN^2$.

and

$$E_{N=1} \propto \frac{|D|}{\tau} . \tag{5.2}$$

Since the switching energy scales with the inverse input pulsewidth, it is lowered substantially for communication systems with picosecond pulses. For example, the pulse source available for our experiment can generate hyperbolic secant pulses with a FWHM of 15 ps, allowing the switching pulse energy to reduce 25 times to 4 pJ.

Other specifications for the design are: i) the average optical power available (after post amplification) in the receiver is 12 - 14 dBm, or 15.8 - 25.1 mW, ii) the input pulses are assumed to have a hyperbolic secant shape, and iii) the material loss in fiber is 0.2 dB/km.

The design parameters are chosen to be $D_1 = 1.0$, $D_2 = 0.5$, $L_1 = 0.5z_0$, and $L_2 = 0.45z_0$, as a result of conducting extensive numerical simulations using parameters that are physically realizable.

5.2 Simulations of a Loop Mirror Design with a 10 Gb/s Data Pattern

Using our design, the propagation of a data pattern (100110100) at 10 Gb/s through the dispersion-imbalanced loop mirror is simulated using a split-step Fourier algorithm using 1024 temporal steps. The pulse width is assumed to be 15 ps FWHM. Note that in this design, the input pulses are $N = 2.2$ solitons (with respect to the input fiber where $D = -4.60$ ps^2/km). Fig. 5-2 shows the input, transmitted, and reflected pulse patterns on a logarithmic scale. One can conclude that the pulse-to-pulse crosstalk induced by the loop mirror is minimal (greater than 40 dB).

Next, additive, white gaussian noise with zero mean and normalized variance 0.04 is included in the input data. Fig. 5-3 plots the intensity of the input, transmitted, and reflected patterns on a logarithmic scale. The noise is cleaned up substantially in the output, where the optical SNR increases by about 14 dB. Thus, the loop mirror design can function as an optical regenerator in a transmission link.

5.3 Thresholding

Before one can study how the dispersion-imbalanced nonlinear optical loop mirror, which is regarded as an non-instantaneous thresholder, combats ASE noise, one should consider the simplest case of an ideal instantaneous intensity thresholder. As shown in Fig. 5-4, an ideal thresholder having a sharp step-like response can open up the "eye" of a noisy stream of ZEROs and ONEs, provided that the threshold is set optimally. The distributions of the ZEROs and ONEs in the output signals will be delta functions. Although the Q factor now becomes infinite (i.e., the "eye" is perfectly open), the bit error rate of the system at this point remains the same, because the tails (outlying members) of both distributions are incorrectly restored to the wrong logic level.

Before we explain why the DILM is a non-instantaneous thresholder, we need to point out the fact that a coherent solitonic ($N = 1$) pulse can propagate while

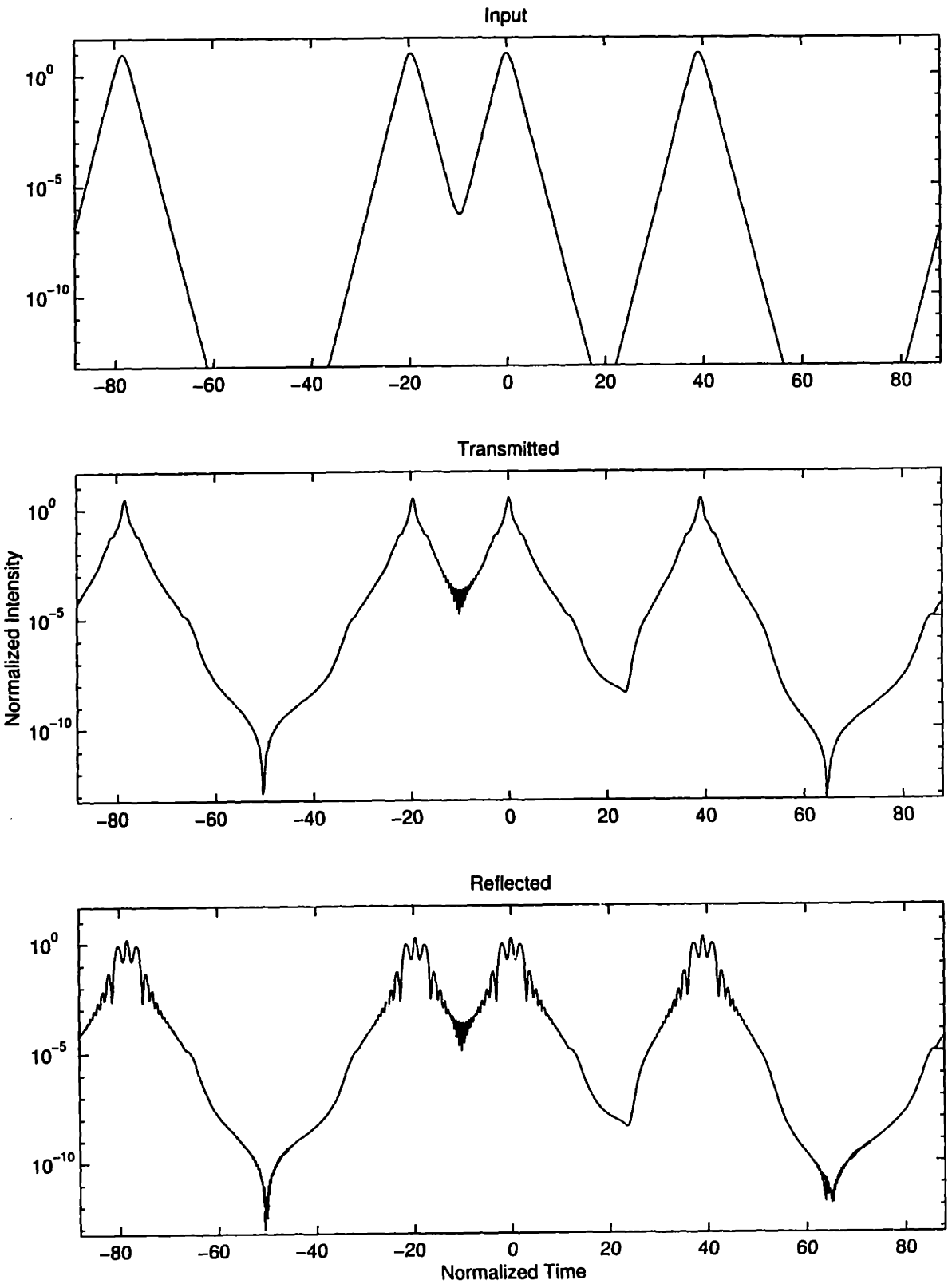

Figure 5-2: Simulated input, transmitted, and reflected pulse patterns. The input pattern is (100110100).

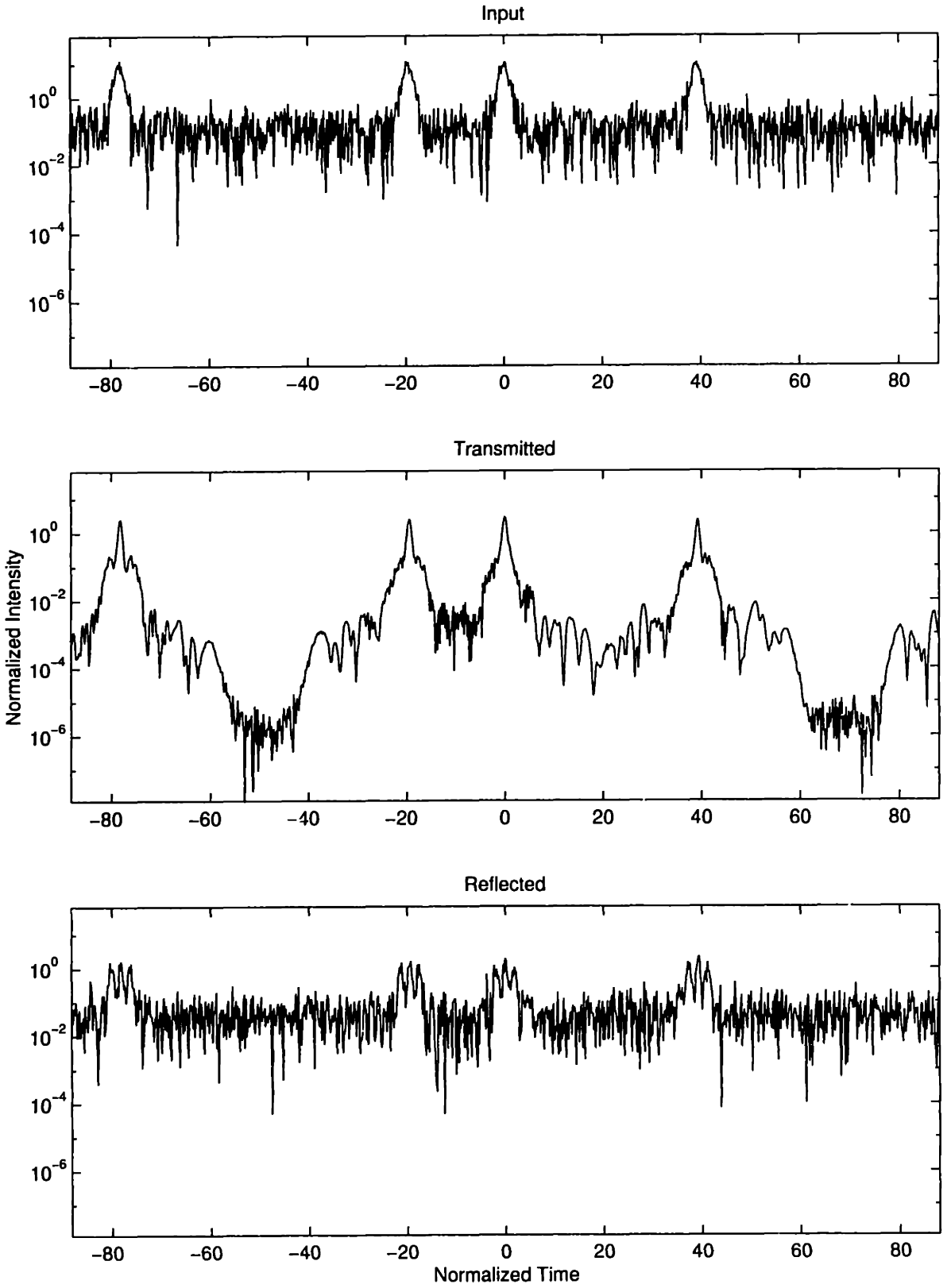

Figure 5-3: Simulated input, transmitted, and reflected pulse patterns. The input is loaded with zero-mean additive white Gaussian noise with a normalized variance of 0.04.

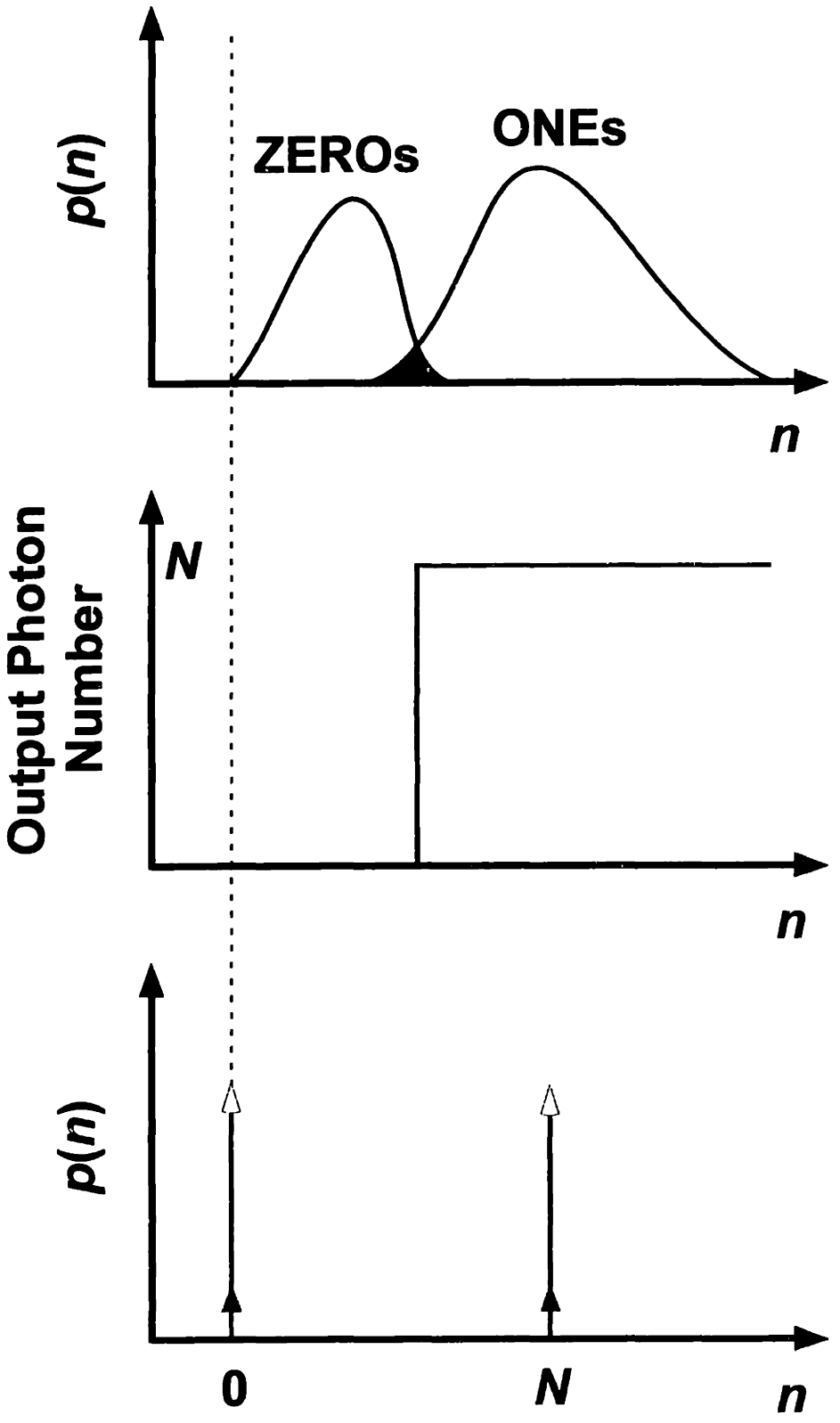

Figure 5-4: Ideal instantaneous intensity thresholding.

maintaining its shape (top); an incoherent noise burst having the same energy will simply disperse (Fig. 5-5). Therefore, if a false ZERO (an incoherent pulse having a significant amount of energy entering the DILM, it will disperse rapidly inside the loop in both directions, resulting in very little leakage in the output. In other words, the DILM can correct false ZEROs and improve the BER. The DILM is also a non-intensity thresholder in the sense that any cw light of sufficient energy will be blocked by the loop. Detailed split-step simulations of coherent and incoherent pulse inputs into the DILM are shown in Fig. 5-6.

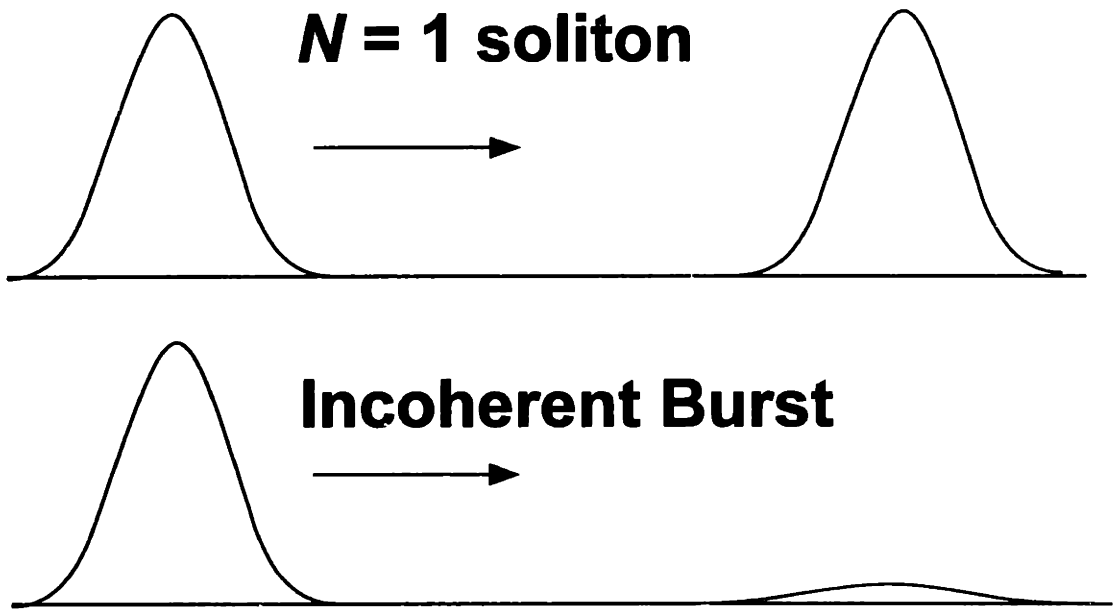

Figure 5-5: A coherent solitonic ($N = 1$) pulse can propagate while maintaining its shape (top); an incoherent noise burst having the same energy will simply disperse.

5.4 Experiment

The experiment setup is shown in Fig. 5-7 [50]. A 10-GHz pulse train, where the 15 ps pulses have a time-bandwidth-product of 0.35 at 1550 nm, is modulated at 10 Gb/s by a lithium niobate amplitude modulator with a $2^{31}-1$ pseudo-random bit sequence. As much as 20 dBm of average optical power is available when the data-encoded pulse train is post-amplified by an erbium-ytterbium co-doped fiber amplifier. The noise

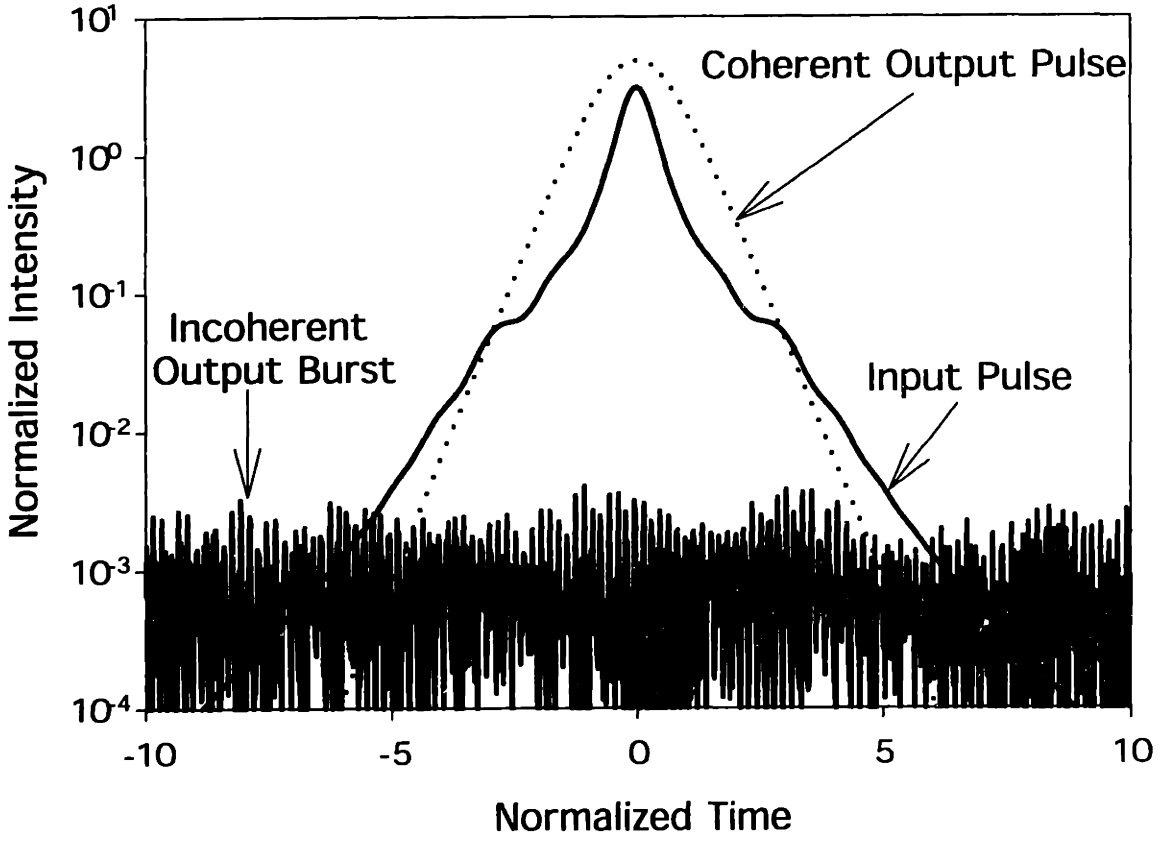

Figure 5-6: Simulated propagations of coherent and incoherent pulse inputs into the dispersion-imbalanced loop mirror. For a coherent input pulse of sufficient energy, a coherent output pulse emerges at the output; on the other hand, incoherent noise bursts with the same energy will be greatly attenuated at the output.

source consists of two erbium-doped amplifier stages in cascade, into which a 1 nm band-pass filter is inserted between the two stages to lower the noise bandwidth and increase the noise spectral power simultaneously. As a result, 8.3 dBm of ASE noise is generated at the signal wavelength with a bandwidth of 1.3 nm. The signal and the ASE noise are both launched into the loop mirror via a 50/50 coupler followed by a three-port optical circulator. One advantage of using this noise-loading technique, compared with the alternative of amplifying an attenuated input signal, is that the levels of signal and noise can be independently adjusted and measured.

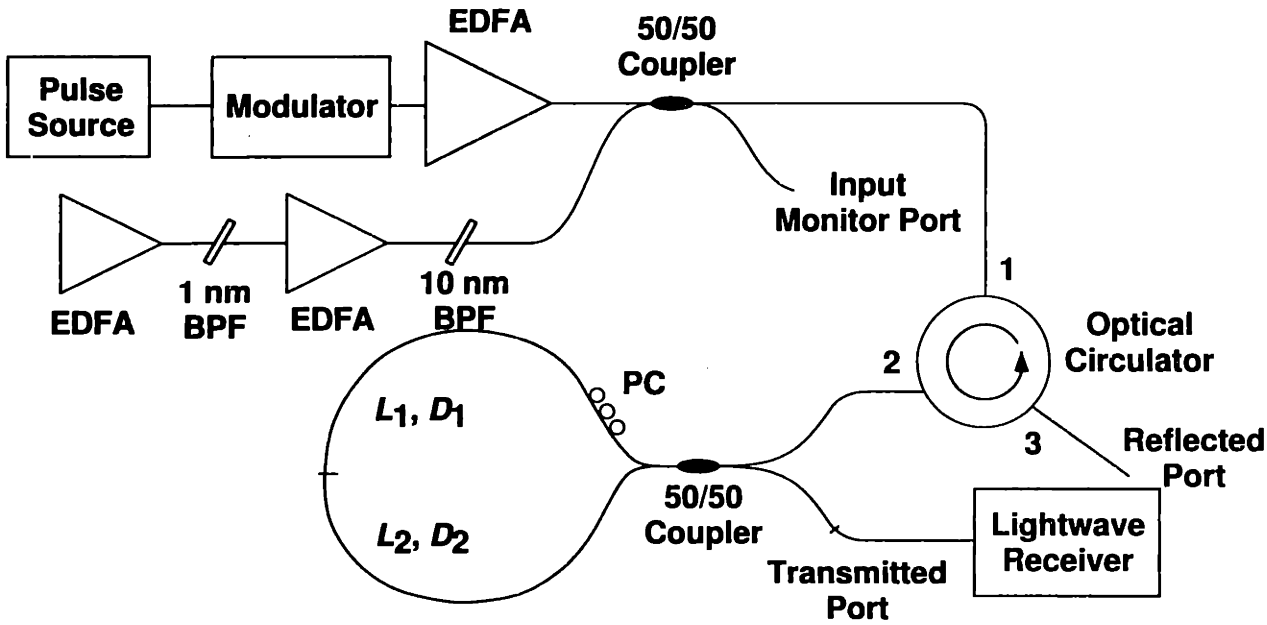

Figure 5-7: Experimental setup: PC, polarization controller; EDFA, erbium-doped fiber amplifier; BDF, band-pass filter.

The dispersion-imbalanced loop mirror is constructed with a 50/50 coupler, 12.62 km of Lucent TrueWave fiber with an anomalous dispersion of +3.52 ps/(nm.km), and 11.36 km of TrueWave fiber with an anomalous dispersion of +1.68 ps/(nm.km) at 1550.0 nm. The losses of the fiber are measured to be 0.201 dB/km and 0.197 dB/km, respectively. To suppress the photoelastic effect, which causes the fiber to act as an acoustic sensor [51], the two fiber spools are housed in hermetically sealed aluminum containers. We deviate from our previous design to operate in the pulse compression regime in order to reduce the generation of dispersive waves, which can introduce crosstalk in the output signal. The optimal loop design is obtained from

running simulations over a large set of possible parameters. In normalized units, the experimental parameters are $N = 2.2$, $D_1 = 1.0$, $D_2 \approx 0.5$, $L_1 \approx 0.5z_0$, and $L_2 \approx 0.45z_0$. The input, and the transmitted signal through the loop mirror, are both fed to an optically pre-amplified lightwave receiver for bit error rate measurements. The receiver, detailed in Fig. 5-8, exhibits a back-to-back sensitivity of -38.7 dBm (105 photons/bit) at 10^{-9} BER for intensity-modulated RZ signals at 1.5 μm. It consists of an optical pre-amplifier, a 1.1 nm band-pass filter to provide rejection of out-of-band noise, an optical saturating amplifier for power limiting, an optical attenuator, and a *pin* detector.

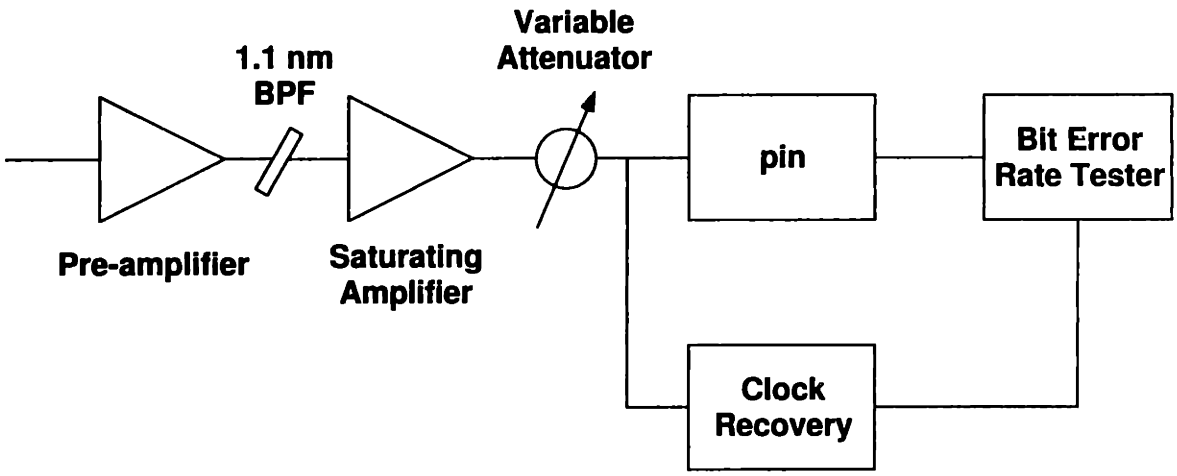

Figure 5-8: Optically pre-amplified receiver.

To minimize the effect of natural birefringence in the fiber, we null the loop transmission at low input power by adjusting the polarization controller. For pulse input without noise injected, the transmitted power as a function of input power is measured and shown in Fig. 5-9. The switching energy corresponding to the first peak is 4 pJ, and the output FWHM pulse width is shortened to 9 ps at that point. The agreement with numerical simulations, computed with a split-step Fourier algorithm, is good. The leakage at low intensities is 0.5%.

Without noise loading, the measured BERs through the loop mirror at 28 mW of input power is shown in Fig. 5-10 as circles. When compared to the BER without the loop mirror (squares), one can see that the insertion of the loop mirror causes no penalty in receiver sensitivity. Furthermore, when in-band ASE noise is added to the

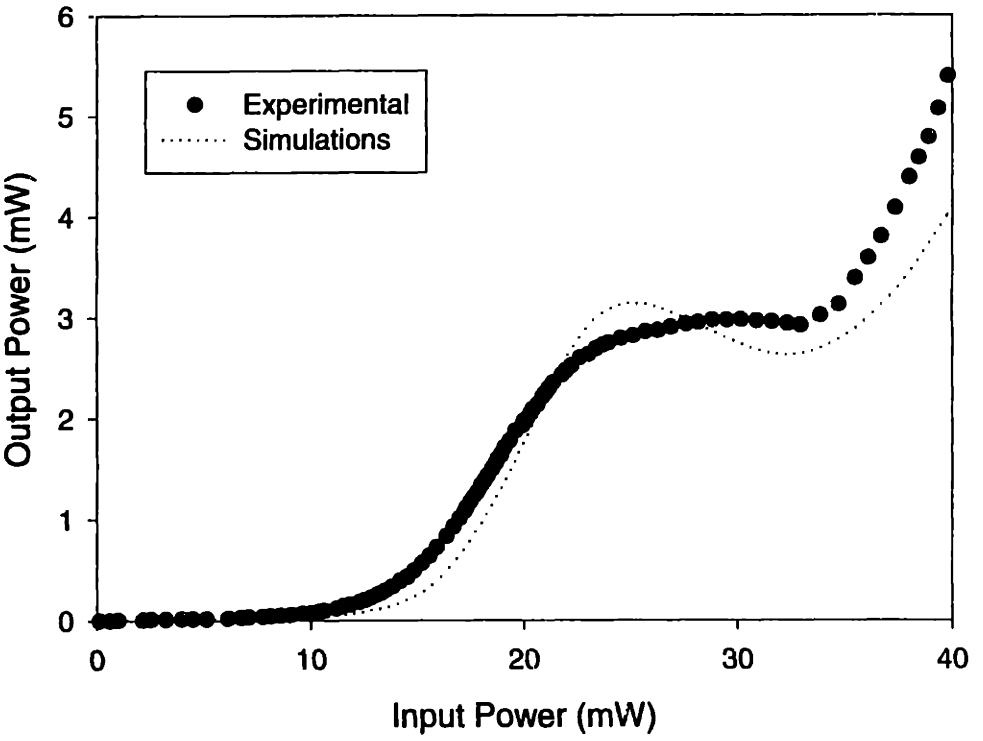

Figure 5-9: Switching characteristics of the dispersion-imbalanced loop mirror. Switching energy at the first peak is 4 pJ for 15 ps pulses.

system such that the input optical signal-to-noise-ratio decreases from 38 dB to 15 dB in 0.2 nm of bandwidth, the degraded sensitivity of −37.0 dBm measured without the loop mirror (triangles) can be improved to −37.7 dBm (inverted triangles). Closer examination of the loop mirror operation reveals that its noise-canceling ability is bias-dependent. In Fig. 5-11, the sensitivities without noise-loading through the loop mirror are shown as squares. For reference, the transmissivity as a function of input power is also plotted. One can see that other than when operating between points C and D, propagating a noise-free signal through the loop mirror incurs a penalty in sensitivity. When noise is added, the only bias range where there is an improvement in sensitivity is 25-32 mW, around point D, where the transmissivity is decreasing with increasing input power. Naturally, the BER curves in Fig. 5-10 are measured at point D. The eye diagrams obtained at a received power of −37.7 dBm at points A and D are shown in Figs. 5-12 and 5-13. The Q values for all seven cases (points A through F) are 2.3, 3.2, 4.3, 5.8, 4.8, 3.2, and 5.2, respectively.

The explanation for the bias dependence of sensitivity can be found from saturable absorber theory. An artificial saturable absorber encourages high intensities to build up from noise. Likewise, at bias points A and B, any fluctuations in the input pulse will be amplified in the output, causing the eye to shrink, as shown in Fig. 5-12. On the other hand, reverse saturable absorbers have been used to counteract pulse-to-pulse variations [44,45]. It is in this stabilizing regime (point D), where transmissivity decreases with increasing intensity, that the loop mirror keeps the output pulses quiet and cleans up the noise between them temporally. Alternatively, it can be concluded from Fig. 5-9 that the best noise suppression should be in a region where the output power is almost insensitive to the variation of the input power (between 24 mW and 33 mW of input power).

Rayleigh scattering is a fundamental fiber loss mechanism arising from random density fluctuations frozen into the fused silica during manufacturing [52]. These fluctuations in the refractive index scatter light in both the forward and backward directions. Although the amount of back scattered light in a typical piece of fiber of sufficient length is very small (about -30 dB of the input light), due to the interfero-

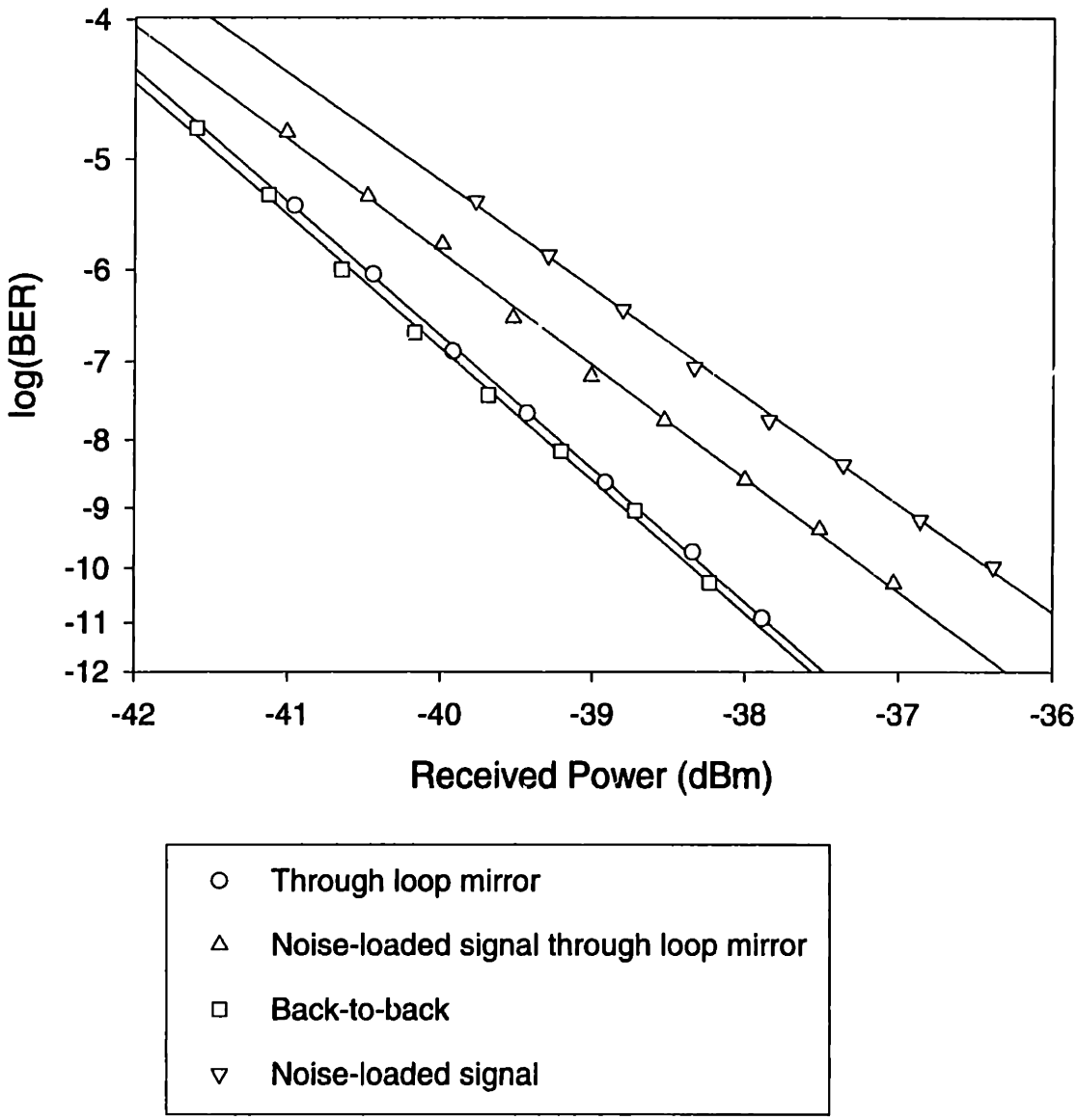

Figure 5-10: Measured bit error rate curves as a function of power received at the receiver.

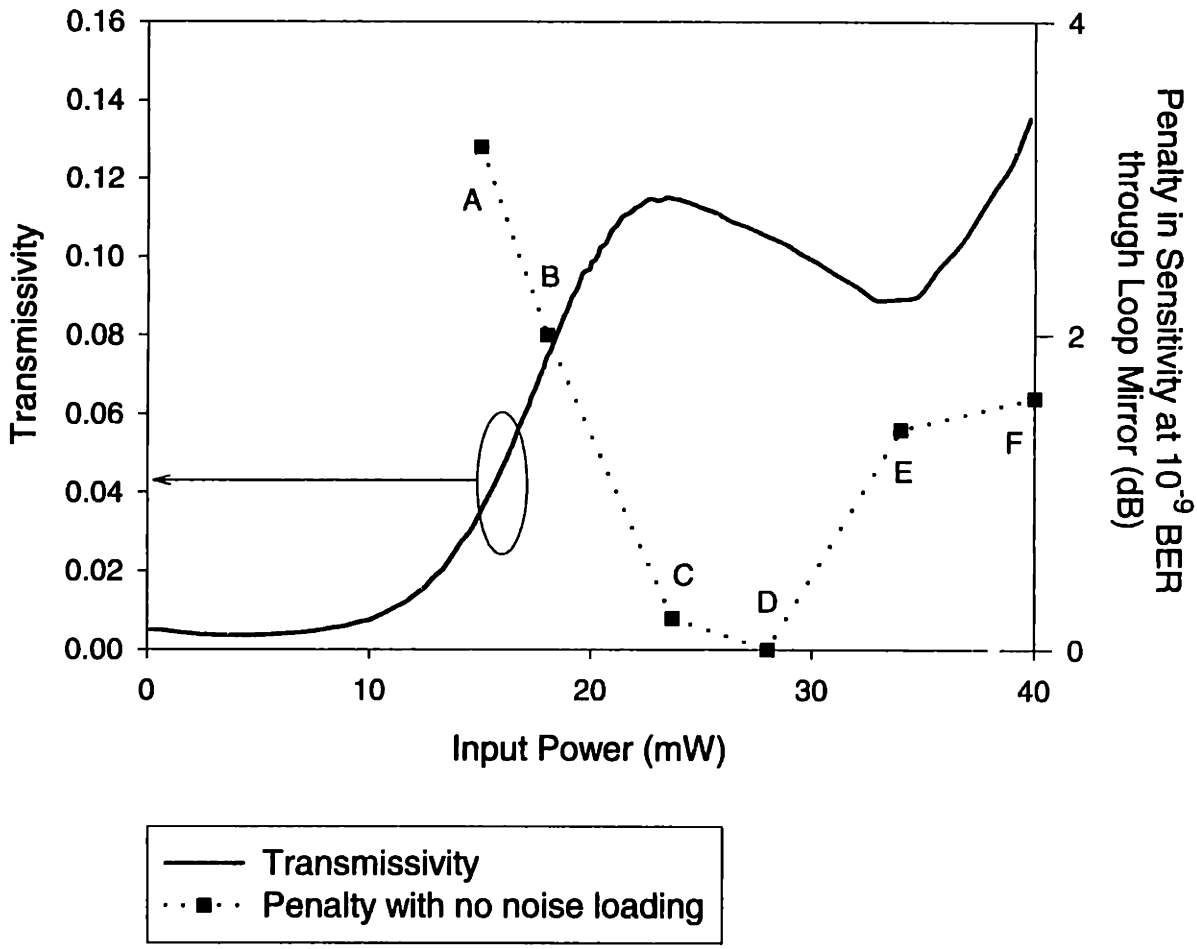

Figure 5-11: Penalties in receiver sensitivity through the loop mirror as a function of the loop mirror operating bias. The bias points A and D are also referenced in Figs. 5-12 and 5-13. The transmissivity of the loop mirrer as a function of input power is also shown.

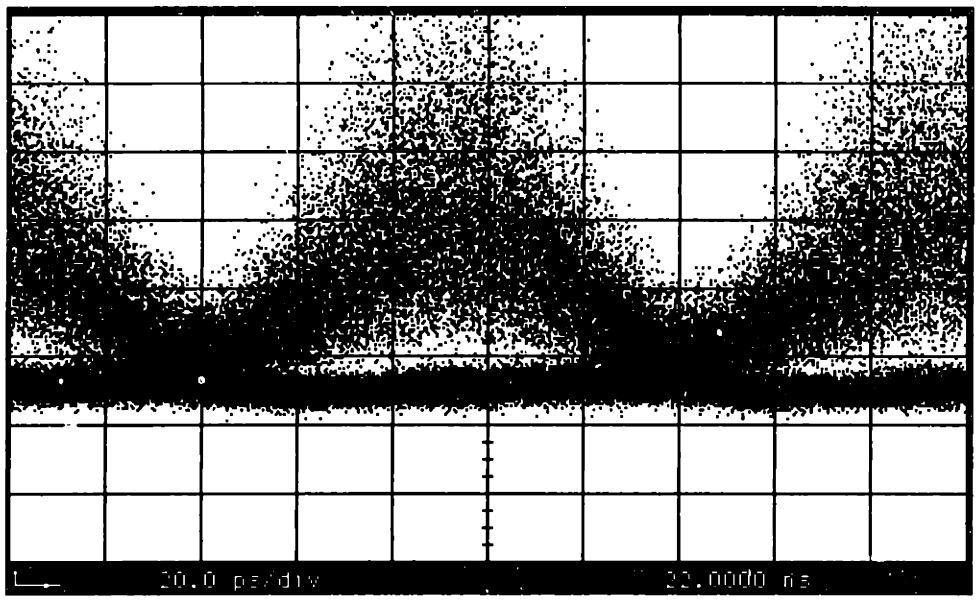

Figure 5-12: Eye diagrams obtained at a received power of −37.7 dBm, at the worst operating point (point A) with in-band noise of bandwidth 1.3 nm and average power 5.3 dBm added to the system.

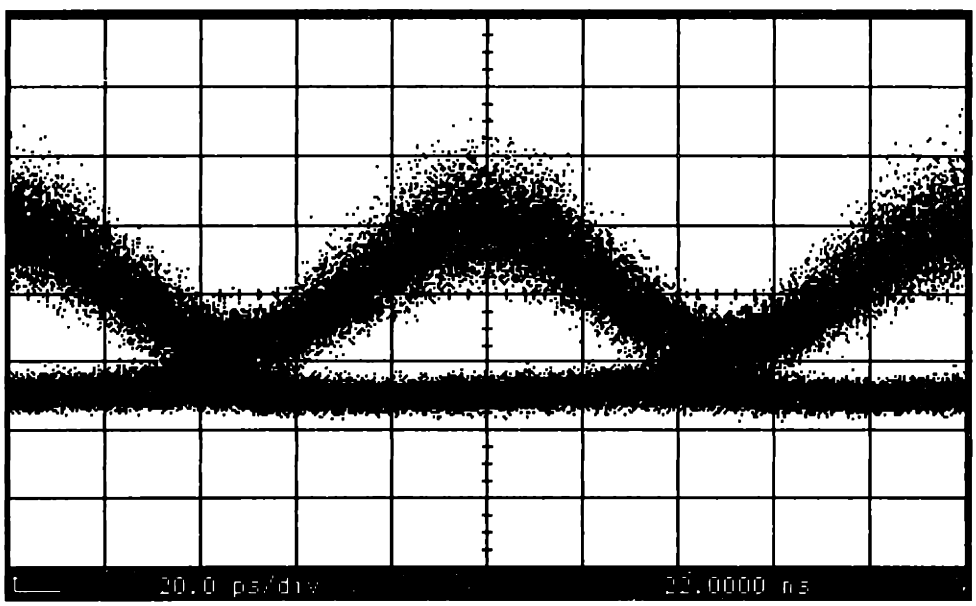

Figure 5-13: Eye diagrams obtained at a received power of −37.7 dBm at the best operating point (point D) with in-band noise of bandwidth 1.3 nm and average power 5.3 dBm added to the system.

metric nature of the loop mirror, this effect is the limiting factor in determining the maximum achievable SNR in the output of the loop mirror.

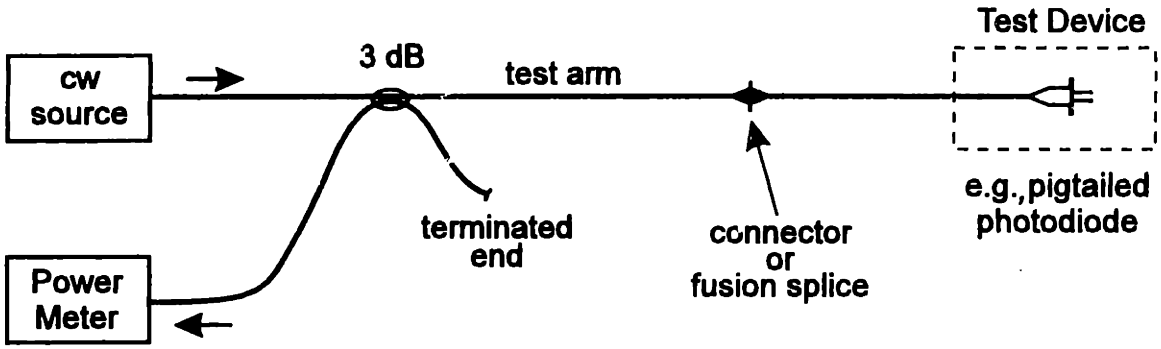

Figure 5-14: Experiment setup for measuring the total return loss (backward Rayleigh scattering included) an optical component; after Ref. [2]

A backward Rayleigh measurement was performed on the TrueWave fiber by disconnecting the two fiber segments inside the loop mirror and measuring the backscattered light via a 50/50 fiber coupling. Fig. 5-14 depicts the general experimental setup for measuring the total return loss, which includes the backward Rayleigh scattering, from a device. To minimize the Fresnel reflection from the end facet, which can be as high as 4% if untreated, the fiber end is cleaved and polished with a sufficient angle. In addition, reflectivities from fiber connectors can be made to be less than -60 dB if angle-polished connectors are used.

The results shown in Fig. 5-15 show that the amount of Rayleigh backscattering is -29.3 dB of the incident light. Since the ratio of scattered light to incident light does not depend on the input power over the entire measurement range, one can conclude that the amount of stimulated Brillouin scattering is negligible, which is not surprising since the 15-ps input pulses are sufficiently broadband.

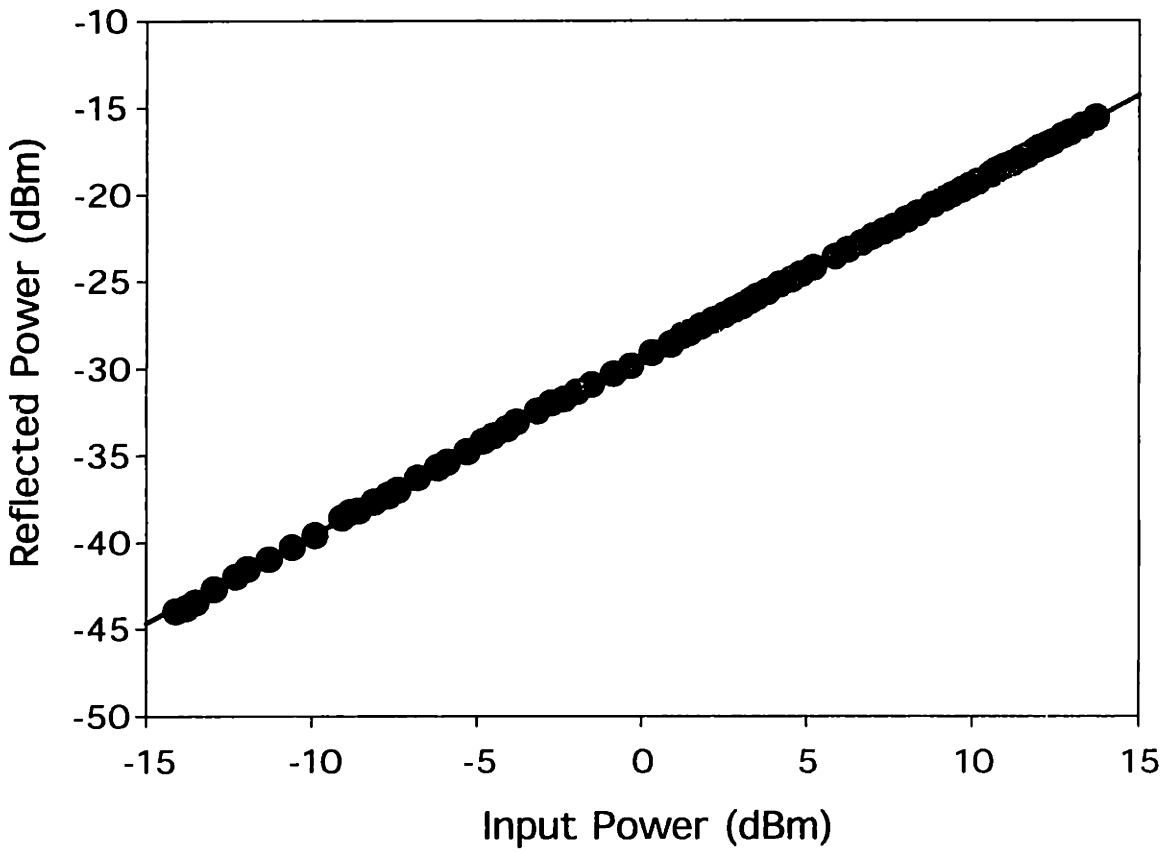

Figure 5-15: Rayleigh backscattering measurement. The amount of Rayleigh backscattering is −29.3 dB of that of the incident light.

Chapter 6

Conclusions and Future Work

This chapter summarizes this thesis. In Chapter 2, the photon statistics of ZEROs and ONEs in a optically preamplified receiver are measured and are found to agree with the predictions of quantum photodetection theory. In Chapter 3, a novel nonlinear pulse filter is described and demonstrated. It has since been used in cleaning up pulses from a fiber laser in 640 Gb/s TDM transmission experiments, as well as used in generating clean and tunable multiwavelength WDM sources at 10 Gb/s. In Chapter 4, the pulse filter is used to clean up in-band ASE noise in a 10 Gb/s RZ signal.

6.1 Thought no. 1

So far we have established excellent agreement between theory and experiment for the photon statistics of ZEROs and ONEs for the cw case *only*. We found out that, in real-life transmission experiments, deleterious effects such as i) detector ringing, which causes intersymbol interference (ISI), and ii) pattern-dependent effects, could broaden/smear out the probability distributions of the ZEROs and ONEs. These effects together conspire to prevent us from observing the quantum-limited receiver sensitivity of 38 photons/bit in our best receivers (according to the specifications, some optical preamplifiers do have a noise figure as low as 3.5 dB). Although there have been some numerous effort to model these non-ideal behaviors [53–63], these

models often fall short of predicting real system behaviors because

1. the number of theory/simulation papers outnumbers the experimental ones by at least 20 to 1. help

2. when trying to model ISI while keeping the calculations tractable at the same time, most researchers often work with a 3-bit pattern (with $2^3 = 8$ combinations), which, in my opinion, is inadequate because we are dealing with, at the minimum, a $2^7 - 1$ or a $2^{15} - 1$ pseudorandom sequence in the lab.

3. these undesirable effects are incorporated into the models in the probability generating function (PGF) space, which do not yield closed-from expressions in probability distribution space. In other words, it may be simply easier just to run the experiments directly instead.

Based on my observations above, I see a clear need in continuing work on bridging the gap between theory and experiments in the studying of real-life high-bit-rate communication systems.

6.2 Thought no. 2

Even with the state-of-the-art 10 Gb/s $\times$ 64 channel dense WDM systems reported at OFC '99, we are still underutilizing the available EDFA bandwidth. It seems that going from 10 Gb/s (OC-192) to 40 Gb/s (OC-768) in each channel is imminent.

Since Nakazawa and Tamura demonstrated the short-haul terrestrial transmission of a single TDM channel at 640 Gb/s, made feasible with the pulse-cleanup DILM device, we should take a closer look at some of the higher-order pulse propagation effects in a DILM. One should

1. study the effect of Raman self-frequency shift (RSFS) as the steady-state pulse inside the loop can be as short as 230 fs. If the amount of RSFS is significant, the two counterpropagating pulses can have very different center frequencies and group delays (!!) after traversing the loop once.

2. study the effect of four-wave mixing between the counterpropagating streams. This effect, already observed by Tamura and Nakazawa [7] becomes more significant as the duty cycle of the pulses increases.

3. study the effect of third-order dispersion (TOD) on intra-loop pulse propagation. Similar to RSFS, TOD can downshift the center frequency of a pulse and cause a change in its group delay as well.

Appendix A

Normalizing the Evolution Equation

The material in this appendix was written by Dr. John D. Moores and Dr. Farzana I. Khatri back in 1988. It also appeared in Dr. Khatri's Ph.D. thesis [64].

A.1 Master Equation with Group Velocity Dispersion

This is a summary of how to normalize the Master Equation. Note that it is normalized to bright solitons in media with anomalous group velocity dispersion (GVD) (and positive Kerr effect), and therefore, $\beta_2 = -|\beta_2|$.

The unnormalized Master Equation is as follows:

$$\begin{aligned} \frac{\partial u}{\partial z} + \sigma \frac{\partial u}{\partial t} &= \left\{ (i\psi + g - l) + \left(\frac{g}{\Omega_g^2} + \frac{1}{L_f \Omega_f^2} \right) \frac{\partial^2}{\partial t^2} \right\} u \\ &+ \left\{ i \frac{|\beta_2|}{2} \frac{\partial^2}{\partial t^2} + \frac{\beta_3}{6} \frac{\partial^3}{\partial t^3} + i \frac{\beta_4}{24} \frac{\partial^4}{\partial t^4} \right\} u - i c_R \delta_3 \frac{\partial |u|^2}{\partial t} u \\ &+ \left\{ (\gamma_3 + i\delta_3)|u|^2 + (\gamma_5 + i\delta_5)|u|^4 \right\} u \,. \end{aligned} \tag{A.1}$$

Here u is the complex field, z is distance, t is the (possibly shifting) time coordinate,

σ is the slip with dimensions of inverse velocity (this term can be scaled out of a single nonlinear Schrödinger equation via the shifting time coordinate, but appears in the coupled Master equations for two polarizations when the medium is birefringent - furthermore, if one of the two coupled equations is in the coordinate frame moving with its pulse, then the other equation has a slip $\sigma = \pm\Delta n/c$, where Δn is the index of refraction difference between the two polarization axes, and c is the vacuum speed of light - note that the beat length $L_b = \Delta n/\lambda$), ψ is a phase shift per length, g is the (saturated) linear gain per length, l is the linear loss per length, Ω_g is the spectral half-width at half maximum intensity of the (homogeneously-broadened) gain, Ω_f is the spectral half-width at half maximum intensity of the net passive (static) filtering, L_f is a characteristic length for Ω_f, $\beta_m, m = 2, 3, 4$ are the mth-order coefficients of group-velocity dispersion, c_R is the effective Raman relaxation time, γ_3 is the third-order saturable absorber gain, δ_3 is the Kerr coefficient (self-phase modulation), γ_5 is the fifth-order saturable absorber gain (usually negative, and therefore a loss), and δ_5 is the fifth-order self-phase modulation coefficient.

To normalize, first let

$$\begin{aligned} t &\longrightarrow t_n\tau \\ z &\longrightarrow z_n z_c \end{aligned}$$

where the normalized time and space variables are t_n and z_n respectively, $\tau \approx 0.56729632855\,\tau_{\mathrm{FWHM}}$, τ_{FWHM} is the pulse width at half-maximum intensity, and z_c is a characteristic length scale which shall be determined below, where we normalize the dispersion coefficient. The choice of time scale is such that normalized sech $(\frac{t_n}{N})$ corresponds to a pulse whose FWHM is $N\tau_{\mathrm{FWHM}}$, in real units.

Next, you high school sophomores should use the chain rule and figure out derivatives like this:

$$\begin{aligned} \frac{\partial u}{\partial z} &= \frac{\partial u}{\partial z_n}\frac{dz_n}{dz} = \frac{1}{z_c}\frac{\partial u}{\partial z_n} \\ \frac{\partial u}{\partial t} &= \frac{\partial u}{\partial t_n}\frac{dt_n}{dt} = \frac{1}{\tau}\frac{\partial u}{\partial t_n}. \end{aligned}$$

Similarly, with the second and third derivatives,

$$\begin{aligned}\frac{\partial^2 u}{\partial t^2} &= \frac{\partial}{\partial t}\left(\frac{1}{\tau}\frac{\partial u}{\partial t_n}\right)\frac{dt_n}{dt} = \frac{1}{\tau^2}\frac{\partial^2 u}{\partial t_n^2} \\ \frac{\partial^3 u}{\partial t^3} &= \frac{1}{\tau^3}\frac{\partial^3 u}{\partial t_n^3}\,.\end{aligned}$$

Making these replacements, the Master Equation becomes:

$$\begin{aligned}\frac{\partial u}{z_c \partial z_n} + \frac{\sigma}{\tau}\frac{\partial u}{\partial t_n} &= \left\{(i\psi + g - l) + \left(\frac{g}{\Omega_g^2\tau^2} + \frac{1}{L_f\Omega_f^2\tau^2}\right)\frac{\partial^2}{\partial t_n^2}\right\}u \\ &+ \left\{i\frac{|\beta_2|}{2\tau^2}\frac{\partial^2}{\partial t_n^2} + \frac{\beta_3}{6\tau^3}\frac{\partial^3}{\partial t_n^3} + i\frac{\beta_4}{24\tau^4}\frac{\partial^4}{\partial t_n^4}\right\}u \\ &- i\frac{c_R\delta_3}{\tau}\frac{\partial|u|^2}{\partial t}u \\ &+ \left\{(\gamma_3 + i\delta_3)|u|^2 + (\gamma_5 + i\delta_5)|u|^4\right\}u\,.\end{aligned}$$

Next, we divide out $|\beta_2|/\tau^2$ so that the normalized dispersion is $1/2$. This gives:

$$\begin{aligned}\frac{\tau^2}{|\beta_2|z_c}\frac{\partial u}{\partial z_n} + \frac{\sigma\tau}{|\beta_2|}\frac{\partial u}{\partial t_n} &= \left\{(i\psi + g - l)\frac{\tau^2}{|\beta_2|} + \left(\frac{g}{\Omega_g^2|\beta_2|} + \frac{1}{L_f\Omega_f^2|\beta_2|}\right)\frac{\partial^2}{\partial t_n^2}\right\}u \\ &+ \left\{i\frac{1}{2}\frac{\partial^2}{\partial t_n^2} + \frac{\beta_3}{6\tau|\beta_2|}\frac{\partial^3}{\partial t_n^3} + i\frac{\beta_4}{24\tau^2|\beta_2|}\frac{\partial^4}{\partial t_n^4}\right\}u \\ &- i\frac{c_R\delta_3\tau}{|\beta_2|}\frac{\partial|u|^2}{\partial t}u \\ &+ \left\{(\gamma_3 + i\delta_3)\frac{\tau^2}{|\beta_2|}|u|^2 + (\gamma_5 + i\delta_5)\frac{\tau^2}{|\beta_2|}|u|^4\right\}u\,.\end{aligned}$$

Now, if we set the coefficient for $\partial u/\partial z_n$ to 1, we have that $z_c = \tau^2/|\beta_2|$. Note that

$$z_c = \frac{2z_o}{\pi}$$

where z_o is the soliton period. We would also like to normalize the Kerr coefficient to unity, for which we choose $u = u_n/\sqrt{\delta_3 z_c}$. Finally, we get:

$$\frac{\partial u_n}{\partial z_n} + \frac{\sigma\tau}{|\beta_2|}\frac{\partial u_n}{\partial t_n} = \left\{(i\psi + g - l)\frac{\tau^2}{|\beta_2|} + \left(\frac{g}{\Omega_g^2|\beta_2|} + \frac{1}{L_f\Omega_f^2|\beta_2|}\right)\frac{\partial^2}{\partial t_n^2}\right\}u_n$$

$$
\begin{aligned}
&+ \left\{ i\frac{1}{2}\frac{\partial^2}{\partial t_n^2} + \frac{\beta_3}{6\tau|\beta_2|}\frac{\partial^3}{\partial t_n^3} + i\frac{\beta_4}{24\tau^2|\beta_2|}\frac{\partial^4}{\partial t_n^4} \right\} u_n \\
&- i\frac{c_R}{\tau}\frac{\partial|u_n|^2}{\partial t}u_n \\
&+ \left\{ \left(\frac{\gamma_3}{\delta_3} + i\right)|u_n|^2 + (\gamma_5 + i\delta_5)\frac{|\beta_2|}{\delta_3^2\tau^2}|u_n|^4 \right\} u_n
\end{aligned}
$$

Thus, we can define normalized parameters, so that the normalized equation is of the same form as the unnormalized equation, Eq. (A.1). Thus,

$$
\begin{aligned}
\sigma_n &= \frac{\sigma z_c}{\tau} \\
\psi_n &= \psi z_c \\
g_n &= g z_c \\
l_n &= l z_c \\
L_{f,n} &= \frac{L_f}{z_c} \\
\Omega_{g,n} &= \Omega_g \tau \\
\Omega_{f,n} &= \Omega_f \tau \\
\beta_{2,n} &= 1 \\
\beta_{3,n} &= \frac{\beta_3}{\tau|\beta_2|} = \frac{\beta_3 z_c}{\tau^3} \\
\beta_{4,n} &= \frac{\beta_4 z_c}{\tau^4} \\
c_{R,n} &= \frac{c_R}{\tau} \\
\gamma_{3,n} &= \frac{\gamma_3}{\delta_3} \\
\delta_{3,n} &= 1 \\
\gamma_{5,n} &= \frac{\gamma_5}{\delta_3^2 z_c} \\
\delta_{5,n} &= \frac{\delta_5}{\delta_3^2 z_c}
\end{aligned}
$$

A.2 Master Equation near Zero Group Velocity Dispersion Point

This is a summary of how to normalize the Master Equation at a zero-group-velocity-dispersion (zero GVD) point.

The unnormalized Master Equation, with zero GVD, is as follows:

$$\begin{aligned}\frac{\partial u}{\partial z}+\sigma\frac{\partial u}{\partial t} &= \left\{(i\psi+g-l)+\left(\frac{g}{\Omega_g^2}+\frac{1}{L_f\Omega_f^2}\right)\frac{\partial^2}{\partial t^2}\right\}u \\ &+ \left\{\frac{\beta_3}{6}\frac{\partial^3}{\partial t^3}+i\frac{\beta_4}{24}\frac{\partial^4}{\partial t^4}\right\}u - ic_R\delta_3\frac{\partial|u|^2}{\partial t}u \\ &+ \left\{(\gamma_3+i\delta_3)|u|^2+(\gamma_5+i\delta_5)|u|^4\right\}u\,.\end{aligned}$$

Here u is the complex field, z is distance, t is the (possibly shifting) time coordinate, σ is the slip with dimensions of inverse velocity (this term can be scaled out of the equation via the shifting time coordinate, but appears in the coupled Master equations for two polarizations when the medium is birefringent), ψ is a phase shift per length, g is the (saturated) linear gain per length, l is the linear loss per length, Ω_g is the spectral half-width at half maximum intensity of the (homogeneously-broadened) gain, Ω_f is the spectral half-width at half maximum intensity of the net passive (static) filtering, L_f is a characteristic length for Ω_f, $\beta_m, m = 3,4$ are the mth-order coefficients of group-velocity dispersion, c_R is the effective Raman relaxation time, γ_3 is the third-order saturable absorber gain, δ_3 is the Kerr coefficient (self-phase modulation), γ_5 is the fifth-order saturable absorber gain (usually negative, and therefore a loss), and δ_5 is the fifth-order self-phase modulation coefficient.

To normalize, first let

$$\begin{aligned} t &\longrightarrow t_n\tau \\ z &\longrightarrow z_n z_3 \end{aligned}$$

where the normalized time and space variables are t_n and z_n respectively, $\tau =$

$0.56729632855\,\tau_{\rm FWHM}$, $\tau_{\rm FWHM}$ is the pulse width at half-maximum intensity, and z_3 is a characteristic length scale which shall be determined below, where we normalize the dispersion coefficient. The choice of time scale is such that normalized sech $(\frac{t_n}{N})$ corresponds to a pulse whose FWHM is $N\tau_{\rm FWHM}$, in real units.

Next, you high school sophomores should use the chain rule and figure out derivatives like this:

$$\begin{aligned}\frac{\partial u}{\partial z} &= \frac{\partial u}{\partial z_n}\frac{dz_n}{dz} = \frac{1}{z_3}\frac{\partial u}{\partial z_n}\\ \frac{\partial u}{\partial t} &= \frac{\partial u}{\partial t_n}\frac{dt_n}{dt} = \frac{1}{\tau}\frac{\partial u}{\partial t_n}.\end{aligned}$$

Similarly, with the second and third derivatives,

$$\begin{aligned}\frac{\partial^2 u}{\partial t^2} &= \frac{\partial}{\partial t}\left(\frac{1}{\tau}\frac{\partial u}{\partial t_n}\right)\frac{dt_n}{dt} = \frac{1}{\tau^2}\frac{\partial^2 u}{\partial t_n^2}\\ \frac{\partial^3 u}{\partial t^3} &= \frac{1}{\tau^3}\frac{\partial^3 u}{\partial t_n^3}.\end{aligned}$$

Making these replacements, the Master Equation becomes:

$$\begin{aligned}\frac{\partial u}{z_3\partial z_n} + \frac{\sigma}{\tau}\frac{\partial u}{\partial t_n} &= \left\{(i\psi + g - l) + \left(\frac{g}{\Omega_g^2\tau^2} + \frac{1}{L_f\Omega_f^2\tau^2}\right)\frac{\partial^2}{\partial t_n^2}\right\}u\\ &+ \left\{\frac{\beta_3}{6\tau^3}\frac{\partial^3}{\partial t_n^3} + i\frac{\beta_4}{24\tau^4}\frac{\partial^4}{\partial t_n^4}\right\}u - i\frac{c_R\delta_3}{\tau}\frac{\partial|u|^2}{\partial t}u\\ &+ \left\{(\gamma_3 + i\delta_3)|u|^2 + (\gamma_5 + i\delta_5)|u|^4\right\}u.\end{aligned}$$

Next, we divide out $|\beta_3|/\tau^3$ so that the normalized third-order dispersion is $1/6$. This gives:

$$\begin{aligned}\frac{\tau^3}{|\beta_3|z_3}\frac{\partial u}{\partial z_n} + \frac{\sigma\tau^2}{|\beta_3|}\frac{\partial u}{\partial t_n} &= \left\{(i\psi + g - l)\frac{\tau^3}{|\beta_3|} + \left(\frac{g\tau}{\Omega_g^2|\beta_3|} + \frac{\tau}{L_f\Omega_f^2|\beta_3|}\right)\frac{\partial^2}{\partial t_n^2}\right\}u\\ &+ \left\{\frac{\beta_3}{6|\beta_3|}\frac{\partial^3}{\partial t_n^3} + i\frac{\beta_4}{24\tau|\beta_3|}\frac{\partial^4}{\partial t_n^4}\right\}u - i\frac{c_R\delta_3\tau^2}{|\beta_3|}\frac{\partial|u|^2}{\partial t}u\\ &+ \left\{(\gamma_3 + i\delta_3)\frac{\tau^3}{|\beta_3|}|u|^2 + (\gamma_5 + i\delta_5)\frac{\tau^3}{|\beta_3|}|u|^4\right\}u.\end{aligned}$$

Now, if we set the coefficient for $\partial u/\partial z_n$ to 1, we have that $z_3 = \tau^3/|\beta_3|$. We would also like to normalize the Kerr coefficient to unity, for which we choose $u = u_n/\sqrt{\delta_3 z_3}$. Finally, we get:

$$\begin{aligned}
\frac{\partial u_n}{\partial z_n} + \frac{\sigma\tau^2}{|\beta_3|}\frac{\partial u_n}{\partial t_n} &= \left\{(i\psi + g - l)\frac{\tau^3}{|\beta_3|} + \left(\frac{g\tau}{\Omega_g^2|\beta_3|} + \frac{\tau}{L_f\Omega_f^2|\beta_3|}\right)\frac{\partial^2}{\partial t_n^2}\right\}u_n \\
&+ \left\{\frac{\beta_3}{6|\beta_3|}\frac{\partial^3}{\partial t_n^3} + i\frac{\beta_4}{24\tau|\beta_3|}\frac{\partial^4}{\partial t_n^4}\right\}u_n - i\frac{c_R}{\tau}\frac{\partial|u_n|^2}{\partial t}u_n \\
&+ \left\{\left(\frac{\gamma_3}{\delta_3} + i\right)|u_n|^2 + (\gamma_5 + i\delta_5)\frac{|\beta_3|}{\delta_3^2\tau^3}|u_n|^4\right\}u_n
\end{aligned}$$

Thus, we can define normalized parameters, so that the normalized equation is of the same form as the unnormalized equation, Eq. (A.1). Thus,

$$\begin{aligned}
\sigma_n &= \frac{\sigma z_3}{\tau} \\
\psi_n &= \psi z_3 \\
g_n &= g z_3 \\
l_n &= l z_3 \\
L_{f,n} &= \frac{L_f}{z_3} \\
\Omega_{g,n} &= \Omega_g \tau \\
\Omega_{f,n} &= \Omega_f \tau \\
\beta_{2,n} &= 0 \\
\beta_{3,n} &= 1 \\
\beta_{4,n} &= \frac{\beta_4 z_3}{\tau^4} \\
c_{R,n} &= \frac{c_R}{\tau} \\
\gamma_{3,n} &= \frac{\gamma_3}{\delta_3} \\
\delta_{3,n} &= 1 \\
\gamma_{5,n} &= \frac{\gamma_5}{\delta_3^2 z_3} \\
\delta_{5,n} &= \frac{\delta_5}{\delta_3^2 z_3}
\end{aligned}$$

Bibliography

[1] B. J. Ainslie and C. R. Day, "A review of single-mode fibers with modified dispersion characteristics," *J. Lightwave Tech.*, vol. 4, no. 8, pp. 967–979, August 1986.

[2] D. Derickson, ed., *Fiber Optic Test and Measurement.* Upper Saddle River, New Jersey: Prentice Hall, 1998.

[3] J. C. Livas, "High sensitivity optically preamplified 10 Gb/s receivers," *Optical Fiber Communication*, vol. 5, pp. 343–345, 1996.

[4] J. Korn, "Propagation of a 10 Gbps RZ bit stream in a circulating loop using TrueWave and DCF with 100 km EDFA spacing," *LEOS'98 Conference Proceedings. 11th Annual Meeting IEEE Lasers and Electro-Optics Society*, vol. 1, pp. 14–15, 1998.

[5] I. Y. Khrushchev, I. H. White, and R. V. Penty, "High-quality laser diode pulse compression in dispersion-imbalanced loop mirror," *Electronics Letters*, vol. 34, no. 10, pp. 1009–1010, 1998.

[6] I. Y. Khrushchev, R. V. P. J. D. Bainbridge, and I. H. White, "Picosecond pulse source for OTDM/WDM applications based on arrayed waveguide grating," *Optical Fiber Communication Conference (February 25, 1999)*, pp. 296–298, 1999.

[7] K. R. Tamura and M. Nakazawa, "Spectral-smoothing and pedestal reduction of wavelength tunable quasi-adiabatically compressed femtosecond solitons using a

dispersion-flattened dispersion-imbalanced loop mirror," *IEEE Photonics Tech. Letters*, vol. 11, no. 2, pp. 230–232, 1999.

[8] M. Nakazawa, "Toward terabit/s single-channel transmission," *Optical Fiber Communciation Conference (February 26, 1999)*, pp. 132–133, 1999.

[9] W. S. Wong, S. Namiki, M. Margalit, E. P. Ippen, and H. A. Haus, "Optical pulse filtering with dispersion-imbalanced loop mirrors," in *Optical Fiber Communication*, vol. 6, (Washington, D.C.), pp. postdeadline paper PD–8, Optical Society of America, 1997.

[10] W. S. Wong, S. Namiki, M. Margalit, H. A. Haus, and E. P. Ippen, "Self-switching of optical pulses in dispersion-imbalanced nonlinear loop mirrors," *Optics Letters*, vol. 22, no. 15, pp. 1150–1152, 1997.

[11] H. A. Haus, *Waves and Fields in Optoelectronics.* Englewood Cliffs, N.J.: Prentice-Hall, 1984.

[12] V. E. Zakharov and A. B. Shabat, "Exact theory of two-dimensional self focusing and one-dimensional self modulation of waves in nonlinear media," *Sov. Phys. JETP*, vol. 34, pp. 62–69, January 1972.

[13] C. S. Gardner, J. M. Greene, M. D. Kruskal, and R. M. Miura, "Method for solving the Korteweg-de Vries equation," *Phys. Rev. Lett.*, vol. 19, pp. 1095–1097, 1967.

[14] E. Desurvire, "On the physical origin of the 3 dB noise figure limit in laser and parametric optical amplifiers," *Optical Fiber Technology*, vol. 5, no. 1, pp. 40–61, 1999.

[15] P. B. Hansen, A. J. Stentz, L. Eskilden, S. G. Grubb, T. A. Strasser, and J. R. Pedrazzani, "High sensitivity 1.3 μm optically preamplified receiver using Raman amplification," *Electronics Letters*, vol. 32, no. 23, pp. 2164–2165, 1996.

[16] S. D. Personick, "Receiver design for digital fiber optic communication systems, I," *The Bell System Technical Journal*, vol. 52, no. 6, pp. 842–886, 1973.

[17] S. D. Personick, "Receiver design for optical fiber systems," *Proc. IEEE*, vol. 65, no. 12, pp. 1670–1678, 1977.

[18] L. G. Kazovsky and O. K. Tonguz, "Sensitivity of direct-detection lightwave receivers using optical preamplifiers," *IEEE Photonics Tech. Letters*, vol. 3, no. 1, pp. 53–55, 1991.

[19] R. C. Steele, G. R. Walker, and N. G. Walker, "Sensitivity of optically preamplified receivers with optical filtering," *IEEE Photonics Tech. Letters*, vol. 3, no. 6, pp. 545–547, 1991.

[20] T. Li and M. C. Teich, "Bit-error rate for a lightwave communication system incorporating an erbium-doped fibre amplifier," *Electronics Letters*, vol. 27, no. 7, pp. 598–600, 1991.

[21] P. Diament and M. C. Teich, "Evolution of the statistical properties of photons passed through a traveling-wave laser amplifier," *IEEE J. Quantum Electronics*, vol. QE-28, no. 5, pp. 1325–1334, 1992.

[22] T. Li and M. C. Teich, "Photon point process for traveling-wave laser amplifiers," *IEEE J. Quantum Electronics*, vol. QE-29, no. 9, pp. 2568–2578, 1993.

[23] W. S. Wong, H. A. Haus, L. A. Jiang, P. B. Hansen, and M. Margalit, "Photon statistics of amplified spontaneous emission noise in a 10-Gbit/s optically preamplified direct-detection receiver," *Optics Letters*, vol. 23, no. 23, pp. 1832–1834, 1998.

[24] K. Shimoda, G. Takahashi, and C. H. Townes, "Fluctuations in amplification of quanta with application to maser amplifiers," *J. Phys. Soc. Jpn.*, vol. 12, no. 6, p. 686, 1957.

[25] L. Mandel *Proc. Phys. Soc.*, vol. 74, p. 233, 1959.

[26] J. B. Johnson and H. Nyquist, "Thermal agitation of electricity in conductors," *Phys. Rev.*, vol. 32, p. 110, 1928.

[27] K. Levenberg, "A method for the solution of certain non-linear problems in least squares," *Quart. Appl. Math.*, vol. 2, pp. 164–168, 1944.

[28] D. Marquardt, "An algorithm for least-squares estimation of nonlinear parameters," *SIAM J. Appl. Math.*, vol. 11, pp. 431–441, 1963.

[29] L. Boivin, M. C. Nuss, J. Shah, D. A. B. Miller, and H. A. Haus, "Receiver sensitivity improvement by impulsive coding," *IEEE Photonics Tech. Letters*, vol. 9, no. 5, pp. 684–686, 1997.

[30] N. J. Doran and D. Wood, "Nonlinear-optical loop mirror," *Optics Letters*, vol. 13, no. 1, pp. 56–58, 1988.

[31] M. E. Fermann, F. Haberl, M. Hofer, and H. Hochreiter, "Nonlinear amplifying loop mirror," *Optics Letters*, vol. 15, no. 13, pp. 752–754, July 1, 1990.

[32] D. J. Richardson, R. I. Laming, D. N. Payne, V. Matsas, and M. W. Phillips, "Selfstarting passively modelocked erbium fibre ring laser based on the amplifying Sagnac switch," *Electronics Letters*, vol. 27, no. 6, pp. 542–544, March 14, 1991.

[33] I. N. Duling, III, "Subpicosecond all-fibre erbium laser," *Electronics Letters*, vol. 27, no. 6, pp. 544–545, March 14, 1991.

[34] A. D. Ellis and D. A. Cleland, "Ultrafast all optical switching in two wavelength amplifying nonlinear optical loop mirror," *Electronics Letters*, vol. 28, no. 4, pp. 405–406, 13 Feb. 1992.

[35] M. Jinno and T. Matsumoto, "Ultrafast all-optical logic operations in a nonlinear Sagnac interferometer with two control beams," *Optics Letters*, vol. 16, no. 4, pp. 220–222, Feb. 15, 1991.

[36] D. Anderson, "Variational approach to nonlinear pulse propagation in optical fibers," *Phys. Rev. A*, vol. 27, pp. 3135–3145, 1983.

[37] D. Anderson, M. Lisak, and T. Reichel, "Asymptotic propagation properties of pulses in soliton-based optical-fiber communication systems," *J. Opt. Soc. Am.*, vol. B5, no. 2, pp. 207–210, 1988.

[38] D. Anderson and M. Lisak, "Bandwidth limits due to mutual pulse interaction in optical soliton communication systems," *Optics Letters*, vol. 11, no. 3, pp. 174–176, 1986.

[39] M. Karlsson and A. Höok, "Soliton-like pulses governed by fourth order dispersion in optical fibers," *Opt. Commun.*, vol. 104, pp. 303–307, 1994.

[40] D. Anderson, Y. S. Kivshar, and M. Lisak, "Polarization oscillations and soliton stability in birefringent optical fibres," *Physica Scripta*, vol. 43, pp. 273–280, 1991.

[41] M. Karlsson, D. Anderson, A. Höok, and M. Lisak, "A variational approach to optical soliton collisions," *Physica Scripta*, vol. 50, pp. 265–270, 1994.

[42] Y. S. Kivshar and W. Królikowski, "Lagrangian approach for dark solitons," *Opt. Commun.*, vol. 114, pp. 353–362, 1995.

[43] H. A. Haus, "Optical fiber solitons, their properties and uses," *Proc. IEEE*, vol. 81, no. 7, pp. 970–983, July 1993.

[44] J. D. Moores, "On the Ginzburg-Landau laser mode-locking model with fifth-order saturable absorber term," *Optics Communications*, vol. 96, no. 1,2,3, pp. 65–70, February 1, 1993.

[45] C. R. Doerr, H. A. Haus, E. P. Ippen, M. Shirasaki, and K. Tamura, "Additive pulse limiting," *Optics Letters*, vol. 19, no. 1, pp. 31–33, January 1, 1994.

[46] N. J. Doran and D. Wood, "Soliton processing element for all-optical switching and logic," *J. Opt. Soc. Am.*, vol. B4, no. 11, pp. 1843–1846, 1987.

[47] B. Olsson and P. A. Andrekson, "Noise filtering with the nonlinear optical loop mirror," *J. Lightwave Tech.*, vol. 13, no. 2, pp. 213–215, 1995.

[48] L. F. Mollenauer, M. J. Neubelt, S. G. Evangelides, J. P. Gordon, J. R. Simpson, and L. G. Cohen, "Experimental study of soliton transmission over more than 10,000 km in dispersion-shifted fiber," *Optics Letters*, vol. 15, no. 21, pp. 1203–1205, 1990.

[49] M. Nakazawa, E. Yamada, H. Kubota, and K. Suzuki, "10 Gbit/s soliton transmission over one million kilometres," *Electronics Letters*, vol. 27, no. 14, pp. 1270–1272, July 4, 1991.

[50] W. S. Wong, P. B. Hansen, T. N. Nielsen, M. Margalit, and S. Namiki, "In-band amplified spontaneous emission noise filtering with a dispersion-imbalanced nonlinear loop mirror," *J. Lightwave Tech.*, vol. 16, no. 10, pp. 1768–1772, 1998.

[51] H. Lefevre, *The Fiber-Optic Gyroscope*. Boston: Artech House, 1993.

[52] G. P. Agrawal, *Nonlinear Fiber Optics*. San Diego, CA: Academic Press, 1989.

[53] S. R. Chinn, "Error-rate performance of optical amplifiers with Fabry-Perot filters," *Electronics Letters*, vol. 31, no. 9, pp. 756–757, 1995.

[54] J. C. Cartledge and A. F. Elrefaie, "Effect of chirping-induced waveform distortion on the performance of direct detection receivers using traveling-wave semiconductor optical preamplifiers," *J. Lightwave Tech.*, vol. 9, no. 2, pp. 209–219, 1991.

[55] F. F. Rühl and R. W. Ayre, "Explicit expressions for the receiver sensitivity and system penalties of optically preamplified direct-detection systems," *IEEE Photonics Tech. Letters*, vol. 5, no. 3, pp. 358–361, 1993.

[56] L. F. B. Ribeiro, J. R. G. D. Rocha, and J. L. Pinto, "Performance evaluation of EDFA preamplified receivers taking into account intersymbol interference," *J. Lightwave Tech.*, vol. 13, no. 2, pp. 225–232, 1995.

[57] S. L. Danielsen, B. mikkelsen, T. Durhuus, C. Joergensen, and K. E. Stubkjaer, "Detailed noise statistics for an optically preamplified direct detection receiver," *J. Lightwave Tech.*, vol. 13, no. 5, pp. 977–981, 1995.

[58] C. Lawetz and J. C. Cartledge, "Performance of optically preamplified receivers with Fabry-Perot optical fibers," *J. Ligthwave Tech.*, vol. 14, no. 11, pp. 2467–2474, 1996.

[59] G. Jacobsen, "Multichannel system design using optical preamplifiers and accounting for the effects of phase noise, amplifier noise, and receiver noise," *J. Lightwave Tech.*, vol. 10, no. 3, pp. 367–377, 1992.

[60] J. N. Hollenhorst, "Fundamental limits on optical pulse detection and digital communication," *J. Lightwave Tech.*, vol. 13, no. 6, pp. 1135–1145, 1995.

[61] S. R. Chinn, D. M. Boroson, and J. C. Livas, "Sensitivity of optically preamplified DPSK receivers with Fabry-Perot filters," *J. Lightwave Tech.*, vol. 14, no. 3, pp. 370–376, 1996.

[62] I. T. Monroy and G. Einarsson, "Bit error evaluation of optically preamplified direct detection receivers with Fabry-Perot optical filters," *J. Lightwave Tech.*, vol. 15, no. 8, pp. 1546–1553, 1997.

[63] G. Einarsson and I. T. Monroy, "Error probability evaluation of optical systems disturbed by phase noise and additive noise," *Proceedings IEEE International Symposium on Information Theory (Cat. No.95CH35738)*, p. 482, 1995.

[64] F. I. Khatri, *Optical soliton propagation and control.* Ph.D. thesis MIT, 1996.